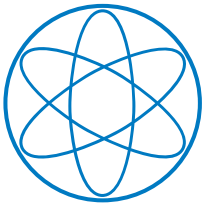

MASTER'S THESIS

Search for Recent ^{60}Fe Deposition in Antarctica with AMS

Suche nach aktueller ^{60}Fe Deposition in der Antarktis mit AMS

Dominik Koll
Matrikel Nr.: 03636179

May 1, 2018

GAMS-Group at Maier-Leibnitz-Laboratory

E15 Chair for Experimental Physics and Astroparticle Physics

Excellence Cluster "Origin and Structure of the Universe"

Physics-Department of Technical University of Munich

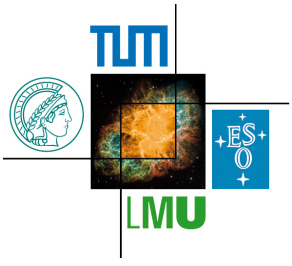

Abstract

The main aim of this thesis is the search for ^{60}Fe of different extraterrestrial origins in Antarctica. ^{60}Fe with a half-life of 2.6 Myr is mainly produced by stellar nucleosynthesis, explosive nucleosynthesis and by cosmic ray reactions on cosmogenic targets containing Ni. In contrast to these production paths, significant build-up of ^{60}Fe on Earth by cosmic rays is inhibited by the shielding of the atmosphere. Anthropogenic production by accelerators, nuclear reactors and nuclear weapon tests is also insignificant because of either high dilution by stable Fe or regionality of these hot-spots. Hence, any detection of ^{60}Fe in the environment on Earth is directly related to the input of extraterrestrial material.

For this project, 500 kg of pure Antarctic surface snow from the Kohnen Station in Dronning Maud Land, Antarctica, were shipped frozen to Munich. By filtering the molten snow and separating Fe from other elements in the filters and the water, two samples for an ultra-sensitive Accelerator Mass Spectrometry (AMS) measurement were produced. The filters were chemically treated by collaborators at the Helmholtz-Zentrum Dresden-Rossendorf (HZDR) and the water was treated by collaborators at the Atominstitut of TU Vienna. In the scope of this work, the already established chemistry to separate Fe from Ni, applied by HZDR, was improved for the water sample to obtain higher purity for smallest sample masses. The improved chemistry, with significantly less utilization of chemicals like concentrated acids, is able to suppress the amount of Ni in the AMS sample just as well as the established chemistry, and reduces some interfering isotopes, e.g. ^{59}Co, further. The total amount of initially present Fe in the filters is 4.2 mg, whereas the amount of Fe in the water is only 0.7 mg. Furthermore, larger particles from the filters were hand-picked and stored for further analysis.

^{60}Fe measurements were performed at the Maier-Leibnitz-Laboratory in Garching, Germany, using AMS. This facility features a 14 MV tandem accelerator and a dedicated AMS setup for isobaric suppression (GAMS). The lowest detection limit obtained for the AMS measurements is $^{60}\mathrm{Fe/Fe} = 2.5 \cdot 10^{-16}$ with full background suppression. The AMS measurements of the filter and the water samples yielded concentrations of ^{60}Fe/Fe significantly above background level. The filters show an ^{60}Fe concentration of $^{60}\mathrm{Fe/Fe} = 1.1 \cdot 10^{-15}$, whereas the water shows $^{60}\mathrm{Fe/Fe} = 3.5 \cdot 10^{-15}$, with high uncertainties of almost a factor of 2 because of low counting statistics. These concentrations could be converted to the number of ^{60}Fe atoms in the samples that is $4.9 \cdot 10^4$ atoms and $2.3 \cdot 10^4$ atoms for the filter and the water samples, respectively.

By this measurement, the accretion rate of extraterrestrial Ni in Antarctica is calculated to be 10^{-9} g/cm^2/yr, assuming chondritic composition of the extraterrestrial material, a production rate of 0.51 dpm/kg for a pure Ni target of micrometeoritic size, and the measured concentrations to be purely cosmogenically produced. Any interstellar contribution is currently not identifiable by this search, but also not excluded. Further measurements of isotopes of purely cosmogenic origin will constrain the source of the detected ^{60}Fe nuclei further.

Summarizing, this is the first-ever detection of extraterrestial ^{60}Fe in Antarctica with the use of AMS.

Kurzdarstellung

Das Ziel dieser Arbeit ist die Suche nach extraterrestischem ^{60}Fe unterschiedlicher Herkunft in der Antarktis. ^{60}Fe mit einer Halbwertszeit von 2.6 Myr wird hauptsächlich durch stellare Nukleosynthese, explosive Nukleosynthese und durch Reaktionen kosmischer Strahlung mit Ni Targets gebildet. Im Gegensatz dazu ist die ^{60}Fe Produktion auf der Erde durch kosmische Strahlung nicht signifikant, da die Atmosphäre diese abschirmt. Anthropogene Produktion durch Beschleunigeranlagen, Kernreaktoren oder Kernwaffentests ist ebenfalls nicht signifikant, da die ^{60}Fe Konzentrationen entweder durch stabiles Fe zu sehr verdünnt sind oder nur sehr lokalisiert auftreten. Deswegen ist eine Detektion von ^{60}Fe auf der Erde ein direkter Hinweis auf den Eintrag extraterrestrischer Materie.
Im Zuge dieses Projekts wurden 500 kg reinster antarktischer Schnee von der Kohnen Station in Dronning Maud Land, Antarctica, in gefrorenem Zustand nach München transportiert. Durch Filtration und chemischer Abtrennung von Fe wurden zwei Proben für eine ultra-sensitive Beschleunigermassenspektrometrie-Messung (AMS) gewonnen. Die Filter wurden durch Kollegen am Helmholtz-Zentrum Dresden-Rossendorf (HZDR) chemisch behandelt, wohingegen das Wasser von Kollegen am Atominstitut der TU Wien weiterverarbeitet wurde. Die etablierte Probenchemie, welche durch das HZDR zur Trennung von Fe und Ni angewendet wird, wurde weiterentwickelt, um höhere Reinheit in der AMS Messung zu erreichen und die chemische Trennung für kleinste Probenmengen zu optimieren. Vergleichbare Trennung von Fe und Ni wurde bei geringerer Menge an konzentrierten Säuren und weiterer Reduktion störender Spezies, wie zum Beispiel ^{59}Co, erreicht. In den Filtern befinden sich 4.2 mg Fe, wobei im Wasser mit nur 0.7 mg Fe deutlich weniger Fe vorhanden ist. Größere Staubkörner, welche herausgefiltert worden sind, wurden für weitere Untersuchungen beiseite gelegt.
Die ^{60}Fe Messungen wurden am Maier-Leibnitz-Laboratorium (MLL) in Garching, Deutschland durchgeführt, wobei ein 14 MV Tandem Beschleuniger, sowie ein dediziertes AMS Messsystem für isobarische Unterdrückung (GAMS), zur Verfügung stehen. In den Messungen wurde eine Sensitivität von $^{60}\mathrm{Fe/Fe} = 2.5 \cdot 10^{-16}$ erreicht, wobei diese Messungen untergrundfrei sind. Desweiteren wurden ^{60}Fe/Fe Konzentrationen signifikant oberhalb des erwarteten Untergrundlevels gefunden, für die Filter $^{60}\mathrm{Fe/Fe} = 1.1 \cdot 10^{-15}$ und für das Wasser $^{60}\mathrm{Fe/Fe} = 3.5 \cdot 10^{-15}$, mit großen Fehlerbereichen bis zu einem Faktor 2 wegen kleiner Zählstatistik. Diese Konzentrationen entsprechen $4.9 \cdot 10^4$ ^{60}Fe Atome für die Filter, beziehungsweise $2.3 \cdot 10^4$ ^{60}Fe Atome für das Wasser.
Durch diese Messungen kann mit Hilfe der Produktionsrate von 0.51 dpm/kg für mikrometeoritische Ni Targets, welche eine rein chondritische Zusammensetzung haben, eine Akkretionsrate von extraterrestrischem Ni in der Antarktis von 10^{-9} g/cm^2/yr errechnet werden. Ein interstellarer Anteil kann durch diese Messung noch nicht identifiziert, jedoch auch nicht ausgeschlossen werden. Weitere Messungen rein kosmogen erzeugter Nuklide werden den Ursprung der gemessenen ^{60}Fe Konzentrationen weiter einschränken.
Zusammenfassend wurde im Zuge dieses Projekts erstmalig extraterrestrisches ^{60}Fe in der Antarktis durch AMS Messungen detektiert.

Contents

1 Introduction

For centuries, scientists on Earth have tried to explain the origin of life. This is a fundamental open question of mankind. Directly related to that question is the origin of heavy elements and the influence of extraterrestrial processes on planet formation and evolution of life. All these questions depend strongly on the physics of stars and cosmic rays. By observation and theoretical models of stars and stellar explosions like Supernovae (SNe), these questions can be tackled.

One way to encounter these problems is to analyze tracers which are directly produced in these objects, with lifetimes long enough to detect them on or near Earth, and which are unique in their signal. Ejection and transport processes must be efficient enough to inject measurable quantities into our solar system. One distinct candidate is the long-lived radioisotope ^{60}Fe.
^{60}Fe with a half-life of (2.62±0.04) Myr [96] is produced in late stellar burning phases and core-collapse supernovae [69]. Another production process is spallation of Ni by cosmic rays [60]. Significant production on Earth by cosmic rays is prohibited by the atmosphere, the entry of the radioisotope from outer space is small compared to the total abundance of stable Fe and there is no major anthropogenic production site. Nuclear weapon tests lead to a slight enrichment of ^{60}Fe in the environment, but these hot-spots are restricted to certain areas. Globally, this contribution could be neglected. Consequently, the natural level of ^{60}Fe relative to stable Fe on Earth is $^{60}\mathrm{Fe/Fe} < 10^{-17}$, too small to be detectable by any measurement technique available at this time. In special cases, where dilution by stable Fe is minimized, the accumulation of ^{60}Fe is favored or an ^{60}Fe injecting event occurs, measurements are possible.
In the past, different approaches to detect extraterrestrial ^{60}Fe were adopted. The most prominent approaches are Accelerator Mass Spectrometry (AMS) and cosmic ray detection. Typical radioisotope detection by decay counting is not applicable here because of the long half-life and the minute concentrations.
The first AMS detection of stellar ^{60}Fe was reported by the AMS group in Munich in 1999 [61]. A ferromanganese crust from the pacific ocean was analyzed and ^{60}Fe was found significantly above background in a time window which could be related to stellar explosions. Further studies confirmed this result in a time range roughly 1.5 Myr to 3 Myr ago [59, 36]. Additionally to crust material, marine sediment is also a possible reservoir for extraterrestrial Fe. First investigations in Pacific sediments were inconclusive [36]. More recent projects confirmed the long ranging ^{60}Fe deposition in the ferromanganese crust also in marine sediments [71] and on a global scale [112]. Ejecta from SNe containing ^{60}Fe passed our solar system, hence ^{60}Fe should also have been deposited on other objects. Studies of samples from the lunar surface by the Munich group [34] revealed ^{60}Fe above cosmogenically produced background on the Moon.
Since these results show nucleosynthesis by stars millions of years ago, currently ongoing nucleosynthesis should also be detectable. Findings of ^{60}Fe in cosmic rays [14] and γ-rays from the decay $^{60}\mathrm{Fe} \xrightarrow{\beta} {}^{60}\mathrm{Co} \xrightarrow{\beta} {}^{60}\mathrm{Ni}$ [115] provide evidence about currently ongoing nucleosynthesis. In this case, γ-counting is possible because of the high source ratio of $^{60}\mathrm{Fe/Fe} \approx 7 \cdot 10^{-5}$ [14] and the measurable line flux of $\mathrm{F}_\gamma \approx 4 \cdot 10^{-5}\,\mathrm{cm}^{-2}\,\mathrm{s}^{-1}\,\mathrm{rad}^{-1}$ for the inner galaxy [115]. Furthermore,

^{60}Fe as part of a greater collection of radioisotopes was already present at the formation of the solar system [47]. Radioisotopes, produced and ejected by supernovae and present already at the early stages of the solar system, are clear hints for dust decoupling and injection into dense clouds [46]. Dust is a viable candidate to transport synthesized material to Earth and to be incorporated into geological reservoirs.

In this project, a new possible geological reservoir for ^{60}Fe is introduced: Antarctic snow. A suitable geological reservoir is characterized by a low anthropogenic input and an intrinsic pureness of the reservoir itself. Antarctica is mostly uninhabited which reduces anthropogenic contributions to a minimum. Known precipitation rates [86, 15], measured infall of extraterrestrial matter [44, 28] and ice/snow as pure material could be used to infer accumulation of extraterrestrial matter which is mainly deposited in the form of micrometeorites (MM's) and Interplanetary Dust Particles (IDP's). The largest contribution to the annual infall of extraterrestrial matter (220 t/yr - 78,000 t/yr) comes from cosmic dust [21, 16, 41].
Cosmic rays, and in this case especially solar cosmic rays, produce ^{60}Fe by nuclear reactions on stable Ni nuclei. To identify the origin of ^{60}Fe in the sample material (stellar or cosmogenic), known production rates [108] by cosmic rays as well as the flux of ^{60}Fe near Earth, induced by Interstellar Dust (ISD) [61, 34] are used.

Within the scope of the Antarctica project of the AMS group in Munich, 500 kg of surface snow from the Kohnen Station in Dronning Maud Land, Antarctica, were shipped frozen to Munich, molten and filtered and subsequently chemically treated by collaborators at Helmholtz-Zentrum Dresden-Rossendorf (HZDR) in Dresden, Germany and at Atominstitut in Vienna, Austria. The sample set is divided by filtering in two fractions with larger and smaller particles ($< 2\,\mu$m $<$). In general, the amount of material in the water, as well as in the filters, (without considering previously collected and stored MM's) is in the order of 100 μg - 10 mg. AMS measurements of ^{60}Fe were carried out in Munich at the Maier-Leibnitz-Laboratory in Garching to determine the ^{60}Fe concentrations in the filters and in the water. Later measurements of ^{41}Ca and ^{53}Mn will complete the Antarctica project. It has to be mentioned that this material is recent material from the surface of Antarctica. This is in contrast to most other measurements, where old material was used which needed to be dated.

In addition to these points, it is the first time to analyze such a high amount of Antarctic snow for its ^{60}Fe content with ultra-sensitive AMS. Therefore, this project plays a pioneering role in this field of research and could improve the knowledge about extraterrestrial influx and injection mechanisms of dust into the solar system and onto Earth.

In the following chapters, ^{60}Fe is characterized as a suitable tracer for astrophysical processes. Its production in stars and its route to Earth is displayed. Further on, a description of the sample material as well as chemical isolation and purification techniques are given. Afterwards, AMS is introduced as an ultra-sensitive detection technique for smallest concentrations with focus on the setup available in Munich. Finally, experimental procedures are explained and results are discussed.

2 ^{60}Fe: From Production to Deposition on Earth

In this chapter, ^{60}Fe as a tracer for different extraterrestrial processes, including stellar nucleosynthesis, explosive nucleosynthesis and cosmic ray production, is introduced. Characterization and production is followed by incorporation in dust and deposition on Earth.

2.1 ^{60}Fe Characteristics

Fe is one of the most abundant elements on Earth and in the solar system. The high abundance results from the high binding energy per nucleon of 8.8 MeV, which is in the peak of all binding energies per nucleon. Therefore, stable Fe nuclei are in an energetically favorable configuration of nucleons. Higher mass elements can energetically undergo fission and lower mass elements can undergo fusion towards the Fe-peak of binding energy. Fe is mainly produced in stars by stellar nucleosynthesis, as it will be displayed in the following.

Fe has four stable isotopes, namely ^{54}Fe, ^{56}Fe, ^{57}Fe and ^{58}Fe with natural isotopic abundances of 5.8%, 91.8%, 2.1% and 0.3%, respectively. In addition to the four naturally occurring stable isotopes, Fe has more than twenty unstable isotopes, predominantly with half-lives in the microsecond range. The only long-lived radioisotope of Fe is ^{60}Fe, with a newly determined half-life of $T_{1/2} = (2.62 \pm 0.04)$ Myr [96].

The first determination of the half-life of ^{60}Fe was performed in 1957 [95]. The concentration of ^{60}Fe was herby not determined directly but only estimated from the produced activity in an irradiated copper target from proton irradiation. The very uncertain value of $3 \cdot 10^5$ yr was improved by measurements in 1984 [66] which showed that ^{60}Fe has a half-life in the Myr range, (1.49±0.27) Myr. This was the first time that AMS was used in combination with decay counting of the ingrowth of radioactive ^{60}Co for the determination of the ^{60}Fe half-life via equation 2.1. In 2009, the half-life of ^{60}Fe was determined a third time, now by the AMS group in Munich [96]. Indeed, enough material was available to measure the amount of ^{60}Fe by multicollector inductively coupled plasma mass spectrometry without the need for an AMS measurement. The significantly higher value of (2.62±0.04) Myr was established and recently confirmed [113], [87]. One has to mention that the ingrowth of the isomeric state of ^{60}Co could also be used for activity determination, because this measurement is particularly free from possible background coming from already abundant ^{60}Co in the sample.

$$A = -\frac{dN}{dt} = \lambda N \tag{2.1}$$

^{60}Fe is β^- unstable and decays via ^{60}Co ($T_{1/2} = 5.3\,\mathrm{yr}$) to stable ^{60}Ni. Two γ-rays with energies of $E_1 = 1173\,\mathrm{keV}$ and $E_2 = 1333\,\mathrm{keV}$ are emitted which are important γ-lines for astronomy [115]. The detection of both γ-rays from several of these decays is a clear indication for ^{60}Fe in the Interstellar Medium (ISM). For a decay scheme, see Figure 2.1. ^{60}Fe is separated by two masses from its next stable isotope ^{58}Fe and is also separated by two nuclear charges from its only stable isobar ^{60}Ni. This is convenient for the detection of ^{60}Fe by AMS, as illustrated in the following chapters. ^{60}Ni is the second most abundant isotope of Ni, with isotopic abundance of 26.3% after ^{58}Ni with 68.1%. Ni, just like Fe, is one of the most abundant elements on Earth, which is problematic for AMS measurements, as natural samples are heavily contaminated with Ni. For an excerpt of the chart of the nuclides around Fe, see Figure 2.2.

^{60}Fe features some properties that makes it a suitable tracer for astrophysical processes. It is not produced in significant amounts by anthropogenic processes in the environment on Earth. Only dedicated facilities, e.g. accelerators with energies above 1 GeV and experimental reactors with neutron sources, are able to produce ^{60}Fe on Earth in considerable quantities, besides the already discussed nuclear weapon tests. The production of these spikes has no influence on the global ^{60}Fe budget because of the dilution by stable Fe. ^{60}Fe is also not produced significantly by cosmic rays on Earth because of the shielding of Earth's atmosphere. Furthermore, no primordial ^{60}Fe is left on Earth due to its short half-life compared to the age of the Earth.
Any ^{60}Fe detected on Earth must originate from outer space, if entry from the discussed sources could be excluded. Astrophysical production sites for ^{60}Fe are cosmic ray production in interplanetary bodies and nucleosynthesis in stars. Thus, ^{60}Fe could be deposited on Earth by meteorites or dust grains which emanate from stars by winds or explosions, or by ejection from their cosmogenic parent body after collisions.

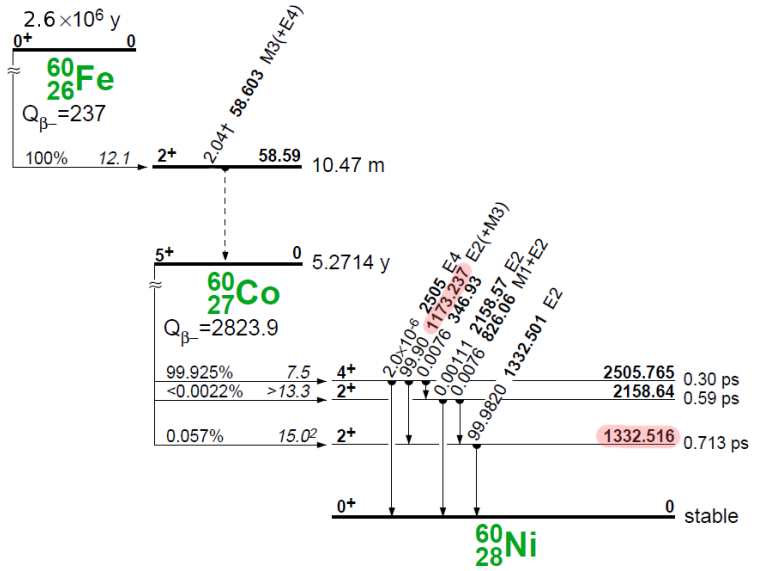

Figure 2.1: Decay scheme of ^{60}Fe with its daughter nuclides ^{60}Co and ^{60}Ni. Important γ-rays for astrophysics are indicated. Figure taken from [70].

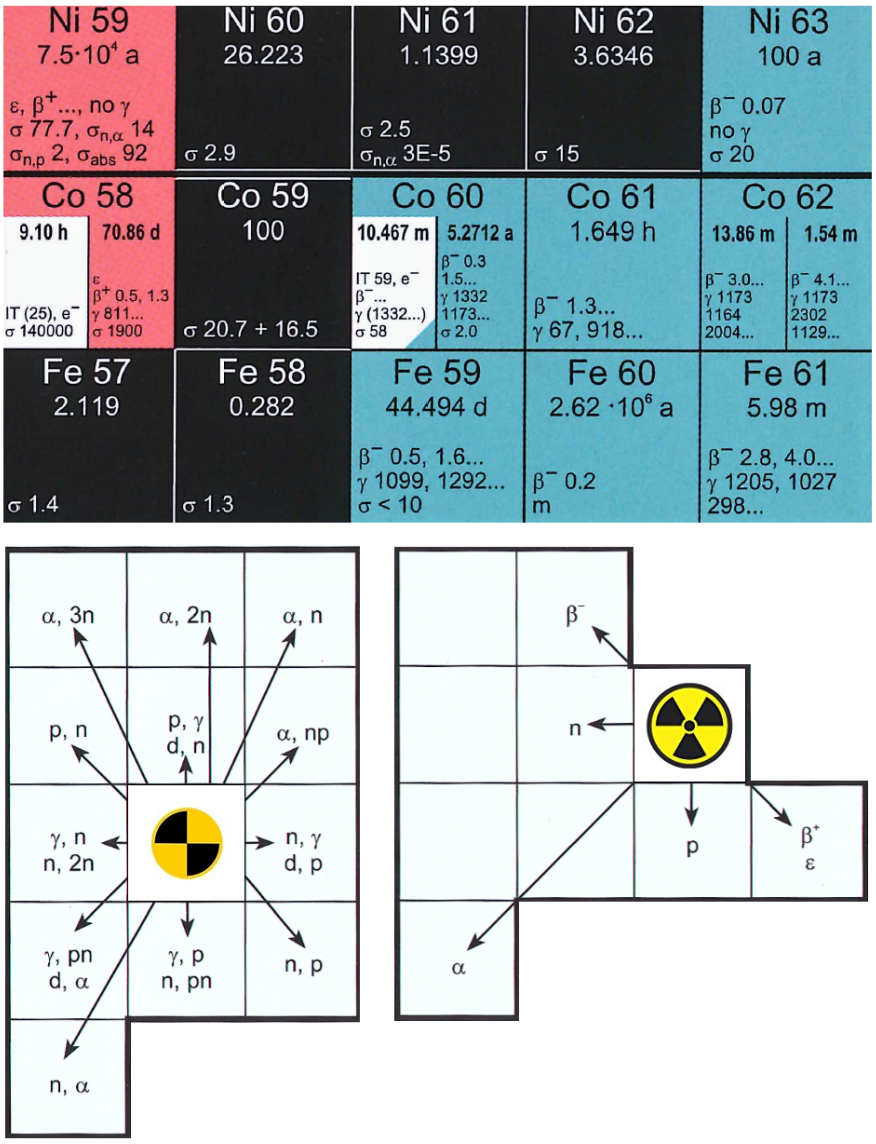

Figure 2.2: Chart of the nuclides for isotopes near ^{60}Fe. The single stable isobar ^{60}Ni and the next stable isotope ^{58}Fe are two nuclear charges and two masses apart from ^{60}Fe, respectively. Nuclear reactions, as well as radioactive decay path ways, are shown below. Figure modified from the Chart of the Nuclides (2015) [75].

2.2 Stellar Origin of ^{60}Fe

At first, the production of ^{60}Fe in stellar environments will be discussed, which includes stellar nucleosynthesis and explosive scenarios. In this case, dust will be the main carrier of any ^{60}Fe atoms, as it will be shown in the following chapters. Different stellar production mechanisms and sources for a detectable ^{60}Fe signal on Earth are considered. Here, stellar nucleosynthesis and nuclear astrophysics are based on [23, 10, 52].

2.2.1 Stellar Evolution and Nucleosynthesis

Almost all elements of the periodic table are produced in stellar environments. Only the lightest elements, i.e. H, He and a tiny fraction of Li, were already present after the big bang and before the first generation of stars started their nucleosynthesis. This very first production of elements is called big bang nucleosynthesis. The next step of nucleosynthesis is stellar nucleosynthesis by nuclear fusion in stars.

The birth of a star starts with the gravitational contraction of a gas cloud. The contraction releases, according to the Virial theorem (equation 2.2), energy in the form of heat.

$$E_{grav.} + 2E_{therm.} = 0 \tag{2.2}$$

During contraction, a stabilizing equilibrium between the gravitational force and the gas pressure is established, which is called hydrostatic equilibrium. The start of nuclear burning is highly dependent on temperature that itself is dependent on the heat release by contraction. If the initial mass of the contracting cloud is $M_{cloud} > 0.08\,M_\odot$, the proto-star will start with its first nuclear burning step, H-burning. Any proto-star with less mass is called brown dwarf and will never reach nuclear burning. The parameters determining the evolution of a star are its mass, metallicity, angular momentum and possible companion stars. In the following, evolution due to different initial mass is considered.

Stars with $0.08\,M_\odot < M < 0.4\,M_\odot$ are so-called red dwarfs. These stars fuse H to He in their cores. Because of their low mass, the consumption of H takes longer than the age of the universe. In the end, they will consist only of He and no further nuclear reactions could be triggered. They will cool down as He white dwarfs. Termination of cooling could lead to hypothetical black dwarfs without emission of light.
White dwarfs (WD's) are remnants of stellar evolution without explosive scenario. These remnants are stabilized by electron degeneracy pressure against gravitational collapse. No nuclear reactions occur and hot WD's cool down by photon emission. In binary systems, a WD could accrete matter by gravity from a companion which leads to a revival of nuclear burning.

For stars with $0.4\,M_\odot < M < 8\,M_\odot$, H-burning could proceed via the so-called pp-chain or the CNO-cycle, depending on the mass of the star. For stars below $1.5\,M_\odot$, four protons fuse to ^{4}He, including a weak interaction step to form deuterium, whereas for stars above $1.5\,M_\odot$, four protons fuse to ^{4}He with C, N and O as catalysts (see equation 2.3 and equation 2.4).

$$4p \xrightarrow[d(p,\gamma)^3He]{p(p,e^+\nu)d} {}^4He + 2e^- + 2\bar{\nu_e} + Q_{pp} \tag{2.3}$$

$$4p \xrightarrow[(p,\gamma),(p,\alpha),\beta]{C,N,O\ catalysts} {}^4He + 2e^- + 2\bar{\nu_e} + Q_{CNO} \tag{2.4}$$

Q-values for the reactions are $Q_{pp} = Q_{CNO} = 26.73\,\mathrm{MeV}$, and different reactions occurring throughout the process are indicated by the reactions above and below the arrows. Effective Q-values are slightly lower because of neutrino cooling. The pp-chain, as well as the CNO-cycle, appear in all stars, but depending on their mass and therefore their core temperature, the contribution to the total energy production is different. Heavier stars obtain most of their energy from the CNO-cycle, whereas stars as the Sun proceed mainly via the pp-chain.

These light stars have enough mass to ignite He-burning after H is consumed. He-burning happens through the resonant triple-α process, where two He nuclei fuse to unstable ^{8}Be, which either disintegrates back to He or fuses with another He nucleus to C via ^{4}He(^{4}He,γ)^{8}Be(^{4}He,γ)^{12}C. Subsequent captures of He on C nuclei lead to the build-up of O. As a consequence of this process, elements between He and C (Li, Be, B) are not synthesized in stars. These elements are either slightly produced in the big bang or by cosmic-ray spallation of heavier elements.
These stars have inert He shells around an inert C and O core and H-burning shells above. H-burning adds He to the inert He shell until He-burning starts violently by a so-called He shell flash. The star expands and the H-burning shell cools until nuclear burning stops. Subsequent contraction and revived H-burning leads to He shell flashes after 10,000 years - 100,000 years. This phase is called Asymptotic Giant Branch phase (AGB-phase) and is important for nucleosynthesis of heavier elements. After He is exhausted, these light stars cannot ignite further burning steps and end as C/O WD's.

Stars with $8\,\mathrm{M}_\odot < \mathrm{M} < 10\,\mathrm{M}_\odot$ can ignite C-burning in the core which leads to production of O and Ne. In the end, an O/Ne WD is the remainder of C-burning. Another possibility is that these stars release their synthesized material in an Electron Capture Supernova (ECSN) [55].

If the initial mass of the star is beyond $\mathrm{M} = 10\,\mathrm{M}_\odot$, further burning stages are ignited, namely Ne-burning, O-burning and Si-burning. Ne-burning and Si-burning happen by photodisintegration of seed nuclei by the intense photon bath at temperatures in the GK range. O-burning is the last fusion step before the formed elements in the star are processed in a photodisintegration rearrangement. In the end, Nuclear Statistical Equilibrium (NSE) is reached in the star, where all electromagnetic and strong interactions are in equilibrium and nuclei are rearranged up to the peak of binding energy per nucleon. The maximum of binding energy is around Fe which stops the energy production of the star after an Fe core is established. Subsequently, the star cannot sustain the pressure against gravitational collapse, which ends in a Core Collapse Supernova (CCSN).

A CCSN starts by the collapse of the star under its own gravity, after nuclear reactions cannot generate energy and therefore pressure any further. Photodisintegration becomes dominant and consumes energy by the endothermic splitting of the previously produced nuclides. Free

electrons are subsequently captured by nuclides, which leads to a neutronization of the core. Furthermore, energy is also carried away by neutrinos, which in total leads to the collapse of the star [51, 118]. After the inner core reaches nuclear densities, the residual, still in-falling core is reflected and creates a shock wave within the outer in-falling layers. This shock wave is already stopped in the interior of the dying star and establishes a high density outer layer of the core. These high densities reduce the mean free path of neutrinos, escaping from the core, in such a way, that the energy transfer by neutrinos could trigger another shock wave which in the end leads to a CCSN [54]. High densities, energy transfer and shock waves generate an environment for explosive nucleosynthesis [50, 68]. The remnant of a CCSN is either a Neutron Star (NS) or a Black Hole (BH), depending on the mass of the remnant and the progenitor.
Nucleosynthesis in heavy stars only leads to elements lighter than Fe, because the Coulomb-barrier for charged particle fusion is too high for further fusion steps at stellar temperatures. Therefore, neutral particles could be used to produce heavier nuclides by fusion. Free neutrons are not initially abundant in stars because of the short free neutron half-life. Neutron producing reactions occur in advanced stellar nucleosynthesis as well as in explosive environments with high neutron densities. There are two different neutron capture processes, distinguishable by the intensity of the flux of free neutrons.

The slow neutron capture process (s-process) takes place during stellar nucleosynthesis, mainly in AGB stars [56]. Neutron liberating reactions occur during He and C shell- or core-burning (see equation 2.5).

$$^{22}Ne(\alpha,n)^{25}Mg \qquad ^{13}C(\alpha,n)^{16}O \tag{2.5}$$

For the s-process, a low neutron flux ($10^7\,\mathrm{cm^{-2}\,s^{-1}} < \mathrm{n} < 10^{11}\,\mathrm{cm^{-2}\,s^{-1}}$) over medium timescales (thousands of years) are available. Neutron capture is much slower than the β-decay of neutron-rich nuclides. Therefore, new elements are generated along the valley of stability. The s-process terminates at ^{209}Bi, which is unstable, but with a half-life longer than the age of the universe, it is the last non-decaying element [76].
The rapid neutron capture process (r-process) requires a much higher neutron flux (up to $\mathrm{n} = 10^{27}\,\mathrm{cm^{-2}\,s^{-1}}$). By this high neutron flux, neutron capture is more likely than β-decay which leads to neutron-rich isotopes far off the valley of stability and close to the neutron drip line. After termination of the neutron flux (seconds), the highly unstable nuclides decay towards the valley of stability, which leads to the build-up of elements up to the actinides. The origin of r-process elements is subject of current research, where CCSNe and neutron star mergers (NS-NS merger) are considered as possible candidates due to the extreme environment. Recently, by the first time ever simultaneous observation of gravitational waves and photons from NS-NS merger [1, 91] and by AMS measurements on actinides [111], the favored explanation for r-process nucleosynthesis tends to NS-NS merger. See Figure 2.3 for an abundance pattern of elements in the galactic environment and their respective production mechanism.
Proton-rich nuclides are also produced in stars, whereas the exact production mechanism is unclear. Possible reactions are rapid proton capture (rp), photodisintegration (γn) or neutrino-induced reactions (νp). Waiting-point nuclei, which slow down the reaction by their long half-life and low cross sections, could be overcome by additional neutron captures. These reactions are often summarized as the p-process, following the nomenclature of the s/r-process.

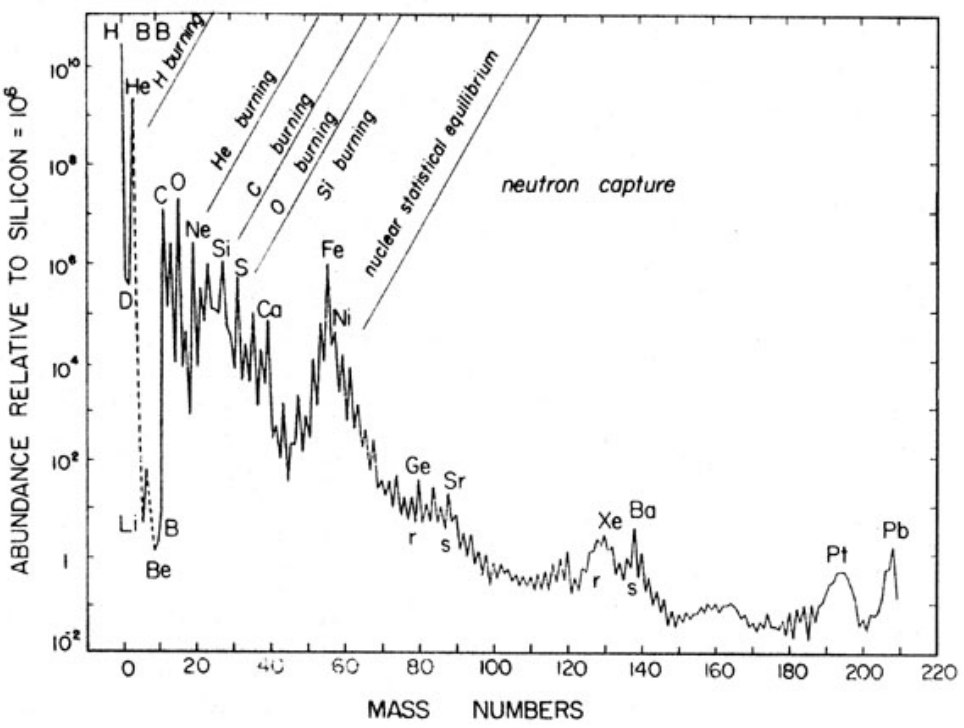

Figure 2.3: Local galactic abundance distribution for elements in all mass ranges normalized to 10^6 ^{28}Si atoms. Displayed data consists of solar system abundances as well as of data from nearby stars and nebula. Note the labels for the production mechanism of the elements and the peak pattern which represents nuclear features like binding energies and closed nucleon shells. Figure taken from [89].

Thermonuclear Supernovae (TNSN) are another form of stellar explosions. In contrast to a CCSN, where a remnant depending on the progenitor mass remains after the explosion, a TNSN leads to a full disruption of the star. The progenitors are WD and companions as binary systems. The WD accretes matter from the companion which leads to runaway fusion reactions in the WD. The WD is not able to expand and cool because of degenerate conditions and therefore, the energy increases until degeneracy is lifted and the WD explodes with full disruption. TNSN, also known as SNIa, are used as cosmic standard candles for distance measurements because of their unique and constant light curves and their brightness which can outshine their host galaxy with all other stars.

SNe are potentially dangerous for life on Earth. Enhanced cosmic radiation might deteriorate the ozone layer which has biological effects on living beings [6]. An approximated kill-radius is around 10 pc which is fortunately too close for possible SN candidates known at this time to harm us [43], especially since the supernova rate in our galaxy is at most three per century [3]. This does not exclude the possibility that mass-extinction events in the past could be related to SNe in the near vicinity of Earth [63]. Detection of SN produced material on Earth could therefore be used to improve our understanding of the evolution of life in the past and also set benchmarks for evolutionary phases.

An elegant way to summarize different stages of stellar evolution and to cluster stars by their spectral properties, is the Hertzsprung-Russell diagram (HRD). Stars are clustered in a 2-D representation by their luminosity and their effective surface temperature. Other possible sorting criteria are stellar magnitude or the spectral class of the star. Prominent features of the HRD are the Main Sequence which is related to H-burning stars, the Giant and Supergiant branch of evolved stars and WD's. In addition to the already mentioned groups, evolutionary lines like the Hayashi track could be obtained. See Figure 2.4 for a schematic HRD.

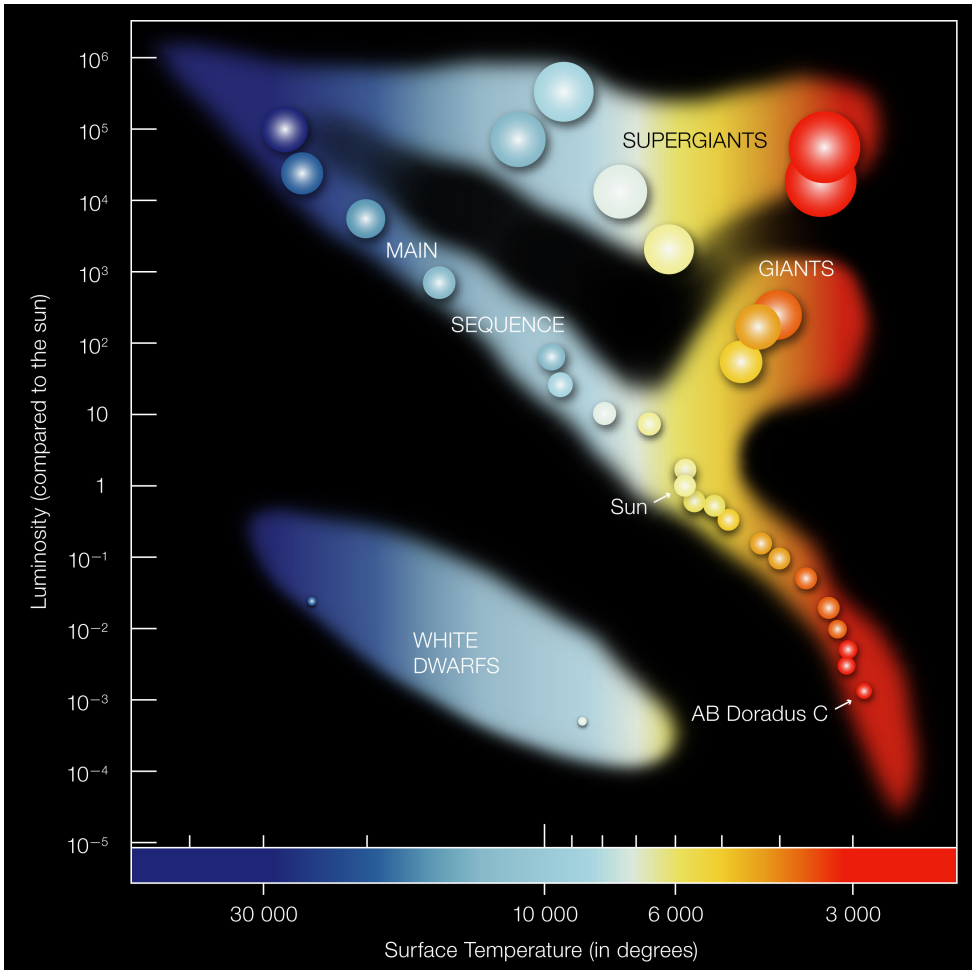

Figure 2.4: Schematic Hertzsprung-Russell-Diagram for different groups of stars. Most of the stars are accomodated in the Main Sequence, whereas evolved stars are right to the Main Sequence and WD's are left to the Main Sequence. Most of the stars are in the Main Sequence, because H-burning lasts much longer than all subsequent burning phases. Picture taken from [105].

2.2.2 ^{60}Fe Dust from AGB-Stars and Supernovae

^{60}Fe is produced in stellar vicinities. The main production mechanism is neutron capture on stable Fe during the s-process in stellar or explosive nucleosynthesis. In the following, production of dust at different astrophysical sites and stardust as source for ^{60}Fe on Earth is established.

At first, dust production in CCSN is evaluated and the evolution after the explosion is described. Triggered by the explosion of the star, synthesized material is ejected into the ISM within a shock wave. The Supernova Remnant (SNR) starts in the Ejecta Dominated (ED) phase, where the shock wave is barely influenced by the sweep-up of material from the ISM. A contact discontinuity between the shocked ISM and the ejected stellar material is formed which in the end leads to a reverse shock, when the mass of the shocked ISM material equals the mass of the ejected material [67]. After the reverse shock has heated the interior of the SNR by kinetic energy transfer, the SNR is in the Sedov-Taylor (ST) phase of adiabatic, pressure-driven expansion. Here, radiative losses are subordinate because of high temperatures and fully-ionized conditions. The first phases of SNR evolution could be solved by a self-similar solution with highest accuracy [109]. The last phase of the SNR evolution is the "Snow-Plough" (SP) phase. More and more material from the ISM is accumulated in front of the decelerating shock front, where energy is dissipated by radiation after recombination of electrons and nuclides. After the shock front has decelerated to a level, where individual velocities of particles are relevant compared to the velocity of the shock wave, the SNR disperses into the ISM.

In this violent scenario, dust is produced in significant quantities, as it was shown by observation and calculation in early work [106]. Theoretical approaches for dust production are Classical Nucleation Theories (CNT), where dust is initially formed as critical cluster to overcome the condensation barrier of gas, which in the end leads to the growth of clusters to macroscopic size by accreting more and more material. However, CNT does not involve chemical reactions that are needed for the formation of clusters. Chemical Kinetic Theory (CKT) contains chemical reactions as well as molecule formation [98, 97]. Further studies quantified the amount of hot dust and reveiled that a large contribution by cold dust was not noticed by former oberservations and calculations [24, 45, 17]. Cold dust (20 K - 40 K) in contrast to hot dust ($>$ 40 K) is only visible in the far infrared or the sub-mm range, whereas most telescopes work in the near and mid infrared. Cold dust in large quantities was therefore overseen for long time. Detection of cold dust is even today challenging, because large quantities of interstellar dust between the SNR and the telescope could overlay a possible cold dust signal.
Dust production models are confirmed by observation of freshly formed dust in SN2010jl [42], in SN1987 [53] and in Cassiopeia A [93] amongst others. Signatures, needed for the detection of ongoing dust formation, are the onset of thermal emission of dust grains, shifts in the emission profile of the object and a decrease in optical luminosity, coincident with an increase of luminosity at longer wavelengths [74].

In addition to the already mentioned CCSN, dust is also produced in an ECSN [38], in SN IIP [98], in Pop III SNe, which are related to pair-instability supernovae [84], and inherently in shock waves [31]. The typical yield for dust by CCSNe range from 0.01 $M_\odot$ to 1 $M_\odot$ of dust, depending on the initial stellar mass and composition, the type of the SN and on the model used for calculation (see Table a).

Model	Progenitor Mass	Dust Mass
Kozasa [64]	15 $M_\odot$	0.33 $M_\odot$
	20 $M_\odot$	0.68 $M_\odot$
Todini [106]	15 $M_\odot$	0.45 $M_\odot$
	20 $M_\odot$	0.08 $M_\odot$ - 0.7 $M_\odot$
	25 $M_\odot$	0.08 $M_\odot$ - 1.0 $M_\odot$
Nozawa [84]	20 $M_\odot$	0.57 $M_\odot$ - 0.73 $M_\odot$
Bianchi [12]	15 $M_\odot$	0.28 $M_\odot$
	20 $M_\odot$	0.40 $M_\odot$
	25 $M_\odot$	0.62 $M_\odot$
Cherchneff [24]	20 $M_\odot$	0.10 $M_\odot$ - 0.16 $M_\odot$
Sarangi [98]	15 $M_\odot$	0.04 $M_\odot$
	25 $M_\odot$	0.09 $M_\odot$
Gomez [45]	15 $M_\odot$ - 20 $M_\odot$	0.1 $M_\odot$ - 0.7 $M_\odot$

Table a: Dust production from SNe for different progenitor masses and different models. For details about model parameters like metallicity or mixing, references are given. Table adapted from [24].

Another possible production site for dust is a thermonuclear supernova. Dust production could affect the measured light curves of SNIa which are routinely used as cosmic distance gauges. TNSNe feature a harsh environment for dust production, since the ejecta is more heated than for CCSNe, which in the end leads to a higher grain destruction rate. In addition to the higher destruction, the density of the expanding material drops faster than for CCSNe, which reduces the condensation rate. Theoretical models, as well as observation, show that TNSNe do not produce dust in significant quantities [45].

Violent environments, unavoidably linked with the production of dust in SNe, cause also destruction of dust. Hard thermal sputtering, induced by the reverse shock wave, efficiently reduces the size of the dust grains [12]. Furthermore, thermal sputtering can lead to full destruction of smaller dust grains, whereas larger grains survive the reverse shock. Dust destruction is highly dependent on the ejecta density, the relative velocity between the ejecta and the reverse shock, the cooling efficiency of the SNR, the metallicity, and the size and composition of the dust grains [102]. Grains, surviving the reverse shock in CCSNe, are typically larger than 0.1 μm before sputtering. Smaller grains are sputtered to sizes in the nm range, which are not further considered as ISD. Therefore, most of the ejected dust by mass is not destroyed by the reverse shock [42]. Fe grains are most resistant against thermal sputtering, whereas silicates or carbon grains are efficiently sputtered [101].

In contrast to explosive scenarios, stellar evolution is known to produce dust in the AGB-phase of medium-mass stars. As pointed out before, AGB stars show frequently occuring thermal pulses within their AGB-phase. These pulses lead to mass loss by ejection of material into the ISM. The velocities are much smaller compared to CCSNe, where shock waves lead to the ejection of material. Therefore, the ejected material accumulates around the pulsating star as a thick layer, observable by the emission of light from the dust particles [4].

This circumstellar dust layer features excellent conditions for dust grain formation. The temperature around an AGB star is sufficiently cool to allow coagulation of the ejected gas. Furthermore, the densities are high enough to ensure efficient condensation [27]. Hence, grain formation in AGB stars is highly efficient and comparable to the dust yields of SNe after destruction by the reverse shock wave [121]. Initial mass and nucleosynthesis dependent grain composition is a distinctive feature of AGB stars. Depending on the surface C/O ratio and therefore on the initial mass of the star and the current phase of nucleosynthesis, the composition of the major part of the dust grains is either C- or O-rich. Typical molecules are carbon or carbides for C-rich stars and silicates or alumina for O-rich stars [27].

Different stellar dust production sites were evaluated for the purpose of producing a possible ^{60}Fe signal on Earth by ISD. Now, the amount of ^{60}Fe produced in each of the scenarios has to be evaluated. ^{60}Fe is produced by neutron capture on stable Fe. Substantial production of ^{60}Fe requires high enough neutron densities that the production reaction ^{59}Fe(n,γ)^{60}Fe is more frequent than the decay ^{59}Fe(β)^{59}Co, and temperatures low enough that the destruction of ^{60}Fe by photodisintegration is low. The amount of neutrons for a significant build-up of ^{60}Fe in stellar nucleosynthesis has to be in the range of 10^{10} cm^{-3} - 10^{12} cm^{-3} [69]. These conditions are fulfilled for different environments, e.g. by the s-process in stellar shell-burning. Convective shells play a major role in synthesizing ^{60}Fe. Freshly synthesized ^{60}Fe is transported to cooler regions in the star, where no destruction by photodisintegration or neutron capture occurs. Furthermore, new material for neutron-liberating reactions is transported to hotter regions in the star.

CCSNe eject between 10^{-4} M$_\odot$ and 10^{-5} M$_\odot$ of ^{60}Fe, mainly depending on the initial stellar mass [69, 117, 25]. The highest contribution to the ^{60}Fe abundance comes from He and C convective shells, whereas the contribution of explosive nucleosynthesis plays only a minor role. The overall contribution to the Fe budget of the universe is smaller compared to SNIa, but much higher compared to AGB stars (see Figure 2.6). ECSNe are also known as ^{60}Fe producers and are often considered as the source for the ^{60}Fe signal in the former measurements on Earth [114, 38].
TNSN produce highest amounts of Fe (see Figure 2.6) and also ^{60}Fe in moderate to low quantities [100, 38]. The highest possible amount of ^{60}Fe produced in a TNSN is of the order of 10^{-7} M$_\odot$, at least three orders of magnitude lower than for CCSNe. Since TNSNe produce dust in insignificant quantities, this source is ruled out. However, TNSNe contribute to the overall ^{60}Fe budget of the ISM.
AGB stars synthesize ^{60}Fe, as well as dust, in high quantities and are therefore a viable candidate, besides CCSNe, for an ^{60}Fe signal from ISD. One has to point out here that AGB stars eject their synthesized material by winds and not by shock fronts. Therefore, the expansion of the material is limited. See Figure 2.5 for the dust production in the AGB stars.

To compare the contribution of AGB stars and CCSNe to the galactic ^{60}Fe budget, one has to weight the amount of produced ^{60}Fe with an initial mass function and the stellar lifetime. The initial mass function describes the mass distribution of stars forming by the collapse of a progenitor gas cloud. The stellar lifetime is mainly determined by the initial mass and is shorter for heavier stars. Hence, heavier stars that undergo SN release considerably faster their synthesized material. AGB stars contribute only to 3% to the galactic ^{60}Fe budget compared to SNe [72] and are therefore also ruled out as major source for ^{60}Fe stardust on Earth.

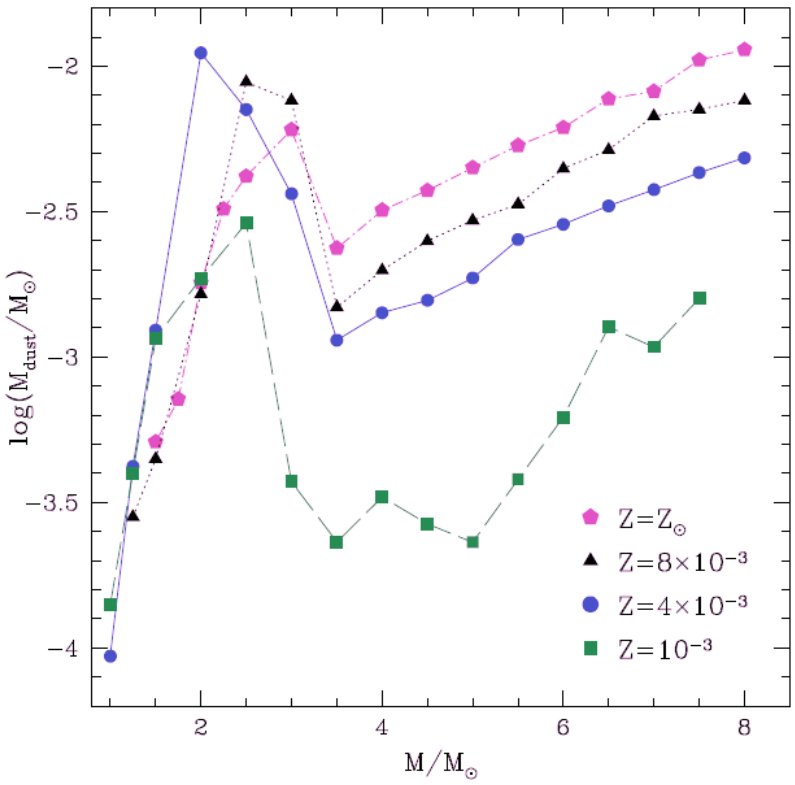

Figure 2.5: Total dust mass produced by AGB stars for different initial stellar masses and for different metallicities. Differences for decreasing metallicity, starting from the solar metallicity, are aparent. Figure taken from [26].

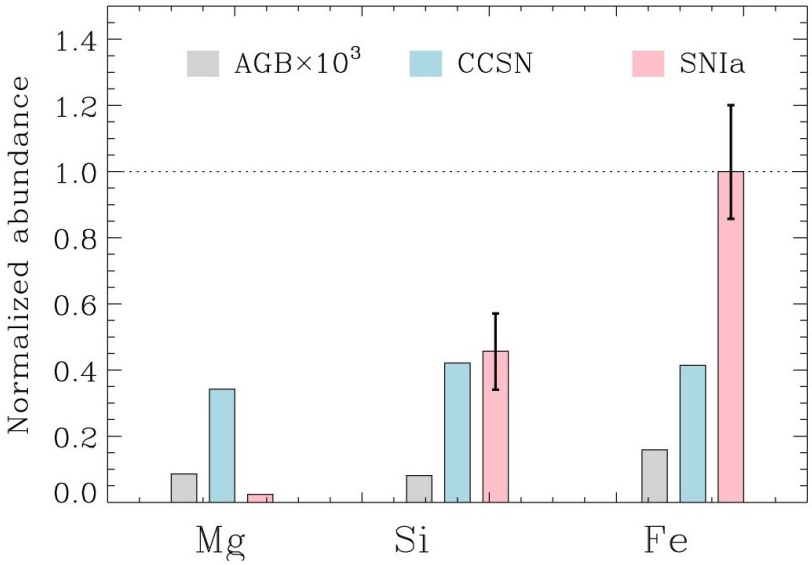

Figure 2.6: Element production by different stellar sites. TNSN produce most of the Fe in the universe, whereas AGB stars only play a minor role for the Fe budget. Abundances are scaled to Fe for SNIa and error bars indicate the variation of abundances within the sources. Figure taken from [30].

2.3 Cosmogenic Origin of ^{60}Fe

Stellar environments feature a natural vicinity for the production of ^{60}Fe and dust. Another production site is irradiation of interstellar and interplanetary dust by cosmic rays.

^{60}Fe is produced by nuclear reactions of Solar Cosmic Rays (SCR) and Galactic Cosmic Rays (GCR) on targets containing significant amounts of Ni. ^{60}Fe-producing reactions happen on stable ^{62}Ni and ^{64}Ni with isotopic abundances of 3.6% and 0.9%, respectively [61]. Another natural production path would be double free neutron capture on stable Fe. By knowing the cosmogenic production rates of ^{60}Fe, it is possible to estimate an upper limit of cosmogenic ^{60}Fe production in cosmic dust or meteoroids. For this estimation, the production rates for SCR and GCR are evaluated (see Table b and more detailed Table m). Production rates are highly dependent on the size of the object, since the primary cosmic ray particle induces, by spallation reactions on the surface, a shower of secondary particles which penetrates deeper into the target [34]. Secondary neutrons can lead to highly efficient ^{60}Fe production by double neutron capture on stable Fe nuclei. A secondary particle shower is only induced at significant quantity, if the target itself is large enough [78]. For IDP's and MM's in the micrometer range, there is no build-up of a secondary shower and for this reason, nuclear reactions induced by primary cosmic rays, which are mostly protons, are the dominant production mechanism.

Target Size [μm]	**Production Rate [dpm/kg]**
2.5	0.40
10	0.48
50	0.50
100	0.50
GCR	0.12

Table b: Cosmogenic production rates for ^{60}Fe by SCR interactions on pure Ni targets in units of disintegrations per minute per kg target material [dpm/kg]. Different target sizes are assumed at a SCR rigidity of 125 MV and a proton flux of $100\,\mathrm{cm^{-2}\,s^{-1}}$, which represents a conservative upper limit to recent work [107]. GCR production yield considerably less ^{60}Fe than SCR. Data gratefully provided by R. Trappitsch and I. Leya [108].

As typical cosmogenic production rate for spallation on Ni, 0.51 dpm/kg Ni is assumed [108]. On the one hand, this production rate neglects secondary neutron production for the estimation of ^{60}Fe production, whereas on the other hand, changes in the assumed solar spectrum, typical sizes of later analyzed objects below 50 μm and size-dependent GCR production would lead to a lower value for the production of ^{60}Fe. This production rate could be rewritten in the form of number of produced ^{60}Fe atoms per unit mass of target material. The production rate of 0.51 dpm/kg Ni corresponds to 10^{12} atoms of ^{60}Fe per kg Ni as target. One has to mention here that this production rate and the following calculations are only applicable for small dust grains, grains within the solar system and for grains with chondritic composition. For other compositions, the obtained results could be scaled by the respective abundance of Ni.

After this conservative upper limit for the production of ^{60}Fe is established, the expected amount of ^{60}Fe in the later introduced sample material could be calculated. The amount of Fe and Ni is assumed to be purely cosmogenic to yield an upper limit on the cosmogenic ^{60}Fe production in the sample material. Terrestrial Ni and Fe lead to a smaller amount of the expected cosmogenic Ni and Fe in the sample. Furthermore, the amount of ^{60}Fe by SN is assumed to be in the same range as for the already detected SN induced concentration [59].

At first, one has to estimate the amount of cosmogenically introduced stable elements. Here, 1 mg of cosmogenic Fe is assumed and the amount of comogenic Ni is calculated by using typical elemental abundances in chondritic meteorites [116, 44, 103]. For this project, the abundances shown in Table l are used to calculate upper limits. 1 mg of cosmogenic Fe corresponds to 58 μg of cosmogenic Ni in chondritic meteorites, which could then be scaled by individual factors for different initial masses. 58 μg of cosmogenic Ni would lead to $5.8 \cdot 10^4$ atoms of ^{60}Fe in the sample material.

In contrast to the production of ^{60}Fe by cosmic rays, where Ni as target element is needed, the amount of ^{60}Fe with SN origin in the sample material is independent of any element abundances. As an upper limit for the introduction of SN ^{60}Fe, the flux of already detected SN ^{60}Fe is used [34]. For an adopted ^{60}Fe flux of $0.5 \cdot 10^8$ at/cm^2 over 0.9 Myr, the amount of ^{60}Fe is estimated. The collected surface area of the sample material, which is normalized to one year of precipitation, yields $4 \cdot 10^{12}$ atoms over 0.9 Myr, which leads to $4 \cdot 10^6$ atoms of ^{60}Fe in the collected sample material.

This primitive estimation has some implications: At first, the influx of ^{60}Fe has to be as high as for the already detected signal. This is in general not the case, because the high flux 2 Myr ago was triggered by several SNe and the already existing abundance of ^{60}Fe in the ISM between Earth and these SNe. This high flux of ^{60}Fe towards the Earth seems to be exceptional. Furthermore, the high flux was obtained over 0.9 Myr. The current sample comprises only the last ten years of precipitation, where short-term modulation plays a significant role compared to the long period of hundreds of thousands of years. Nevertheless, this approximation is only used for a first estimation of the maximum amount of ^{60}Fe in the sample. The amount is higher than the detection limit of AMS and therefore, a measurement is in principle feasible with unknown outcome.

All in all, the maximum amount of cosmogenically produced ^{60}Fe could be more than one magnitude lower than the amount of SN ^{60}Fe. Though, these values represent only upper limits and as already stated, these values are only primitive estimations. Considering the highest sensitivity of the later introduced AMS detection technique and the unique sample material, which is also described later in detail, the measurement of ^{60}Fe is desirable to get new insight into the physics of interstellar and interplanetary dust and the influx of material from outer space.

The last part of this chapter is dedicated to the influx mechanics of extraterrestrial material on Earth and possible origins of dust particles for cosmogenically or stellar produced ^{60}Fe.

2.4 Dust Origin and Influx on Earth

Stellar and cosmogenically produced ^{60}Fe is present in the universe. In this part, different origins of possibly detectable ^{60}Fe on Earth are investigated within the frame of the solar neighborhood. Furthermore, the influx of this material on Earth is briefly described with respect to the different initial conditions of the dust particles.

2.4.1 Local Interstellar Cloud, Local Bubble and Interplanetary Dust

^{60}Fe is produced in stellar and explosive scenarios as well as by cosmic ray reactions in dust particles. In the following, possible sources for an interstellar and interplanetary ^{60}Fe signal on Earth are discussed.

The solar system is currently embedded in a low density ($n_H = 0.3\,cm^{-3}$) and warm (6900 K) cloud of gas and dust [37]. The so-called Local Interstellar Cloud (LIC) is currently moving perpendicular to the movement of the solar system and the solar system will leave this vicinity in 10^4 yr. Possible origins of the LIC are fragmentation of the Loop I Bubble or detachment from the interaction zone of two super bubbles [58]. The LIC with a gas to dust ratio of 100 for H is rich in heavy elements that are concentrated in dust (gas to dust ratio for Fe around 0.05) [58, 18]. The absolute abundance of Fe is around 30 atoms normalized to 10^6 atoms of H.

Further on, the LIC is embedded in the Local Bubble (LB) which is a hot cavity (T = 1 MK ; $n_{Plasma} = 0.005\,cm^{-3}$) in the interstellar medium. The LB is 14 Myr old and was produced by several (14 - 20) SNe from the Lower Centaurus Crux and Upper Centaurus Lupus subgroups [9, 40] which are combined in the Scorpius Centaurus OB association. The formation of the LB by these SNe is believed to coincide with the deposition of ^{60}Fe [19] that was detected in a ferromanganese crust from the Pacific by AMS [59].

Since the LB producing SNe are believed to deposit already present or freshly synthesized ^{60}Fe from the ISM on Earth, the LIC which was possibly formed by the interaction of the LB with the Loop I Bubble [18] could also accumulate ^{60}Fe. By passing the LIC, the solar system and therefore Earth could incorporate ^{60}Fe in the form of ISD.

Dust grains are abundant in the LIC with different sizes. Smallest grains are not able to penetrate into the solar system due to deflection because of their relatively high charge to mass ratio. Nevertheless, grains can become larger by coagulation and are then able to reach the solar system with isotopic information of the LIC [57].

Another possible source for ^{60}Fe, which could be captured by Earth, are IDP's. IDP's originate from dust producing and emitting sources inside or near the solar system. Locations for dust emissions are the Oort Cloud beyond the heliosphere, the Kuiper Belt surrounding the solar system, the Asteroid Belt at 3 AU or comets. Dust between the planets in the solar system is often referred to as Zodiacal Cloud.

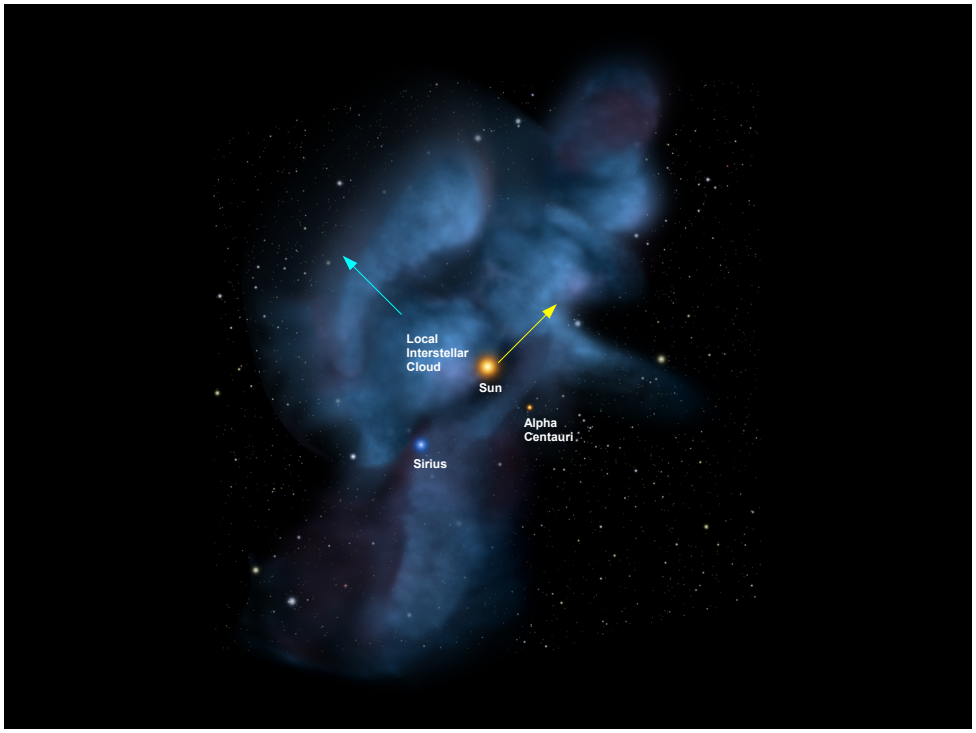

Figure 2.7: The Local Bubble, containing the solar system and the Local Interstellar Cloud, is depicted. Movement of the solar system and the Local Interstellar Cloud are indicated. The picture comprises 40 lyr in each direction. Figure modified from [88].

Particles from the Oort Cloud in the micrometer range are mostly ejected from the solar system and therefore do not contribute significantly to a possible IDP signal on Earth [7].
Inside the solar system, particles from the Kuiper belt have highly eccentric orbits, leading to significant particle losses. Kuiper belt objects contribute only slightly to the extraterrestrial dust budget on Earth [81].

The Asteroid Belt between Mars and Jupiter, as well as comets, are the most likely candidates for extraterrestrial dust grains found on Earth. Historically, the contribution of the asteroid belt was thought to dominate the IDP flux on Earth. Recent studies favor cometary over asteroidal origin. The observation of the albedo and spectral gradient of the Zodiacal light and comparing these properties with possible parent bodies leads to the conclusion that comets are almost exclusively the source for IDP's [119].

Interstellar dust, as well as interplanetary dust, contain a possible ^{60}Fe signature. They differ in their isotopic ratios of radionuclides produced by irradiation compared to the abundances from supernovae among others. This has to be investigated by measurements of these isotopes to pinpoint the origin of extraterrestrial dust found on Earth. To end this chapter, their relative difference in influx mechanics is outlined and the deposition on Earth is described.

2.4.2 Influx Mechanics and Deposition on Earth

The production mechanism and possible origins of interstellar and interplanetary dust have been established in the previous chapters. Here, the influx mechanics of dust particles with different origins are discussed.

Interstellar dust is initially far away from the solar system. In principle, dust and plasma from a SN can enter the solar system, if the pressure of the incoming material is higher than the solar pressure. For plasma, this is only possible for very near SNe [33] which would cause major biological effects on Earth. Direct deposition could therefore be excluded for the search of SN material on Earth. For decoupled dust instead, larger distances are possible because of their lower interaction with the heliosphere. Therefore, dust has to decouple from the plasma, which is possible for dust grains in the micrometer range [85]. ISD is already present in the solar system [48, 104].

The main interaction of dust, coming from the outside of the solar system, with the heliosphere and massive objects in the solar system are gravitation, radiation pressure and deflection by the Lorentz force in electromagnetic fields due to their effective charge [5].
For particles inside the solar system with defined bound motion, Poynting-Robertson drag [94] reduces their angular momentum over long time scales and therefore their radius of motion. This causes particles to spiral inwards and eventually be captured by planets or the Sun.

Coming towards the vicinity of Earth, also Earth's magnetic field, motion and gravitation has to be considered [39]. By entering Earth's atmosphere, dust particles are altered due to different processes. Most critical parameters of the dust particles are their size, chemical composition, entrance velocity and angle of entrance [21].
Dust particles in the atmosphere are exposed to friction, which leads to a heat-up of the dust grains. Thermal ablation due to melting has to be considered for distinct dust grains as well as (partial) evaporation of mass. In combination with thermal sputtering by collisions with the gas molecules of the atmosphere, an effective reduction of size and mass of the dust grains is achieved. Since these processes are coupled to the size, mass and velocity of the particles, which themselves are changing during these processes, a precise description with robust predictions is difficult [92]. For this project, detailed knowledge about these processes and the distribution of sizes and masses is not crucial, since the sample sets divide only the initially available material in larger ($r > 1\,\mu$m) and smaller ($r < 1\,\mu$m) particles.

After the dust grains decelerated to the point, where thermal sputtering, as well as ablation, are no longer significantly changing the size and mass of the objects, atmospheric processes transport and distribute these dust grains all over the world. Particle sizes range from nanometers to roughly $100\,\mu$m in radius. The distribution of particles is determined by winds, seasonal changes of air streams and wet-dry precipitation events, that all has to be tackled by atmospheric models.

In the following chapter, the sample used for this project is introduced as well as developed and applied chemical techniques to separate different isotopes with special focus on the Fe content.

3 Chemistry and Sample Characterization

Extraterrestrial material, possibly containing stellar and cosmogenically produced ^{60}Fe, is deposited on Earth. As discussed before, several different geological reservoirs are able to incorporate ^{60}Fe and to store it for long times.
In the following, the unique reservoir of Antarctic snow is described and it is discussed why Antarctic surface snow was chosen for this project.

3.1 Antarctic Snow as Geological Reservoir

Antarctica is unique as geological reservoir, because it is well-separated from other continents and far from any civilization. Therefore, anthropogenic influences are minimized. Nevertheless, the potential for terrestrial contamination during e.g. sampling or further chemical treatment must be considered. Since the ^{60}Fe concentration on Earth is below the detection limit, except in geological reservoirs, any contamination from the environment could be neglected. Dilution by stable Fe, which could be a problem for later AMS measurements, is reduced by the use of non-ferrous materials.
Another advantage of Antarctic snow over other reservoirs, like deep-sea crusts or sediments, is that Antarctic surface snow is unaffected by ocean currents, tides, continental drift or seismic activity. Antarctic snow could be affected by winds from South America as well as from Africa. This effect should be negligible compared to the much higher dilution of other reservoirs used in the past and especially due to the large distances to these continents of several thousand kilometers.
Dating of reservoirs is in some cases necessary, otherwise no time resolution of events could be obtained by measurements. For deep-sea crusts and sediments, dating is challenging due to varying sedimentation rates and the dependence on models for geomagnetic field reversal or biological markers [71]. For Antarctica, precipitation rates have been investigated before and volcanic eruptions in the past can be used as benchmarks [86]. Therefore, dating is in principle possible for material from Antarctica.

For this project, Antarctic surface snow was chosen as appropriate sample material.
Firstly, no dating is needed for surface material. The collected material comprises less than ten years, which is a much shorter time period compared to stellar or cosmic time scales and could be assumed to be recent material. Antarctic deep-cores can only be dated back thousands to several hundred thousand years, because of the high precipitation rates in Antarctica (mm/yr) [86, 15] compared to low sedimentation rates in deep-sea cores (m/Myr) [71]. A search for the already known SN entry $\approx 2\,\mathrm{Myr}$ ago [59] would therefore be challenging.

Secondly, the concentrations of stable Fe (and Mn) are small (ng/g range) and have not changed over the past 5000 yr [120], which prevents dilution of a possible ^{60}Fe (or ^{53}Mn) signal. Furthermore, past studies of Antarctic micrometeorites (AMM's) show that Antarctica is indeed suitable for collecting cosmic dust and particles [44]. Having only small concentrations of stable isotopes is also a disadvantage, as this requires concentration of large initial sample masses in order to yield an adequate sample for an AMS measurement and for chemistry.
Thirdly, any contribution from dissolved Fe in the Antarctic sea [2] is averted by choosing an inland location. By collecting surface material, it is also guaranteed that no unknown incidents in the past like floodings, hurricanes or aridity has altered the collected material.

500 kg of surface snow were collected by collaborators from the Alfred-Wegener-Institut near the Kohnen Station in Antarctica. The Kohnen Station in Dronning Maud Land (75°00'S, 00°04'O, 2892 m) is a German research station in Antarctica since 2001 (see Figure 3.1). The amount of collected snow represents 8 m^2 of surface material for one year of precipitation using the known precipitation rate of 62 mm w.e per year [15].
These 500 kg were shipped frozen to Munich for chemical purification and AMS measurements of ^{10}Be, ^{26}Al, ^{41}Ca, ^{53}Mn and ^{60}Fe. After arriving in Munich, the frozen snow was melted in a cleaned stainless steal basin and filtered afterwards. Filter pore sizes were 12 μm - 15 μm and subsequently 2 μm - 3 μm which are the typical ranges for IDP's. By filtering the water, the sample is divided into larger and smaller particles, which is important for a later evaluation of different ablation models. The filters and the filtered water were separated and further treated by collaborators in Dresden, Germany and in Vienna, Austria, respectively. The water was stored in several plastic containers at pH 1 after addition of HNO_3.

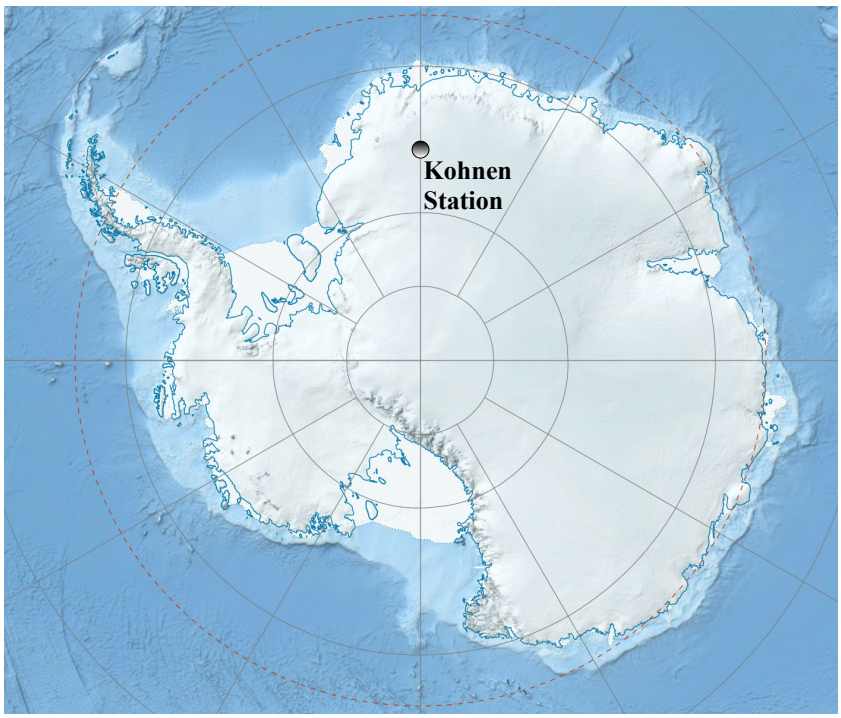

Figure 3.1: Map of Antarctica. Kohnen Station in Dronning Maud Land is indicated. Samples were taken by collaborators from the Alfred-Wegener-Institut.

3.2 Chemical Separation in Dresden

The filters were treated at the Helmholtz-Zentrum Dresden-Rossendorf (HZDR). Visible structures in the filters were handpicked and analyzed by EDX (Energy Dispersive X-ray spectroscopy). Through EDX, the element content of each collected grain is determined which could be compared to typical values of extraterrestrial material. EDX in combination with characteristic visual features from the atmospheric entry are used to determine the origin of the collected grains. See Figure 3.2 for illustration of an exemplary grain and Table o for the element content of three exemplary grains. The residual sample consists of 9 filters with pore size of 2 μm - 3 μm and 4 filters with pore size of 12 μm - 15 μm. The filters, including small particles, were incinerated (up to 650°C), particles digested and radionuclides of interest were radiochemically separated from the matrix and each other [77].

The ashes from the incineration are transferred to a Teflon bomb (Parr pressure bomb) with 2 ml HNO_3 (70%) each, then 2 ml $HClO_4$ (70% - 72%) and 7 ml HF (48%) are added to each sample. After 24 h at 150°C, the solution is evaporated to dryness and the residue redissolved in HCl (10.2 M). The samples are combined and stable nuclide carriers (Be, Ca, Mn, Fe) are added. An ion-exchange column (20 cm height, 1 cm diameter, Dowex 1X8) is washed with 20 ml of H_2O and afterwards conditioned with 20 ml of HCl (10.2 M). The sample is put on top of the column and the first fraction, containing Be, Al, Ca and Ni is eluted with 18 ml of HCl (10.2 M). To elute Mn, 100 ml of HCl (7.1 M) is used. In the end, Fe is eluted by 27 ml of H_2O. The eluted Fe is then precipitated by the direct addition of NH_3 (aq, 25%) and purified by rinsing the precipitate. Fe_2O_3 is generated by igniting the precipitate at 600°C.

The total amount of concentrated HCl used for this chemistry is 120 ml, considering the different concentrations used for chemistry to be still concentrated HCl. Concentrated acids contain minor fractions of dissolved metals and are therefore considered to be contaminants for ultra pure ion-separation chemistry. A modified sample preparation chemistry for Fe with reduced amounts of acids and additional purification is developed on the basis of the previously described method.

The amount of material in the filters (after removing visible structures) was determined by Inductively Coupled Plasma Mass Spectrometry (ICP-MS) from a 5% aliquot. Masses are displayed in Table c. The measured amount of Fe was confirmed after the chemistry by weighing the separated Fe fraction. The preparation of the filters resulted in two AMS samples and two chemistry blanks (see Table g).

	Be	**Al**	**Ca**	**Cr**	**Mn**	**Fe**	**Ni**
Filter Sample	< 10 μg	3.4 mg	1.5 mg	n.a.	76 μg	4.1 mg	188 μg
Filter Blank	< 10 μg	198 μg	1.2 mg	n.a.	< 10 μg	385 μg	< 10 μg

Table c: Element content of the filter samples and the related blank samples from the ashes of the filters. Especially Be, Mn and Ni are barely abundant, whereas higher amounts of Al and Fe are in the sample. For Ca, the usage of the filters resulted in a strong dilution. Note the different mass scales (μg and mg).

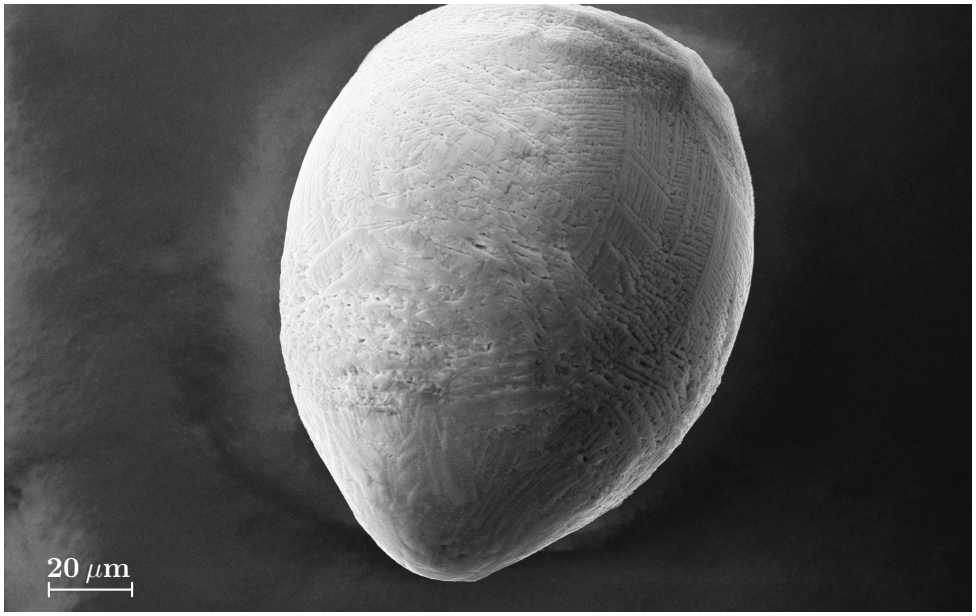

Figure 3.2: Picture of an exemplary dust grain collected from the filter. This grain consists mostly of O, Mg, Si and Fe. The grain is 100 μm in diameter.

Three analytic techniques are used in this project namely ICP-MS, Total reflection X-Ray Fluorescence (TXRF) and EDX.

ICP-MS is a mass spectrometric measurement technique widely used in science. The sample is ionized in a hot Ar plasma which is generated by a high frequency current. Free electrons are accelerated by alternating magnetic fields from an induction coil and subsequently ionize Ar atoms. More and more electrons are generated which ionize in the end the sample to single charged positive ions. These ions are focused and later analyzed by a mass spectrometer by their m/q. This technique is limited by molecular and atomic interference, but it operates over many orders of magnitude in concentration (down to ppb level) and it is less cost-, time- and labor-intensive than AMS.

TXRF uses monochromatic x-rays to determine the element content of a sample. The sample is placed on a carrier disk and irradiated with monochromatic x-rays under smallest incident angles (typically 0.05°) for total reflection. The penetration depth of the x-rays is limited to a few nm by total reflection, which leads to high signal to noise ratios. Atoms are ionized by the incident x-rays. Afterwards lower electron states are occupied by electrons in higher states by de-excitation. Characteristic fluorescence light is detected in a photon detector and could be attributed to the specific composition of the sample material. TXRF is non-destructive and therefore suitable for surface contamination monitoring and element determination in the ppm to ppb range.
For EDX, a beam of photons or charged particles is directed towards the target, where electrons from an inner shell will be excited. Characteristic x-rays are emitted through de-excitation of electrons from an outer outer shell. This discrete x-rays are detected and assigned to specific elements in the sample.

3.3 Chemical Separation in Vienna

The preparation of the water includes several additional steps which were developed and tested within the scope of this project.
Initially, evaporation and therefore concentration of the sample is needed to extract the elements efficiently afterwards. After concentration, the already existing element separation procedure [77] is slightly modified for smaller sample masses and for less contamination of the sample by the chemistry. After the establishment of the extraction method, samples are prepared and measured by AMS at the MLL in Garching.

Evaporation is the first step needed to reduce the volume of the water. For this purpose a rotary evaporator (Rotavapor R-150) is used because of its high and uniform evaporation speed. The water, divided in 10 l fractions, is concentrated to 80 ml for each fraction in the rotary evaporator. Simultaneously, ICP-MS and TXRF measurements are performed on each fraction of the concentrate at the Atominstitut to determine the absolute amount of each element. TXRF was only used to cross-check the determined values from ICP-MS. See Table d for the measured abundances. Here, in the water sample as well as in the filter samples, Be is only barely abundant.

	Be	**Al**	**Ca**	**Cr**	**Mn**	**Fe**	**Ni**
ICP-MS	< 10 μg	n.a.	21.4 mg	54 μg	166 μg	412 μg	198 μg
TXRF	< 10 μg	n.a.	17.7 mg	43 μg	187 μg	709 μg	258 μg

Table d: Element content of the water. Determined masses by ICP-MS and TXRF are given. TXRF shows slight differences to the ICP-MS measurement, but in general confirms the values from ICP-MS. Especially for Fe, the variation between both measurements is large. Note the different mass scales (μg and mg).

Next, modifications of the standard separation procedure are developed and tested. These modifications are needed because of small sample masses (sub milligram) to avoid contamination. Separation of Fe from Ni, Mn, Cr, Ca, Al and Be is achieved by ion-exchange chromatography (Dowex 1X8, 100-200 Cl^-). By a small column length of 6 cm, losses through the column, the amount of resin needed for the separation and significantly the amount of acids and water needed for the procedure are reduced. For this project, the separation of other elements in this first step is not crucial and therefore smaller columns could be used without deteriorating the separation capability of the Fe-Ni separation, which is easiest to separate on the column because of the large difference in required acid concentration [65]. Afterwards, the separation of Mn from Cr among others is carried out, which is not part of this thesis. The following chemistry steps are all performed "carrier-free", as long as the exact amount of Fe in the original sample is not determined more precisely.

The following Fe-Ni separation is only applicable for the case of oxidized Fe. Fe(III) is efficiently separated by the column from Ni, whereas this is not the case for Fe(II). For the Antarctic snow sample, one has to assume a mixture of Fe(II) and Fe(III). Therefore, an additional oxidation

step before ion-exchange chromatography was carried out. By adding H_2O_2 to the already acidified sample overnight, Fe is oxidized without introducing any contamination or deteriorating the residual sample. After oxidation, the sample is processed as described below.

The resin is prepared and conditioned with concentrated HCl (10 M). The sample is then dissolved in HCl (10 M) and put on top of the column. The first eluate (5 ml HCl (6 M)) contains Be, Al, Ca, Cr, Mn and Ni. This fraction is stored for further chemical separation steps. The second eluate (2 ml HCl (3 M)) is used to purify the later sample by removing interfering isotopes. The last step is to eluate Fe with 5 ml of H_20 (tridest.), which is easy to collect because of its yellowish color under acidic conditions.
This separation reduces the amount of Ni in the sample from hundreds of micrograms (same order of magnitude as Fe) to the ppm to ppb range. Still, the amount of Ni is almost two orders of magnitudes too high for an AMS measurement. To solve this problem, the eluate, containing Fe and reduced amounts of Ni, is passed through another column with the same procedure as described above. This results in a further reduction of Ni by almost two orders of magnitude and is sufficient for AMS purposes. Therefore, the first column is used to separate the bulk of elements from Fe and the second column is used to purify the sample to the level needed for AMS.
Dissolved Fe(III) precipitates under alkaline conditions (pH 8) as $Fe(OH)_3$. Hence, NH_3 (aq, 25%) is added by diffusion over hours to minimize contamination. After rinsing and centrifuging the precipitate three times with H_2O (tridest.) at 5,000 rpm for 10 min each, $Fe(OH)_3$ in H_2O is heated till dryness and later ignited at 600°C for two hours to yield Fe_2O_3.

This process is tested by using standard solutions from Roth (1000 μg/ml), analytic chemicals and radiotracers. Typical proportions are 150 mg $Ca(NO_3)_2$, which yields roughly 20 mg Ca, mixed with 1 mg Fe, 200 μg Ni, 200 μg Mn and 50 μg Cr. This resembles the actual content of the snow water sample including an excess of nitrates.
Radiotracers are used to monitor the separation on the column. The radiotracers, used for this project, are ^{51}Cr, ^{54}Mn and ^{59}Fe (see Table e). It would be important to use radioactive Ni as monitor for the Fe-Ni separation, however, radioactive Ni isotopes either decay directly to the ground state or have half-lives to short to use them as tracers.
γ-photons from the decay of the excited daughter nucleus are detected through γ-ray spectroscopy by a Ge detector available at the Atominstitute. The measurement was performed with the same geometry for all samples, whereas an geometric efficiency calibration for this specific geometry was not available. Full separation of Mn and Cr and therefore Ni from Fe is obtained (see Figure 6.1 in the Appendix).

Radiotracer	**Half-life**	**Decay mode**	**γ energy**
^{51}Cr	28 d	EC	320 keV
^{54}Mn	312 d	EC	835 keV
^{59}Fe	45 d	β^-	200 keV, 1100 keV - 1300 keV

Table e: Radiotracers which are used to monitor the separation process. Radiotracers are produced by the TRIGA MARK 2 reactor of Atominstitut, Vienna. Decay data is obtained from the Laboratoire National Henri Becquerel (LNHB).

After establishing the separation procedure, the amount of material lost during rinsing and centrifuging is quantified. Therefore, all washing solutions from several samples are collected and evaporated. Evaporation of this slightly alkaline solution of HCl from the column and NH_3 from the diffusion yields white ammonium chloride (NH_4Cl). By adding small amounts of HCl, the medium turns acid and any Fe content is visible by its yellowish color. This yellowish color could be compared to a solution of artificial NH_4Cl with added Fe. This test shows that the amount that is lost in the rinsing process from the total of 5 mg of Fe is much less than 50 μg. Therefore, the rinsing process leads to losses below 1%, too small to be considered. This quantification could also be done by the usage of the mentioned radiotracers.

It has to be pointed out that some other modifications were tested but discarded.
Oxidation by concentrated HNO_3 would be more convenient than NH_3 diffusion because of faster processing. Direct evaporation after the ion-exchange column yields $FeCl_3$ which could be oxidized by adding subsequently 300 μl of concentrated HNO_3 and further evaporation. Nevertheless, highly concentrated acids contain non-negligible amounts of dissolved metals. Since any Ni content in the acid will remain in the sample because of evaporation, this possibility is discarded. Another procedure which is not considered is direct neutralization. The acidic solution after the column could be neutralized and alkalized by direct addition of NH_3. For the same reason as for the HNO_3 oxidation, this step is not considered because any impurities in the NH_3 solution could contaminate the actual sample. For larger samples (5 mg and more) direct neutralization yields no considerable increase in background as seen in the samples from Dresden.

Ni contamination is efficiently suppressed by using ion-exchange chromatography twice. Another way of suppressing Ni is to use organic-phase extraction before ion-exchange chromatography instead of two columns [29]. Fe is separated from the raw material, which contains Ni, by adding diisopropyl-ether. Fe in the organic phase is then back-extracted to water. This technique is widely used in separation chemistry, but is not chosen for this project because of its drawbacks for small sample masses. Organic-phase extraction is a two step process which can lead to unavoidable losses. Therefore, ion-exchange chromatography is more reliable and efficient for this small sample masses, where losses must be reduced to a minimum. It has to be mentioned that for AMS-untypically large samples, where ion-exchange chromatography is not usable any more because of saturation, organic-phase extraction might be the right tool.

The efficiency of the chemistry, in this case known as recovery, is 80% - 90% for the two column procedure. This was tested on dummy solutions with known amounts of Fe. Compared to the recovery using one long column as used in Dresden (90% up to full recovery), the small columns are slightly less efficient because of the two step process and the smaller amount of material used, but still efficient enough to avoid major losses. By adding carrier solutions to the actual sample, losses of sample material could be reduced further, because the relative recovery of material is higher for larger samples.

The main differences between the two sample preparation techniques are the different amount of acids used, the number of separation steps and the additional purification step for the Vienna sample. Less acids can lead to smaller amounts of contaminating metals in the sample and the additional purification step is possibly able to suppress interfering elements further. The amount of background in each sample is characterized in the following chapters by AMS measurements.

3.4 Sample Characterization

In this section, the different samples used for optimization of the chemical separation of elements are described as well as the final samples.

Any modification of the existing chemical element separation technique requires extensive testing. The background of stable Ni, as well as any ^{60}Fe contamination introduced by the radiochemistry lab, has to be reduced and quantified.
Initial tests (samples Fe 1 - Fe 3) showed that one step ion-exchange chromatography is in principle possible for small sample masses, but the background of Ni is too high to yield sufficient sensitivity in later AMS measurements. The background of Ni is almost two orders of magnitude higher than in commercially available Fe_2O_3 powder, used as lab blank for AMS.
Further tests with samples initially containing radiotracers showed that the usage of radiotracers from the TRIGA reactor in Vienna does not introduce any measurable contamination in the form of ^{60}Fe (samples Fe 4 - Fe 6). The radiochemistry lab in Vienna, as well as the chemistry labs in Munich and Dresden, are free from ^{60}Fe, which was determined by AMS measurements of chemistry blanks and lab blanks.
In addition to NH_3 diffusion, HNO_3 evaporation and direct precipitation were also used (samples Fe 7 - Fe 13). Furthermore, smaller sample masses were tested. The Fe content was reduced from 1 mg over 500 μg to 100 μg without significant loss of material by the separation procedure. Ion-exchange chromatography is therefore suitable, even for smallest sample masses.

All samples up to this point showed the same high Ni background. This leads to the conclusion that one single column does not reduce the amount of Ni enough. Eventually, this results in a loss of sensitivity because of the elevated Ni background in the AMS measurement (sample Fe 14).

This conclusion gives rise to the following assumption: A second column should reduce the residual Ni content to a level appropriate for AMS. Measurements of sample Fe 15 showed a reduction of Ni by two orders of magnitude compared to Fe 14 and at the same level as the lab blank. Table f shows all test samples including characterization and location.

Label	**Lab|Oxidation|Details**
Fe 1 - Fe 3	Vienna | HNO_3 oxidation | one column, no radiotracers
Fe 4 - Fe 6	Vienna | NH_3 diffusion | one column, radiotracers
Fe 7 - Fe 9	Vienna | NH_3 diffusion | one column, decreasing Fe content
Fe 10 - Fe 12	Vienna | HNO_3 oxidation | one column, decreasing Fe content
Fe 13	Vienna | NH_3 direct precip. | one column
Fe 14	Munich | NH_3 direct precip. | one column, compared to Fe 15
Fe 15	Munich | NH_3 direct precip.| two columns, compared to Fe 14

Table f: Classification of test samples used to optimize the modified chemical separation. Details like location of the lab as well as preparation techniques are displayed. Fe 15 and Fe 14 were used for a direct comparison between using one or two columns for Ni suppression.

Fe samples for AMS are often spiked with carriers for chemistry because of small initial sample mass. Initial mass plus added carrier mass gives the total mass of the sample. Some samples are divided into several sub-samples because of a large total sample mass. Typical sample masses for AMS in Munich are between 1 mg and 5 mg for Fe. In addition to that, Ag powder is added to the sample for higher conductivity of the sample in the ion-source during the AMS measurement. Here, all values are given in the form of masses. Another possibility is in the form of number of atoms or in the form of volumes. Masses were chosen because of easier handling during the sample preparation. Therefore, it is important to note that the carrier, as well as the sample, is given in the form of pure Fe and the added Ag powder is pure Ag.

Sample processing and element separation chemistry of the filters and the water resulted in several samples for AMS (see Table g).
Samples obtained from the filters are D_1 and D_2. These belong to the same sample, but are separated due to high total mass. Associated chemistry blanks are labeled as B_D_1 and B_D_2. The initially abundant amount of Fe in the filters is (4.2±0.1) mg.
Concentration and element separation from the water yielded one Fe sample (V_1). Here, two chemistry blanks were prepared (B_V_1 and B_V_2). In contrast to the filter sample, the amount of initially abundant Fe, determined as (0.7±0.1) mg, is lower and more uncertain. Complete uncertainty analysis will be carried out later.
In addition to the samples from Antarctic snow, a lab blank of commercially available Fe_2O_3 powder is regularly used to determine the absolute sensitivity of the setup and to tune the beam for the experiment. This is possible because of unlimited availability of the powder and a constant low concentration of Ni in the powder.
Furthermore, the AMS measurement itself requires a calibrated standard sample with a known concentration of ^{60}Fe. The used standard is labeled as STD and is a in-house produced and cross-calibrated standard for AMS with the concentration $^{60}Fe/Fe = (1.3 \pm 0.3) \cdot 10^{-12}$. Calibration was performed with currently and formerly available standard material.

In the following, AMS as ultra-sensitive tool for radioisotope detection is introduced, specific features of the setup in Munich are highlighted and results of the measurements are discussed.

Label	Sample [mg]	Fe carrier [mg]	Ag added [mg]	Notes
D_1 + D_2	8.2	4.0	20.0	Filter sample
B_D_1	4.1	4.1	10.0	Chem. blank Dresden
B_D_2	3.4	3.4	10.0	Chem. blank Dresden
V_1	2.3	2.0	7.5	Water sample
B_V_1	2.9	2.9	10.0	Chem. blank Vienna
B_V_2	3.5	3.5	10.0	Chem. blank Vienna
Lab Blank	5.0	5.0	10.0	Commercial, Munich
STD	n.a	n.a	n.a	$^{60}Fe/Fe = 1.3 \cdot 10^{-12}$

Table g: Classification of samples obtained from Dresden and Vienna including samples used in Munich. Total sample mass after chemistry including carrier, added carrier for chemistry (both displayed as Fe) as well as later added Ag powder for the sputter ion-source are given. The initial amount of Fe in the sample is slightly higher because of losses by the chemistry.

4 Accelerator Mass Spectrometry (AMS)

In this chapter, the ultra-sensitive technique of Accelerator Mass Spectrometry (AMS) is described. First, basic principles of AMS are introduced with a comparison of different AMS approaches. After the introduction, which is based on [110], the following sections are dedicated to the different parts of the setup in Garching used for this project.

4.1 Basic Principles of AMS

AMS is an ultra-sensitive single-ion-counting technique to detect smallest concentrations of radionuclides. This approach is complementary to activity and decay counting experiments, since it opens the regime of longer half-lives, where the activity does not decrease significantly over months. Typical half-lives of AMS radionuclides are in the order of 10^3 yr $< T_{1/2} < 10^8$ yr. The decay of the radionuclide is therefore negligible for the time of the measurement.

Common AMS measurements yield the fraction of radionuclides in the sample compared to its stable isotope(s), where the term "sample" refers to the material in the ion-source to be analyzed by the measurement. This makes AMS challenging, since the amount of the Isotope of Interest (IoI) in the sample is orders of magnitude smaller than the background, which are the stable isotopes and isobars of the IoI. "Common AMS measurements" means for all radionuclides having stable isotopes. Heavy isotopes like actinides or special cases like Tc do not have stable isotopes. Therefore, the measurement yields the amount of atoms of the IoI in the sample, either by comparison with a known number of atoms from an added spike in the sample itself, or by relating the number of atoms to a standard sample and normalization to a macroscopic current of another element.
The sensitivity of the measurement is given as the minimum concentration of the IoI needed to be detectable. Sensitivities for AMS measurements can go down to $N_{IoI}/N_{stable} \leq 10^{-16}$, where N is the number of atoms in the sample. To suppress the dominating, by orders of magnitude higher background, methods of experimental nuclear physics and sample preparation chemistry are applied. High energy beams, delivered by tandem accelerators, selective ion-sources, magnetic and electrostatic analyzers and detector systems are used to suppress almost all background and make single ions detectable. The most common ion-sources are Cs-sputter ion-sources, which yield negative ions. These ions are accelerated by electrostatic accelerators with terminal voltages between 200 kV for small table-top machines and 14 MV for the largest electrostatic tandem accelerators available at this time. The high-voltage terminal features a stripper foil or a gas stripper that destroys any molecules by electron stripping. To analyze the high energy beam

and to separate the isotopes, one uses electrostatic and magnetic analyzers like dipole magnets, electrostatic deflectors or Wien velocity filters. In the end, the IoI and the remaining background is analyzed in a particle detector system which consists of a combination of velocity, energy loss and total energy measurements. Standard tools from experimental nuclear physics are ionization chambers, passive absorbers, semiconductor detectors and Time-of-Flight (ToF) paths. The sample is treated by tailored purification chemistry to suppress other elements, especially isobars. The usage of ion-exchange chromatography has proven to be successful in many cases.
The most common application of AMS is radiocarbon-dating, the so-called ^{14}C-method. Historically, this was the trigger for the development of AMS and only possible because of its simplicity [82]. ^{14}C belongs to the group of light elements. Due to that, the relative mass difference ΔM between the IoI and the stable isotopes is relatively large (see equation 4.1).

$$\Delta \mathrm{M} = \frac{|\Delta m|}{m_{stable}} = \frac{|m_{IoI} - m_{stable}|}{m_{stable}} \tag{4.1}$$

This leads to good separation of isotopes by the different filter elements in the beamline. Despite the fact, that there is the very abundant isobar ^{14}N, the suppression of it is simple. Since N does not form negative ions in the ion-source, it is completely suppressed even before entering the accelerator. These two advantages made ^{14}C measurements feasible in the early days of AMS in the 1970s [8, 83].
Nevertheless, developments in this field allow us to measure more than 30 different AMS isotopes at this time (see Figure 4.1). Unique detection possibilities and isotopes for different applications in science make AMS to a relevant tool of interdisciplinary research. Applications range from basic research like nuclear astrophysics for nucleosynthesis or cross section measurements over geo-sciences like trace analysis of soils, ice/snow and meteorites to nuclear waste management or reactor applications [35].

The "standard" procedure of an AMS measurement is the following:
The sample material is pressed into a sample holder after chemical purification. Then, all sample holders are mounted in the ion-source, where the extraction takes place. If the ion-source has only one plug-in position, so called "single-cathode" ion-sources, the sample holder has to be removed before a new holder can be inserted. All magnets, electrostatic analyzers, Wien filters and the terminal voltage of the tandem are optimized to get the highest beam current to a Faraday cup near the detection system.
After having stable conditions, a standard sample is inserted. Standard samples have a known concentration of the IoI and with these, it is possible to deduce the unknown detection efficiency from the last Faraday cup in front of the detector to the detector after software cuts. By knowing this efficiency, one determines the blank level in a blank run. This blank level prescribes the sensitivity for the following measurements of all samples. Between sample measurements, one has to stop and monitor the beam current and the efficiency to correct for drifts in the system. This sandwich system reduces systematic errors in the later analysis.

To determine the concentration of the IoI in the sample, one has to calculate the detection efficiency ϵ from the last Faraday cup to the detector after software cuts. The following equations contain expressions for the IoI ^{60}Fe:

$$\epsilon = \frac{n_{std}}{c_{std} \cdot Q_{std,Fe}} \frac{1}{f_{std,life}} \tag{4.2}$$

where n_{std} is the detected number of ^{60}Fe events from the standard run after data analysis, c_{std} is the known concentration of ^{60}Fe in the standard material, $Q_{std,Fe}$ is the total charge delivered by stable Fe at the Faraday cup in front of the detection system and $f_{std,life}$ is the fraction of lifetime of the detector to total measurement time, to compensate for dead-time errors.
The total charge is determined by:

$$Q_{std,stable} = I_{Fe} \cdot t = \frac{I_{^{54}Fe} \cdot t}{q_{^{54}Fe} \cdot f_{^{54}Fe} \cdot e} \tag{4.3}$$

with $f_{^{54}Fe}$ the isotopic fraction of the measured ^{54}Fe to stable Fe, $q_{^{54}Fe}$ the charge state of ^{54}Fe, $I_{^{54}Fe}$ the measured electrical current on the Faraday cup, I_{Fe} the calculated particle current of stable Fe on the Faraday cup, e the elementary charge and t the measurement time.
The detection efficiency corresponds to the physical transmission through the detection system including losses by software cuts to discriminate between the IoI and any background.
The concentration of the IoI in a sample, here ^{60}Fe, is calculated by:

$$c_{^{60}Fe} = \frac{N_{^{60}Fe}}{N_{Fe}} = \frac{n_{^{60}Fe}}{\epsilon \cdot Q_{s,Fe}} \cdot \frac{1}{f_{s,live}} \tag{4.4}$$

where $n_{^{60}Fe}$ is the detected number of ^{60}Fe events in the sample after data analysis, $Q_{s,Fe}$ is again the total charge delivered by stable Fe and $f_{s,life}$ the fraction of lifetime of the detector, but now for the measurement of the sample.
After inserting the equation for the detection efficiency ϵ, the equation for the concentration reduces to:

$$c_{^{60}Fe} = c_{std} \frac{n_{^{60}Fe}}{n_{std}} \cdot \frac{Q_{std}}{Q_{^{60}Fe}} \cdot \frac{f_{std,live}}{f_{s,live}} \tag{4.5}$$

After all, only ratios of critical quantities have to be taken into account. Critical quantities are the concentrations of the standard and the sample, the beam currents, the measurement times after dead-time correction and the number of detected events in the detector.

As described above, this normalization is not possible for special cases like ^{99}Tc, where no stable isotope as reference exists. To relate the detected events in the detector to a concentration in the sample, typically another element is used for normalization. This element should have almost the same mass, nuclear charge and behavior in the ion-source as the IoI, otherwise large systematic uncertainties have to be considered during the normalization e.g. due to matrix effects in the ion-source. Another approach is to use a different, but also long-lived radioisotope of the IoI as a spike. This approach is then comparable to the "common" AMS measurement, if the radioisotope is available in macroscopic quantities. Otherwise, one has to measure both radioisotopes in an AMS measurement, which is more challenging.

After this short introduction to the basic principles of AMS, the unique setup at the Maier-Leibnitz-Laboratory in Garching will be described in detail with special focus on the particular components of the ion-sources, the accelerator and the detectors.

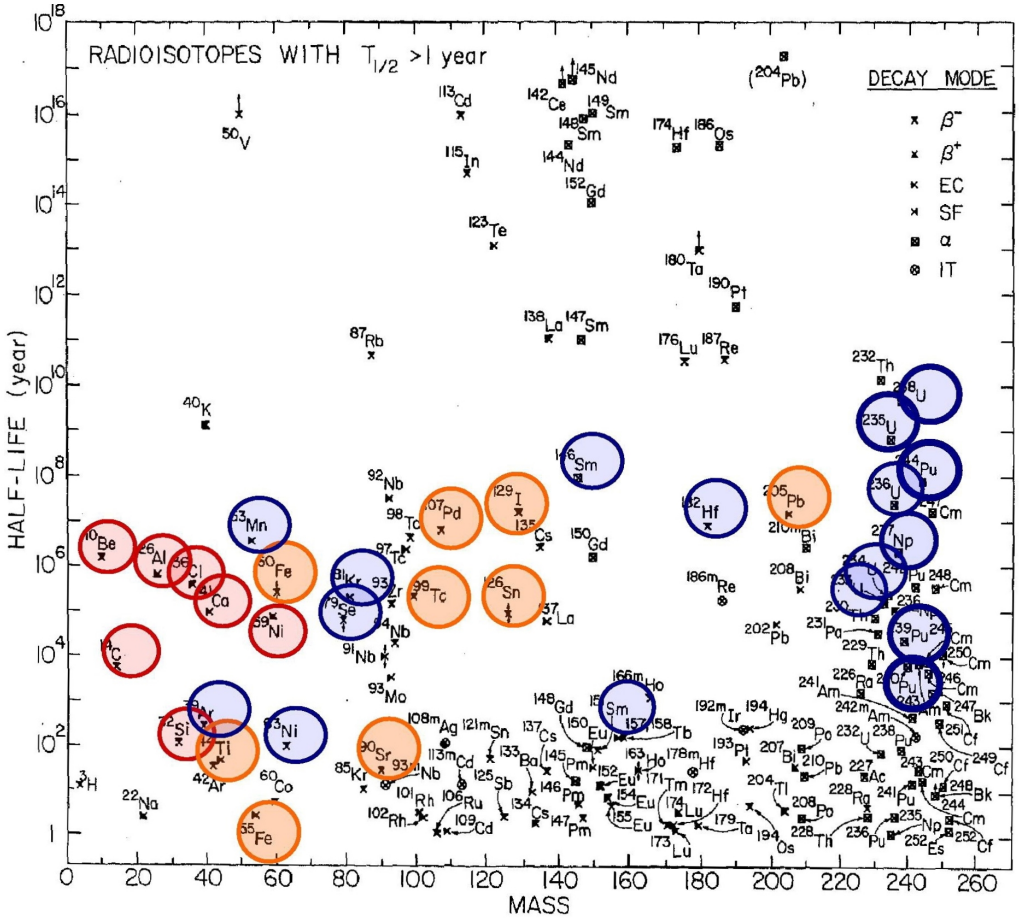

Figure 4.1: Collection of long-lived radioisotopes, sorted by their mass and half-life. Circles from red over orange to blue indicate isotopes used for AMS from 1981 over 1996 to 2008 as reported in the International AMS Conferences. Picture taken from [35].

4.2 AMS-Setup at the MLL

The AMS setup in Garching features two dedicated beamlines. One beamline consists of a ToF path and a Passivated Implanted Planar Silicon (PIPS) detector from Canberra, which is currently replaced by a PIPS detector array for higher detection efficiency [62]. This setup is typically used for AMS of actinides, where no stable isobar exists, and which are too heavy for a magnetic detection system. For special heavy isotopes like ^{79}Se, ^{93}Zr or ^{99}Tc with stable isobars ^{79}Br, ^{93}Nb and ^{99}Ru, respectively, the beamline features removable silicon nitride foils as passive absorber to change the ToF of the IoI and its isobar by different energy loss behavior during the transmission through the passive absorber foils. Such isotopes can be measured either by this setup or the GAMS setup [49]. The GAMS (Gas-filled Analyzing Magnet System) is used for cases, where stable isobars interfere in the mass region $30 < A < 140$. Lighter isotopes are typically measured at smaller facilities, heavier isotopes require techniques as described above. For this project, the IoI is ^{60}Fe with its stable isobar ^{60}Ni and the measurements are performed with the GAMS setup.

Figure 4.2 gives an overview of the experimental setup used for AMS in Garching. AMS isotopes, most commonly measured in Garching, are ^{36}Cl, ^{41}Ca, ^{53}Mn, ^{60}Fe, ^{79}Se, ^{93}Zr, ^{97}Tc, ^{99}Tc, ^{238}U, ^{244}Pu and superheavy elements.
In the following, the different parts of the beamline from the ion-source to the GAMS are described in detail with focus on the crucial elements for AMS.

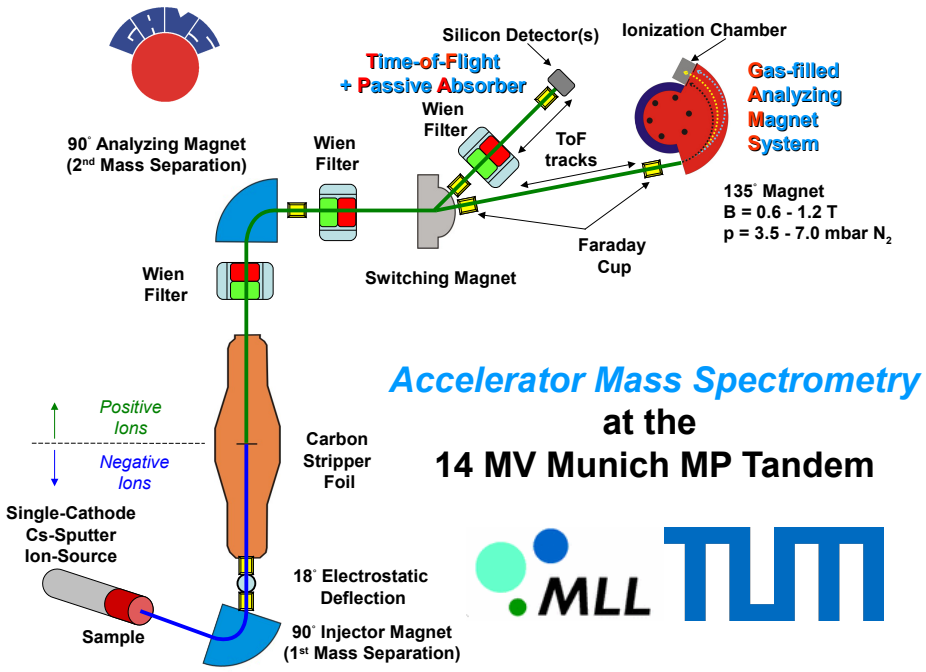

Figure 4.2: Overview of the experimental setup in Garching. The setup with the Gas-filled Analyzing Magnet System (GAMS) is used for this project.

4.2.1 From the Ion-Source to the Tandem Accelerator

In the previous chapter, the sample production procedure was described. The produced samples are then mounted in the ion-source. For this project, a modified Middleton-type single-cathode Cs-sputter ion-source is used [79]. The cathode is screwed onto a water-cooled rod and placed concentrically near the ionizer. Warm Cs vapor is ionized on a red-hot, spherical Ta ionizer and positive Cs ions are accelerated towards the sample holder, where they sputter molecules and atoms out of the sample. Ssee Figure 4.4 for details about the ion-source used in this project. Most of sputtered material is electrically neutral, whereas some fraction forms negative ions by electron exchange with Cs that has condensed onto the cold sample holder. The negative ions are then accelerated towards the exit of the ion-source. Applied voltages are 5 kV for the sputtering process and 23 kV for the extraction. Neutral or positively charged atoms and molecules stay in the ion source or in the cathode. This material could be sputtered again, which leads to a minor form of recycling. See Figure 4.3 for a technical drawing of the ion-source with its components.

Single-cathode ion-sources are chosen instead of multi-cathode ion-sources for AMS at the MLL because of their advantages needed for this setup.
The most important advantage is the low risk of cross-contamination [62]. Only one sample is mounted at the time, whereas between 40 and 200 samples are mounted in a multi-cathode wheel. This reduces the risk of cross-talk between standard samples and blanks. Our single-cathode ion-sources are exchanged and cleaned after each beamtime, which reduces any contamination further. Observed cross-contamination is at least four orders of magnitude below the concentration of the standard sample for ^{36}Cl and even lower for ^{60}Fe or ^{99}Tc and could be obliterated by cleaning.
Another advantage is the cooling system. Samples with low thermal conductivity are cooled efficiently to ensure that Cs vapor condenses onto the sample holder. Multi-cathode wheels are often only slightly cooled or non-cooled, which causes problems with specific insulating samples. The only disadvantage is that one has to stop the measurement and remove the sample by hand to insert another sample. This is time-consuming and can cause drifts in the system. Careful monitoring of all components avoids losses in transmission or efficiency. Since this setup is designed to measure lowest concentrations with highest sensitivity and the number of samples is not as high as in other facilities, single-cathode ion-sources are chosen as suitable ion-sources.

After the extraction took place, the negatively charged ions pass through a system of electrostatic lenses and enter a 90° dipole bending magnet, the injector magnet. The maximal field strength is 1.2 T with a bending radius of 0.38 m. Ions of chemically different atoms or molecules have the same energy, but according to their different mass, they have different momenta. Thus a first mass selection on the Low-Energy side (LE) is possible (see equation 4.10). The mass resolution of the magnet is obtained by:

$$\frac{\Delta m}{m} = 2 \cdot \frac{\Delta B}{B} \tag{4.6}$$

where ΔB is determined by the FWHM of the beam current on the Faraday cup and the change of the magnetic field needed. The mass resolution on the second cup after the magnet (C1) is higher than for the first cup (AMS-Cup) because of several optical elements in between.

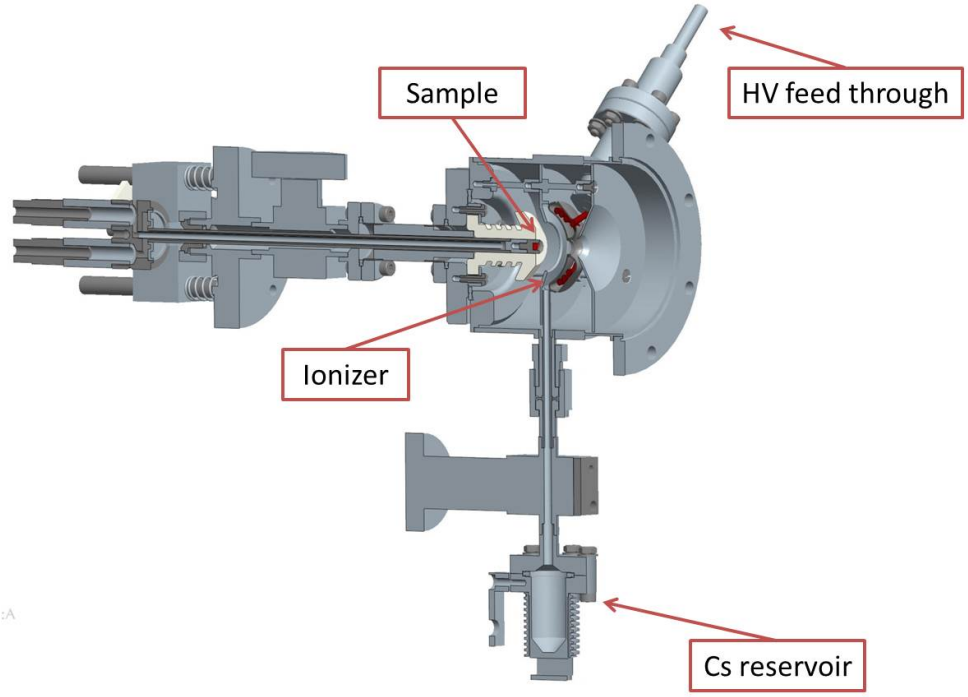

Figure 4.3: Cross section through the Cs-sputter ion-source used for this project. The cooled sample is located near the hot ionizer. Ions are extracted by the applied voltages.

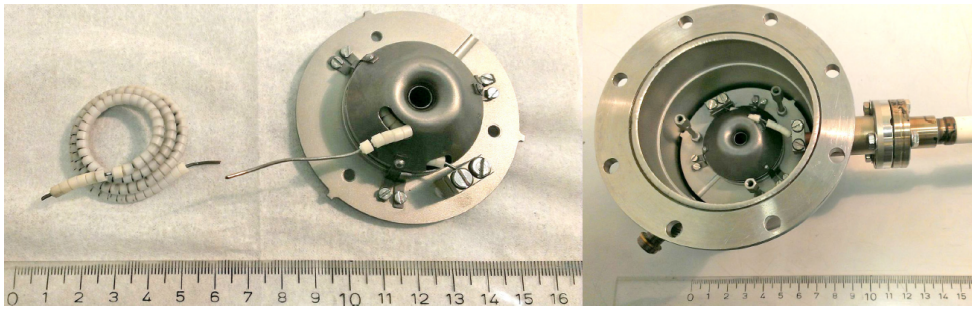

Figure 4.4: Opened Cs-sputter ion-source. Left: Heating wire of the ionizer with pearls for isolation. Middle: Ta ionizer with opening for beam extraction. Right: Ionizer mounted in ion-source.

Typical values for mass resolutions are 1:50 - 1:80 at the AMS-Cup and 1:300 - 1:400 at C1, depending on the beam-tuning and the apertures used after the magnet. For this project, the determined mass resolution for $^{54}Fe^{16}O^-$ is:

$$\left(\frac{\Delta m}{m}\right)_{AMS} \approx \frac{1}{65} \quad \text{and} \quad \left(\frac{\Delta m}{m}\right)_{C1} \approx \frac{1}{355} \tag{4.7}$$

The selected beam is transported through electrostatic lenses, steerers and an electrostatic 18°-deflector to the entrance of the tandem. The beam current is monitored after the injector magnet and in front of the tandem by Faraday cups (AMS-Cup and C1 as introduced above).
In addition to the already mentioned components in the beamline, three four-sector apertures are installed at critical points in the beamline. These can be used to determine the offset of the beam from the center and to reduce beam currents to avoid deterioration of the foils in the tandem from high beam currents. Furthermore, these apertures can be used to reduce the amount of interfering isotopes with different mass in the actual beam. These isotopes have slightly different trajectories than the main beam and can therefore be cut by narrow apertures.

The extracted beam is pre-accelerated by an applied pre-acceleration voltage of 150 kV before entering the tandem. The total kinetic energy of the ions on the LE side is:

$$E_{tot,LE} = e \cdot (U_{sputter} + U_{extraction} + U_{preacceleration}) \tag{4.8}$$

The total kinetic energy of all negatively charged atoms or molecules is therefore 178 keV.
The extraction voltage and the sputter voltage in combination with the maximum magnetic field of the injector magnet allow injection of atoms or molecules up to mass m = 300. For higher masses the voltages are reduced and therefore the energy of the ions. Any reduction of these voltages reduces the resolution of the system, but enables injection of highest masses.

In some cases, the IoI could not be used to tune the beam at the LE side of the tandem because of interferences from other stable compounds. Fe is a typical example, where $^{54}Fe^{16}O^-$ is overlayed by an interfering molecule with almost equal magnetic rigidity at the AMS-Cup, whereas these two species are separated on C1 because of higher separation capability. Therefore, the more abundant $^{56}Fe^{16}O^-$ is chosen to tune the beam at the LE side and it is later switched back to $^{54}Fe^{16}O^-$. This is possible, because the low energy tuning, except for the injector magnet, is only sensitive on the constant energy over charge ratio.
The finding of a second species is possible by the relative width of the FeO^- peak relative to a neighboring peak in this region. In principle, the $^{54}Fe^{16}O^-$ peak has to have the same width as the $^{56}Fe^{16}O^-$ peak. A second species overlays the Gaussian of $^{54}Fe^{16}O^-$ with another Gaussian, resulting in a broader Gaussian than before. Therefore, $^{56}Fe^{16}O^-$ is used to tune the beam at the LE side and $^{54}Fe^{16}O^-$ is used for further beam tuning.

4.2.2 From the Tandem Accelerator to the GAMS

The tandem accelerator is a 14 MV electrostatic pelletron van de Graaff accelerator, installed in the 1970's. The tank of the tandem is filled with 7 bar of SF_6 as insulating gas. Single charged ions and molecules are accelerated towards the terminal, where they pass through a thin C stripper foil ($4\,\mu m/cm^2$). Foil stripping is chosen over gas stripping because of higher yields for higher charge states. The stripping process removes several electrons from the molecules and ions. Molecular bonds break up, leading to the so-called Coulomb-explosion, which occurs for positively charged molecules. Molecular background, which contributes to isobaric background, is the most dominant problem for conventional mass spectrometry to reach higher sensitivities. Molecular background can also be misinterpreted and lead to errors during data analysis. AMS is free from molecular background by the stripping process.

Stripped and now positively charged ions are accelerated with the same voltage towards the exit of the tandem. The total energy of the ions after the tandem is:

$$E_{tot,HE} = E_{tot,LE} \cdot \frac{m_+}{m_-} + e \cdot \frac{m_+}{m_-} \cdot U_{terminal} + q \cdot U_{terminal} \tag{4.9}$$

where m_- is the mass of the negatively charged ion before stripping and m_+ is the mass of the resulting positively charged ion after stripping. m_- is unequal to m_+ for the case of injected molecules. Typical energies used for AMS are 100 MeV up to 150 MeV, which corresponds to 1 MeV - 4 MeV per nucleon. The high voltage stability of $\Delta U_{terminal} = 3$ kV results in a relative voltage and energy stability of $\Delta U : U \approx 1 : 3500$ that is crucial for the stability of the measurement conditions. The voltage is stabilized by a slit system after the tandem, which is only possible for a macroscopic beam. For the case of AMS, a generating voltmeter (GVM) is used to stabilize the voltage to a previously, by slits determined value. The stability of the GVM is comparable to the slit system.

After exiting the tandem, the magnetic rigidity of the beam $B\rho$ (equation 4.10) is determined and kept fixed by a strong dipole magnet. This 90° analyzing magnet has a maximum field strength of 1.6 T and a bending radius of 1.65 m. Its mass resolution is approximately 1 : 3000.

$$B\rho = \frac{p}{q} = \frac{mv}{q} = \frac{\sqrt{2mE}}{q} \approx \left(\frac{2mU}{q}\right)^{1/2} \tag{4.10}$$

To change between different isotopes and to keep the magnetic rigidity fixed, the energy of the particles and therefore the terminal voltage has to be changed. The magnetic rigidity is fixed, because all focusing elements at the HE side are magnetic elements.
For further suppression of interfering isotopes, two Wien filters are installed before and after the analyzing magnet. The first Wien filter has a mass resolution of $\Delta m : m \approx 1 : 80$ and the second (optional) has a mass resolution of $\Delta m : m \approx 1 : 40$. Here, the magnetic field is kept fixed and the electrostatic field is varied for a change in isotopes. For an overview of the tandem hall, see Figure 4.5. After passing the analyzing magnet, the beam is directed towards the GAMS beamline by a switching magnet. In this beamline an optional ToF setup is installed with a path length of 3.4 m. The ToF is not used for isotopes, where the relative mass difference between the IoI and its stable isotopes is large (see equation 4.1).

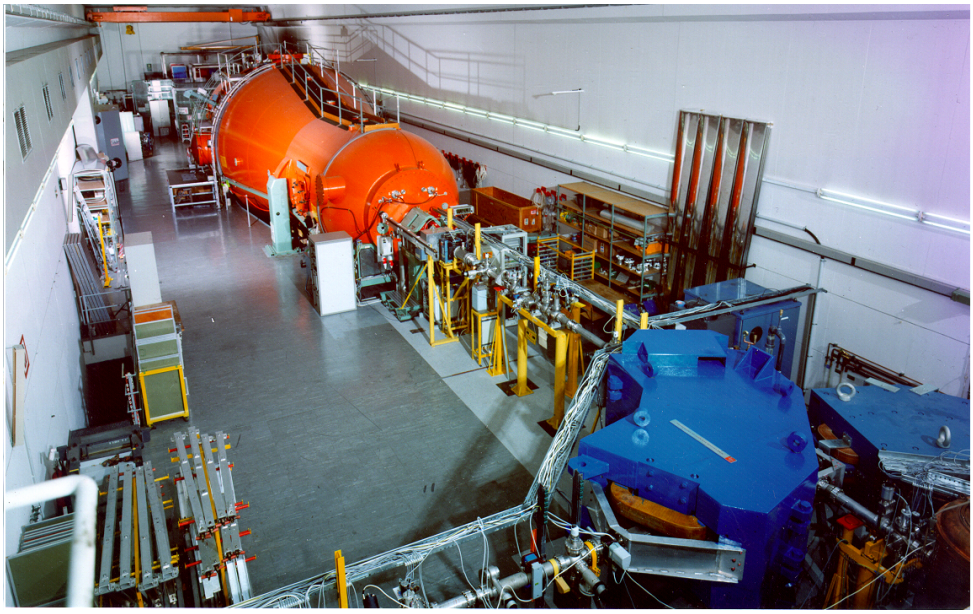

Figure 4.5: Accelerator hall with the tandem (orange) and the analyzing magnet (blue).

Up to this point, no isobaric suppression is achieved. Isotopes are separated by slits and the devices described before. Isobars instead exist in the same charge state and have the same mass, therefore the same magnetic rigidity and energy as the IoI.

The GAMS consists of a magnet chamber with maximal field strength of 1.2 T and a bending radius of 0.9 m at an angle of 135° (see Figure 4.6). As the name says, the magnet chamber is filled with 3 mbar - 7 mbar of N_2-gas. The entrance window of the GAMS is a thin Mylar foil (0.9 μm) to separate the evacuated beamline from the gas-filled chamber. By collisions with N_2-gas molecules, the ions lose energy and an average charge state distribution is formed which is different for the IoI and its isobar [99, 11]. This difference in charge leads to a difference in magnetic rigidity (see equation 4.11).

$$\bar{q} \propto v \cdot Z^{0.4} \longrightarrow B\rho \propto \frac{m}{Z^{0.4}} \tag{4.11}$$

The IoI and its isobar follow different trajectories and enter with spatial separation the detector chamber. The end of the gas-filled magnet features an aperture in front of the detector. By varying the magnetic field in such a manner that the maximum of the isobaric beam is stopped by the aperture, the isobar could be suppressed by three to five orders of magnitude.

The detector consists of an ionization chamber with a 5-fold split anode and a Frisch grid (see Figure 4.7). The Frisch grid collects the mirror charges from all anodes, which is proportional to the total energy loss of the particles. The differential energy loss is measured in each anode, where the first two anodes are split diagonally in order to reconstruct the horizontal position and the entrance angle of the particle. The ionization chamber is filled with 30 mbar - 60 mbar isobutane (C_4H_{10}). The IoI and residual background are stopped at different depth because of their different stopping power due to their different nuclear charges.

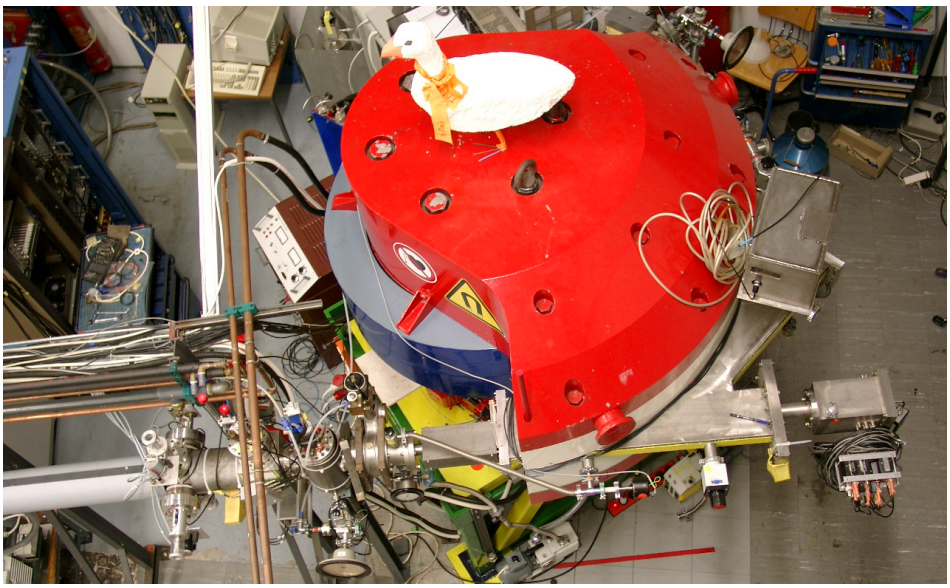

Figure 4.6: Top view: Gas-filled Analyzing Magnet System. The beam enters the gas-filled magnet from left to right and is deflected by 135°.

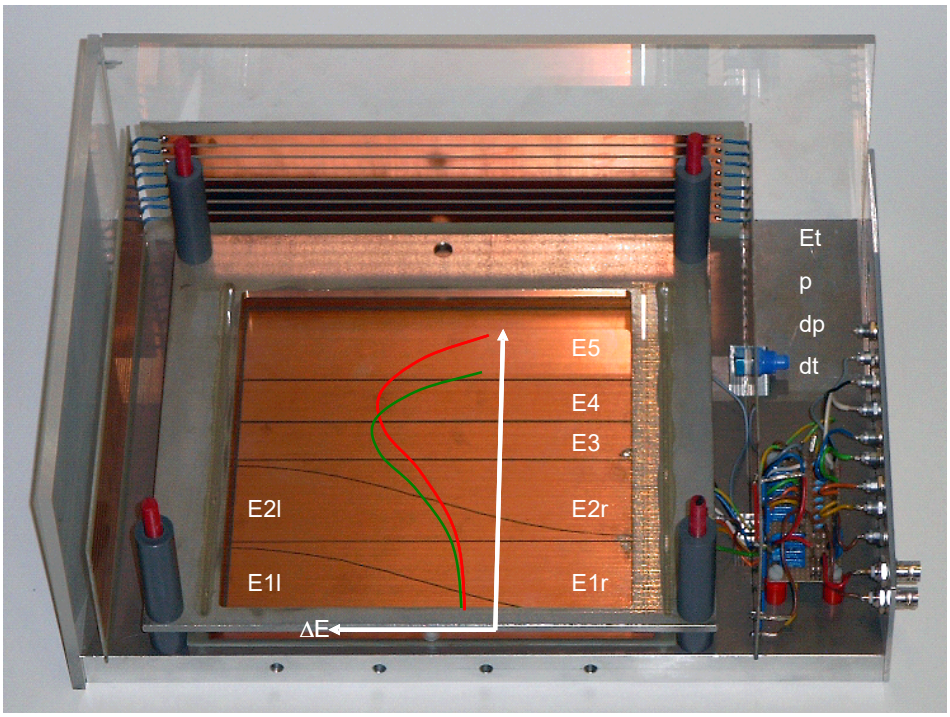

Figure 4.7: Ionization chamber with a 5-fold split anode and a Frisch grid. Readout channels and a schematic drawing for the energy loss behavior of different species are added to the picture. The species denoted in green has higher Z than the species in red.

4.3 AMS of ^{60}Fe at the MLL

^{60}Fe is a special AMS isotope for the setup in Garching. The whole setup was optimized in the past to measure nuclides in this mass region and the sensitivity achieved for ^{60}Fe is the highest of all isotopes in Munich.

For the measurement of ^{60}Fe concentrations, samples are chemically prepared as Fe_2O_3. Typically, 5 mg of Fe_2O_3 is mixed with 10 mg of high purity silver powder, because Ag increases the heat conductivity of the sample. This dedicated Ag powder introduces no additional background, because it is relatively clean in Ni, and Ag is heavier than Fe which makes a full separation at the injector magnet possible. Again for the same reason, the samples are pressed into a manufactured high-purity silver cathode with 1.6 mm sample diameter and 2 mm sample depth. This small size of the cathode leads to smaller beam spots, higher separation capability of optical elements and fewer losses because of smaller emittance of the beam.

FeO^- yields the highest currents of all Fe compositions used in this ion-source. Therefore, ^{60}Fe is extracted in the form of $^{60}Fe^{16}O^-$. As macroscopic beam, $^{54}Fe^{16}O^-$ is used. ^{54}Fe, with an isotopic fraction of 5.8% is in general better for beam tuning than the more abundant ^{56}Fe with 91.8%, because the current of $^{56}Fe^{16}O^-$ (several μA) is too high for continuous operation using foil stripping.
Extraction of FeO^- is unequivocal. The magnetic field of the injector is increased continuously starting from zero. The highest peak at the beginning is $^{16}O^-$. From this distinct point, the magnetic field for $^{54}Fe^{16}O^-$ is calculated by equation 4.12.

$$B_{^{54}Fe^{16}O^-} = B_{^{16}O^-} \cdot \sqrt{\frac{m_{^{54}Fe^{16}O^-}}{m_{^{16}O^-}}} \tag{4.12}$$

Furthermore, the $^{54}Fe^{16}O^-$ peak could be cross-checked by the neighboring $^{56}Fe^{16}O^-$ peak, which is the highest peak in this region, or by the two silver peaks from $^{107}Ag^-$ and $^{109}Ag^-$. Because of interferences for $^{54}Fe^{16}O^-$ at the AMS-Cup, $^{56}Fe^{16}O^-$ is used at first to tune the beam at the LE side before changing back to $^{54}Fe^{16}O^-$. For a mass spectrometric analysis of the cathodes used in this project, see Figure 4.8.

The ions are then injected into the tandem accelerator. The terminal voltage for ^{60}Fe is set at 11.5 MV. This terminal voltage is high enough to reach high charge states by foil stripping and high total energy of the beam, whereas sparks in the tandem are less frequent compared to higher voltages. For ^{60}Fe, the charge state 10+ and for ^{54}Fe, the charge state 9+ was chosen, instead of also common 11+ and 10+, respectively. $^{60}Fe^{10+}$ and $^{54}Fe^{9+}$ have the same m/q, leading to only small changes in the terminal voltage and to no change in the Wien filter (equation 4.10). In addition to that, the stripping yield is a factor of 2 higher for the lower charge states than for the higher states, which reduces the measurement time needed for a certain sensitivity and increases the total efficiency of the setup (see Table h). The drawback of this choice is the integer m/q = 6, leading to m/q interferences in the acquired data. For most cases, an integer m/q ratio is problematic because of high background rates. By using the gas-filled magnet, most background is already discarded. Identified background comes from Co, Se, Cu and of course Ni, whereby Cu is almost completely suppressed by using silver cathodes and powder.

Charge state	Energy [MeV]	Analyzing Magnet [Gauss]	Stripping Yield
5	66.6	1091.162	1.8%
6	78.1	984.699	5.5%
7	89.6	904.057	12.2%
8	101.1	840.307	19.7%
9	112.6	788.303	22.8%
10	124.1	744.848	19.1%
11	135.6	707.840	11.5%
12	147.1	675.834	5.0%
13	158.6	647.800	1.6%

Table h: Stripping yield for ^{60}Fe, injected as $^{60}FeO^-$, at a terminal voltage of 11.5 MV. Analyzing magnet field as well as stripping yield obtained by the calculation program beam32 at MLL are displayed. Charge state 10+ is chosen because of the combination of high yield and high energy.

Finally, $^{60}Fe^{10+}$ is detected in the ionization chamber situated behind the GAMS. Up to this point, $^{60}Ni^{10+}$, which is stable and therefore many orders of magnitude more abundant than $^{60}Fe^{10+}$, is only suppressed by dedicated chemistry and by extraction as $^{60}Ni^{16}O^-$ (one order of magnitude less sufficient compared to $^{60}Fe^{16}O^-$). This reduction of ^{60}Ni is not sufficient to measure ^{60}Fe because of a too high ^{60}Ni rate in the ionization chamber causing significant dead-times of the detector and too high background.
The gas-filled magnet leads to a spatial and energetic separation of ^{60}Ni and ^{60}Fe. Due to this effect, the magnetic field of the GAMS could be adjusted in such a way that ^{60}Ni is shifted spatially to the inner side of the magnet chamber and stopped by an aperture. ^{60}Fe at the same time is more rigid and reaches the detector. This change in magnetic rigidity, in combination with the adjustment of the magnetic field, reduces the ^{60}Ni background by 4 to 5 orders of magnitude. The residual ^{60}Ni and ^{60}Fe, at low enough rate for measurements, enter the ionization chamber. The gas pressures are adjusted in such a way that the charge state averaging and the energy straggling is optimized, which is roughly the case for ions losing half of their energy in the GAMS and half of their energy in the ionization chamber.

In the ionization chamber, ^{60}Ni and ^{60}Fe lose energy according to their characteristic Bragg curve. ^{60}Ni with higher nuclear charge Z is stopped before ^{60}Fe. The chosen gas pressure for the given energy of ^{60}Fe and ^{60}Ni is 3.5 mbar for the GAMS chamber and 40 mbar for the ionization chamber. ^{60}Ni could be suppressed by 6 orders of magnitude during data analysis. See Figure 4.9 for a simulation of the energy loss in the GAMS and in the ionization chamber for ^{60}Fe and ^{60}Ni.

By stopping the ions completely in the ionization chamber, one induces false positive signals on the following anodes. This problem is solved by a linear gate and stretcher. For this project, ^{60}Fe and ^{60}Ni are not stopped completely, which does not affect the separation capability because of high separation in all signals.

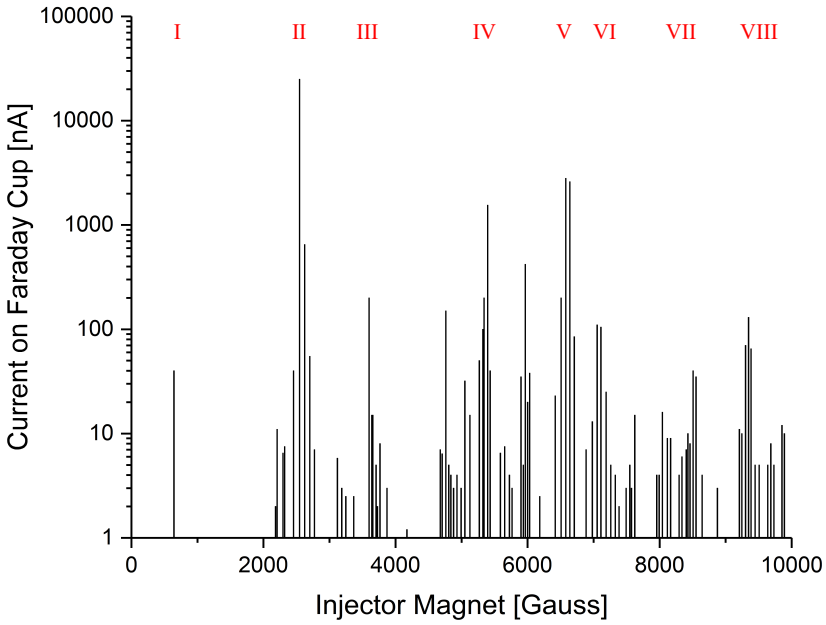

Figure 4.8: Mass spectrometry at the injector magnet for moderate ion-source output. Currents above 1 nA are displayed. Labels I-VIII and the most prominent lines are explained in Table n. The highest peaks are $^{16}O^-$, $^{56}Fe^{16}O^-$ and $^{107/109}Ag^-$.

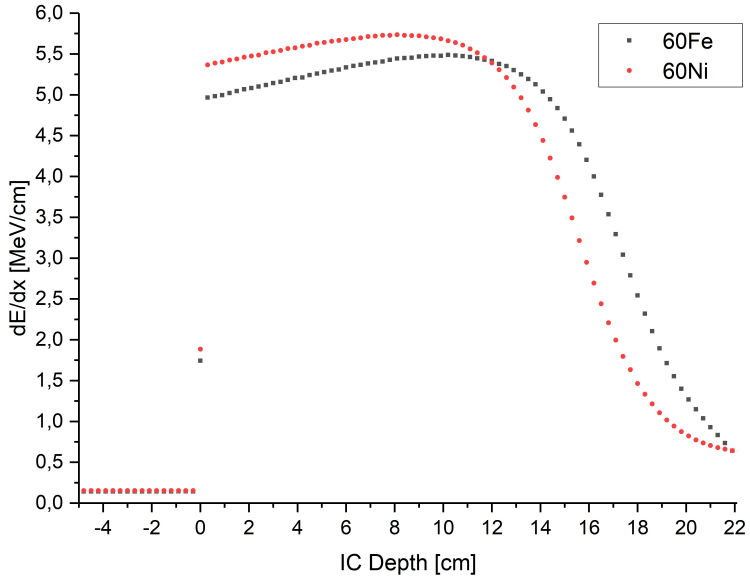

Figure 4.9: Energy loss calculation with TRIM for ^{60}Fe and ^{60}Ni in the GAMS and ionization chamber at 125 MeV for 40 mbar of isobutane [122]. The ions lose considerably less energy per unit length in the GAMS chamber, but the integrated energy loss in the GAMS is comparable to the ionization chamber.

4.4 Data Acquisition and Analysis

^{60}Fe and ^{60}Ni lose energy in the ionization chamber and are thereby detected and discriminated. The ionization chamber produces in total eight raw signals, five from the energy loss anodes (E1 - E5), where the first two anodes produce two signals because of diagonal splitting, and one additional signal from the Frisch grid (Et). In addition to the energy signals, two positions in x-direction are determined by the split anodes (p). The x-angle is determined by the change in x-position (dp) and the y-angle indirectly by the difference in drift times between the first anode and the third anode (dt).

Furthermore to account for high count rates, a pile-up rejection is installed that checks if a signal is followed, within a given gate, by another signal. If this is the case, the distorted signal is recorded with a finite pile-up signal that could be discarded during data analysis. Pile-up, as well as detector dead-time, becomes significant for high count rates above 1000 events/s. The gas-filled magnet with the aperture in front of the ionization chamber is a powerful tool to suppress high count rates, which are purely caused by background.
Besides these standard signals, an optional ToF signal is produced by two Micro-Channel-Plates (MCP's), if inserted. The MCP's detect the electrons that are liberated by the ions, when transversing a thin C foil. MCP's function as start and stop detectors to get a time signal that is directly related to the velocity of the ions. ToF could be used to discriminate between the IoI and its stable isotopes, whereas the isobar has the same ToF as the IoI. As stated before, ToF is not needed for ^{60}Fe measurements, because the next stable isotope of ^{60}Fe, which is two masses apart, is already suppressed by the optical elements in the beamline. For a more detailed description of the electronics, see [70].

For data analysis, each signal of an event is digitized and stored in its raw form with a time stamp to allow on- and off-line analysis. Raw data are displayed as 1-D histograms and are combined in 2-D histograms to give energy and angles correlated with the horizontal position of the detected particle. 1-D histograms display the number of events vs. the assigned channel for the signal. 2-D histograms show channel of energy vs. channel of position of the particle and the number of detected events is color coded. Note, channel numbers are not calibrated. The used software packages for data analysis are ROOT [22] and in-house developed MARaBOU [73]. Histograms are displayed by HistPresent which is also used for later analysis of the data.

In the course of this project, a new background suppression technique at the data acquisition level was installed. For cases with ${}^{A}_{Z}$X as IoI and ${}^{A}_{Z'}$Y for its isobar, where Z' $>$ Z, the isobar is stopped in the ionization chamber before the IoI is stopped. This could be used to suppress the isobar by a Linear Gate and Stretcher (LGS), where inverted bipolar signals could be discarded. For details about the LGS and first measurements with Fe and Ni, see Appendix D.

Data analysis is conducted in the following way. At first, a standard run with clearly visible and distinguishable ^{60}Fe events is compared to a blank run with no ^{60}Fe events at all. By this, it is possible to identify ^{60}Fe in the 2-D spectra by its (x,y) location in the histogram. In the case of ^{60}Fe, the best histogram to start with is (p, E4). After identification, the bulk of background is discarded by window conditions in p and E4. This reduction of background leads to a higher amount of true ^{60}Fe events than background events in the standard run. Therefore, 1-D signals

could be used to set window conditions on each signal to reduce background further and keep as much as possible of the ^{60}Fe events. The efficiency of detection depends mostly on these cuts and determines directly the time needed to achieve a certain sensitivity. Detection efficiencies can range from more than 90% for well separated species (e.g. ^{36}Cl and ^{36}S) to a few percent for little separation (e.g. ^{99}Tc and ^{99}Ru), depending on the software cuts applied.

In the end, the blank measurement with window conditions should be free of events. This approach is used because of the following reasons: Blank runs should per definition contain no ^{60}Fe events. Therefore, the number of events in the blank run should be zero. If there are any events left in this run, then they are purely background. Hence, in all other samples this amount of background has to be subtracted.
The number of events to keep in the blank run is arbitrary. However, this number influences the efficiency, the statistical fluctuation in events and the sensitivity of the measurement.
Subtraction of background events could be an issue of discussions, whether residual events after subtraction are real events or a fluctuation in background. For cases with background events in the blank measurements, a detailed background correction has to be applied, including precise knowledge about the background, statistical subtraction of background and detailed uncertainty analysis to distinguish between fluctuations in background and real events. This is not needed in this project because of excellent separation of ^{60}Fe from background and therefore having background-free conditions after software cuts.
One has to mention that this is only valid for cases like ^{60}Fe or ^{36}Cl, where separation of background from the IoI is sufficient. For more demanding isotopes like ^{93}Zr or ^{99}Tc, the overall aim is to reduce the amount of background to the extent that the efficiency is still high, but the statistical fluctuation in the background which is directly correlated to the total amount of background in the measurement, is reduced. In the end, the measured number of events has to be significantly higher than the fluctuation in background.
In general it is crucial that the total amount of background, as well as the type of background in the blank run, is comparable to the background in the sample run to get reliable outcomes. The amount of background, which is zero for the blank measurement is statistically estimated to be 1.29 events as proposed by Feldman and Cousins [32].

In addition to the previously explained data analysis tool, there are two other ways to analyze the data.
On the one hand, 2-D window conditions could be used to analyze the data. 2-D windows are convenient for the last steps of data analysis. After the number of background events decreased significantly and the residual events are hard to discriminate in 1-D histograms, it is more convenient to switch to 2-D histograms to discard the remaining background events.
On the other hand, the multi-dimensional problem of data analysis of several signals could be tackled by a χ^2-analysis. χ^2-analysis determines the deviation of each parameter of an event from the expected mean in terms of standard deviations of the ^{60}Fe event distribution, which is assumed to be Gaussian (equation 4.13). By summation, the multi-dimensional problem is reduced to one dimension.

$$\chi^2 = \sum_{n=0}^{N} \left(\frac{E_n - \mu_n}{\sigma_n} \right)^2 \tag{4.13}$$

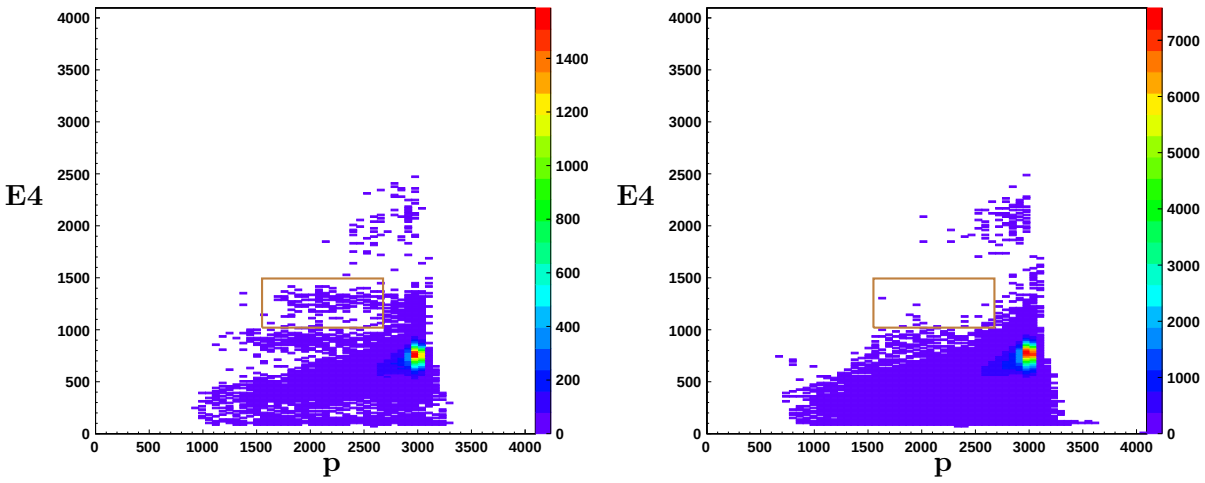

Figure 4.10: Window condition in brown for standard (left) and blank (right) measurements. Most of the background is discarded. The window condition is displayed in brown. Residual events in the region of interest could be separated by 1-D window conditions.

E_n are the measured signals for all acquired signal channels, μ_n are the means of the ^{60}Fe distributions for all acquired parameters and σ_n are the standard deviations of the ^{60}Fe distributions for all acquired signal channels.
This tool could be used in cases, where the dominant background is different in the signals compared to the IoI, and the amount of standard events is high enough to fit the distribution with a Gaussian. For this project, χ^2-analysis is only used to cross-check the analysis of 1-D window-conditions, whereas it is solely used for isotopes like ^{36}Cl and not applicable at all for isotopes like ^{93}Zr or ^{99}Tc.

Uncertainty analysis is a crucial part of data evaluation. Most uncertainties cancel by using standard material and the measurement of ratios. Uncertainties that appear throughout the evaluation are statistical current uncertainties by read off on analog instruments, statistical uncertainty of low count rates, statistical uncertainty by averaging over several standard runs and systematic concentration uncertainties of the standard samples as well as the uncertainty of the initial Fe content of the samples.

The most dominant uncertainty contribution comes from low counting statistics. If the number of events in a measurement run is $n > 20$, $\sqrt{n}$ is assumed as statistical uncertainty. If the number of events in a measurement run is $n < 20$, the confidence intervals of Feldmann and Cousins [32] are used to estimate the uncertainty.
The uncertainty by current read off during the sample measurement is estimated as pure statistical uncertainty to be 10% because of stable ion source output over the measurement time and high current stability at the Faraday cup. Therefore, the uncertainty for two measurements (before and after the data acquisition run) is 7%.
Statistical uncertainty by fluctuations in the ^{60}Fe count rate in the standard measurements and uncertainty by current read off for each standard measurement, has to be considered. In this case, the uncertainty is estimated to be the standard deviation from the determined efficiency

over all standard runs, which leads to 12% statistical uncertainty.
Determination of the current before and after a run is only a linear approximation for the behavior of the current during the measurement. Artificially, this uncertainty is estimated as 10% which is rather conservative, since the current is indirectly monitored by the count rate in the detector and the ion-source output, as well as the transmission through the beamline, is stable. Further uncertainties are either canceled by the relative measurement to the standard (e.g. ion source yields, stripping yields or transmission through the beamline) or are negligibly small compared to the other uncertainties (e.g. timing or dead-time correction).

Systematic uncertainties are more problematic for data evaluation, because these uncertainties cannot be avoided or reduced by measurements.
The concentration of the standard sample is unknown up to 25%. This large systematic uncertainty arises from cross-calibrating this standard by other standard samples that also have uncertain concentrations and by uncertainties in the calibration measurement.
Another systematic uncertainty for the initial Fe content of the filter and water sample must be considered for the calculation because of the addition of carrier material. For the filter sample, the ICP-MS measurement of the initial sample, including the ash of the filters plus the later added carrier, is fully consistent with the outcome of chemistry. Therefore, the efficiency of chemistry is conservatively estimated to be between 90% and 100%. This results in a 3% systematic uncertainty for the initial mass of Fe in the filter from the ICP-MS measurement. For the water sample, the ICP-MS and the TXRF measurements are mostly consistent. For Fe, the variation between ICP-MS and TXRF is the highest. The efficiency of chemistry is estimated to be between 80% and 90% for the two column procedure. The outcome of chemistry is consistent with the estimated initial Fe content within 15% uncertainty.
Addition of carrier material does not introduce any considerable uncertainties further, since the used standard solutions and chemicals have precisely known concentrations and volumetric or gravimetric addition is accurate.

Statistical uncertainties are added quadratically and yield 17% uncertainty for the measurement without considering low count rates of the sample. The uncertainty of low count rates is also added quadratically to the already calculated 17%. The combined uncertainty of the measurement is the sum of systematic uncertainties and statistical uncertainties. For the total uncertainty in the initial concentration of the sample, the uncertainty of the initial Fe content is added linearly.

The systematic uncertainty of the standard sample only shifts the value for the concentration of the sample up and down. The same standard sample is used for blank and sample measurements. Therefore, this uncertainty is not considered for the determination, if the measured sample concentration is significantly above background. An uncertainty factor α could be defined which is 1 for the currently used value for the standard and can range from 0.75 up to 1.25 for the given uncertainty. α could be determined more precisely in later measurements, when new and less uncertain standard samples are available and a new calibration of the used STD standard is possible. The true concentration of ^{60}Fe in the sample after re-calibration of the standard material could be calculated by equation 4.14.

$$c_{true,^{60}Fe} = \alpha \cdot 1.3 \cdot 10^{-16} \cdot \frac{n_{^{60}Fe}}{n_{std}} \cdot \frac{Q_{std}}{Q_{^{60}Fe}} \cdot \frac{f_{std,live}}{f_{s,live}} \tag{4.14}$$

5 Experimental Results and Discussion

In the following chapter, the results of the measurements carried out in four beamtimes between October 2017 and March 2018 with 3 - 5 days per beamtime, are displayed and discussed. At first, the detection limit, which in this case is called sensitivity and was determined by blank measurements, is established. After that, the results for the Antarctic snow samples are presented, followed by a discussion about implications of these results.

5.1 Sensitivity of the Measurement

Ultra-sensitive measurements in the lowest concentration regime need highest sensitivities. The sensitivity for an AMS measurement is given in this context as the lowest possible concentration of the IoI in the sample to be detectable by the setup. For perfect background suppression the sensitivity of the measurement is no longer determined by background, but it is determined by the total efficiency of the setup.

The setup in Munich has a total efficiency for ^{60}Fe measurements around 10^{-4}. The total efficiency originates from the efficiency of the ion-source for producing negative ions (roughly 10^{-2}), the transmission through the whole beamline (10^{-1}), the stripping yield (10^{-1}) and the detection efficiency of the detector. This efficiency is fully compatible with the maximum expected concentration of ^{60}Fe in the water and in the filter samples. One has to mention, that this low amount of material and the very low expected concentrations are on the edge of detectability for ^{60}Fe. The determined detection efficiency for these samples is 60% because of extensive software cuts.

The sensitivity is determined by long blank measurements over hours. For each sample a chemistry blank is measured. Chemistry blanks are used to confirm that the chemistry is successful in removing most of the background and does not add the IoI to the actual samples. The absolute sensitivity is given by the lab blank, because this blank was already confirmed to be free from ^{60}Fe and was measured down to lowest levels.

For this project, a contamination of the samples with ^{60}Fe throughout the chemistry is highly unlikely. ^{60}Fe is not found on Earth in significant quantities and is only produced on Earth in dedicated facilities. Neither the facility in Dresden nor in Vienna produce or handle ^{60}Fe in quantities that could lead to any contamination. Radiotracers used in Vienna have been shown in the previous sections to be uncritical. Therefore, chemistry blanks are only needed to determine the amount of background in the samples and to compare them to the used lab blank.

A major part of this project is to separate Ni from Fe by chemistry to achieve a higher sensitivity in the AMS measurement. Several chemistry test samples were used to determine the relative amount of Ni background in the water sample compared to the clean lab blank (see Table i). Two chemical separation steps by ion-exchange columns are sufficient to reduce the Ni background for AMS. The actual samples contain slightly higher amounts of Ni than the lab blank which are still perfectly measurable under background-free conditions after software cuts. The difference between the Ni background rate for the Vienna sample and the Dresden samples is marginal. Additionally, the Vienna sample shows a cleaner spectrum than the Dresden samples which could be due to the additional purification step during chemistry or higher pureness of acids used for the chemistry.

Label	**^{60}Ni rate [events/nAs]**	**Details**
Fe 1 - Fe 14	60-120	One short column
Fe 15	5.0	Two short columns
Lab blank	4.0	Commercial Fe_2O_3 powder
Ag powder	3.5	Commercial Ag powder
D_1+D_2	8-10	Chemistry blank Dresden
V_1	6-8	Chemistry blank Vienna

Table i: GAMS suppressed ^{60}Ni background rate for different samples. The background rate is given as events in the histogram normalized to stable Fe current and measurement time. Fe 15 is at the same level as the lab blank. Samples from Vienna and Dresden are comparable in Ni, but the Vienna sample shows a slightly cleaner spectrum in critical ^{59}Co.

The absolute sensitivity achieved over the course of three beamtimes is $^{60}\mathrm{Fe}/\mathrm{Fe} = 2.5 \cdot 10^{-16}$. This concentration is an upper limit, given by the 1-σ interval by Feldman and Cousins [32] for zero events. It has to be mentioned that this absolute sensitivity is a cumulative sensitivity over four beamtimes. It is reasonable to use the cumulative sensitivity as absolute sensitivity and as blank level, because the settings of the system like the charge state for ^{60}Fe and therefore the stripping yield, the gas settings of the detector and the magnetic field of the GAMS, the type of ion-source and the material used for the determination of the single sensitivities are not changed from one beamtime to another.

The absolute sensitivity in this case is not limited by background events. For this project, full background suppression is achieved by the settings used for the measurement and software cuts. The limiting factor for the absolute sensitivity is the limited current output of the ion-source and the measurement time. One might argue that background could emerge at lower levels, but the lab blank was already measured down to $< 10^{-16}$ without background for similar settings [70].

A key point of the sensitivity determination is to analyze the background. Background has to be comparable for the blank runs and the sample runs in order to make sure that the sensitivity is achieved not only for blank measurements, but also for the sample. Therefore, each limiting background has to be quantified and possibly also identified to obtain reliable results and also to improve isotope suppression chemistry in the future.

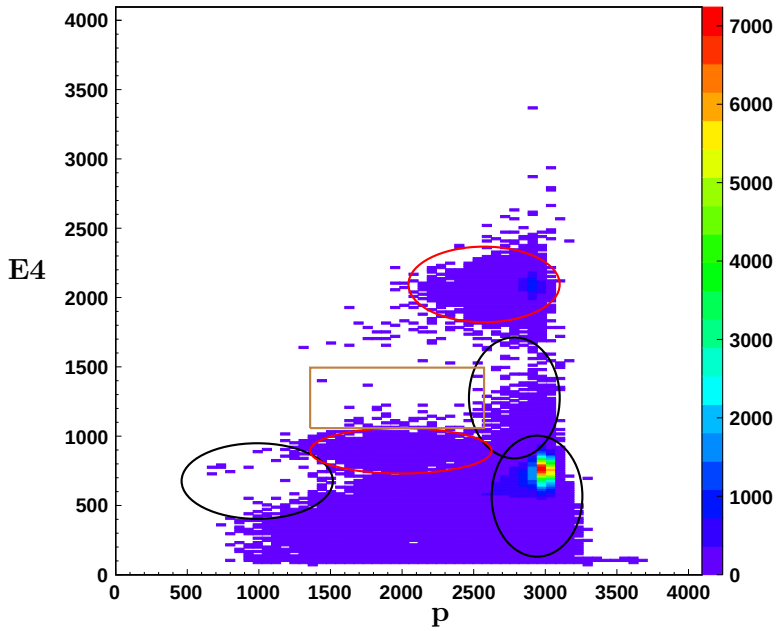

Figure 5.1: Background for ^{60}Fe measurements. Important background species are highlighted. Unidentified background in red is uncritical and easily suppressed by energy loss signals. ^{59}Co is the limiting background for the detection efficiency, whereas ^{60}Ni is the limiting background for the detector count rate (black, right). The ROI for ^{60}Fe is displayed in brown.

For the case of the Antarctic snow sample, the lab blank is cleaner in terms of background than the samples. Therefore, the lab blank was spiked with different contaminants to achieve comparability between the blanks and the samples. Chemistry blanks could also be used, but unfortunately B_D_1 yielded low currents in the ion-source and all chemistry blanks are significantly cleaner than the Antarctic samples.
At first, the amount of background in the sample runs is quantified and identified. For identification, a sample with different mixtures of possible contaminants (mostly m/q interferences and isotopes near the Fe mass region) is used to determine the nature of background. See Figure 6.3 in the Appendix for background identification. An important point is the nature of background and the impact on the sensitivity of the measurement. The background above and below the Region of Interest (ROI) of ^{60}Fe is uncritical (see Figure 5.1), since this kind of background is fully separated by other energy loss signals. Background identified as ^{76,77,78}Se^{13+} is less abundant in the measured samples and also separable in the ionization chamber. The most critical background is ^{60}Ni^{10+} and ^{59}Co^{10+}. ^{60}Ni^{10+} can lead to high count rates, but is fully separated in the spectra, whereas ^{59}Co^{10+} is only slightly abundant, but is near the ROI of ^{60}Fe.
After determining the background, sufficient background events are generated and added to the blank runs. In total, more than a factor of two more critical background events are in the combined blank runs than in the combined sample runs. Therefore, the sensitivity determined by the blank run is also reliable for the sample runs.
In the following, results for the Antarctic snow samples are displayed and discussed. The measurements were carried out in February and March 2018.

5.2 Results for Antarctic Snow Samples

In approximately 50 hours of measurement time, the filter samples, the water sample and several blank samples were measured for their ^{60}Fe content.
The two filter samples and the water sample yielded concentrations of ^{60}Fe/Fe significantly above background level with a total of 10 detected ^{60}Fe events.
See Figure 5.2 and Figure 5.3 for the events, obtained in the beamtime in March, in exemplary spectra and Table j for the evaluated results of the measurement including uncertainty treatment for the measurement. For full evaluation of all signals, see Figure 6.4 in the Appendix.
In addition to the measurements in March, an additional measurement was performed earlier in February, which is displayed in Figure 6.2. Here, two additional counts for the water samples were obtained.

Sample	**^{60}Fe counts**	**^{60}Fe/Fe**	**Upper Limit**	**Lower Limit**
Lab blank	0	0	$0.25 \cdot 10^{-15}$	n.a.
Filter (D_1 + D_2)	5	$0.55 \cdot 10^{-15}$	$0.88 \cdot 10^{-15}$	$0.29 \cdot 10^{-15}$
Water (V_1)	5	$0.90 \cdot 10^{-15}$	$1.44 \cdot 10^{-15}$	$0.47 \cdot 10^{-15}$

Table j: Measured concentration of the samples compared to the 1-σ upper limit of the spiked lab blank measurement. 1-σ upper and lower limits include already complete uncertainty treatment for the measurement.

The measured concentrations in the water and the filter samples are significantly above the background level of the lab blank which is also an upper limit for the sensitivity for this measurement. The total amount of background events from ^{59}Co in the filter samples is a factor of two lower than in the blank run, for the water sample the amount of ^{59}Co is a factor of seven lower than for the blank runs.

These results have to be converted to the real concentration of the samples and the number of atoms in the sample. Due to dilution with stable Fe by the addition of carrier material, the measured concentrations are lower than the real concentrations of the sample. Furthermore, an additional uncertainty by carrier addition has to be considered. This additional uncertainty does not affect the confidence in the signal, because the measurement uncertainties are not affected by the dilution process and are therefore independent. See Table k for the initial abundance of ^{60}Fe in the samples with full uncertainty treatment. Note, the calculated number of ^{60}Fe atoms in the samples is independent from any dilution, because only the measured concentration and the measured mass of the AMS sample has to be taken into account, which are precisely known.

As mentioned before, the systematic uncertainty of the concentration of the standard material leads only to linear shifts in the measured and calculated values. This uncertainty contribution is not taken into account. As introduced before, a numerical factor α could be used to scale the measured quantities according to a more precise value of the used standard.

	Filter Sample	Water Sample
Concentration ^{60}Fe/Fe	$1.1 \cdot 10^{-15}$	$3.5 \cdot 10^{-15}$
Upper Limit	$1.8 \cdot 10^{-15}$	$5.7 \cdot 10^{-15}$
Lower Limit	$0.5 \cdot 10^{-15}$	$1.6 \cdot 10^{-15}$
Atoms of ^{60}Fe	$4.9 \cdot 10^{4}$	$2.3 \cdot 10^{4}$
Upper Limit	$7.8 \cdot 10^{4}$	$3.6 \cdot 10^{4}$
Lower Limit	$2.5 \cdot 10^{4}$	$1.2 \cdot 10^{4}$

Table k: Determined concentration of ^{60}Fe in the samples, where an additional slight dilution by the ash of the filters has to be taken into account. The number of ^{60}Fe atoms in the full sample is unaffected from any dilution, because only precisely measured and not calculated values are taken into account.

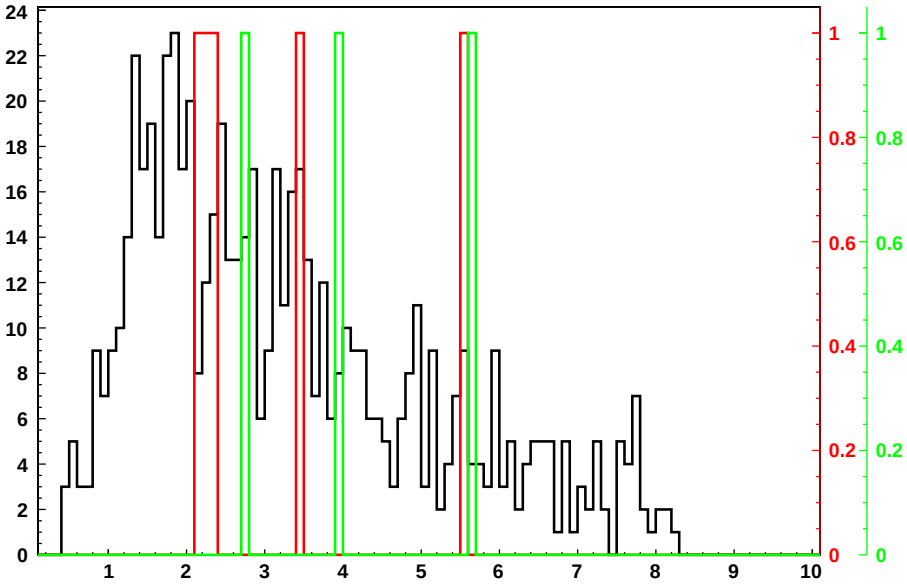

Figure 5.2: χ^2 distribution of the standard events with events from the filter samples (green) and water sample (red). χ^2 analysis is only used in addition to the more rigorous window conditions to check for major outliers. χ^2 could not be used in this case to distinguish completely between true events in the sample and false positives in the blank, because background events differ only in a few parameters from real events.

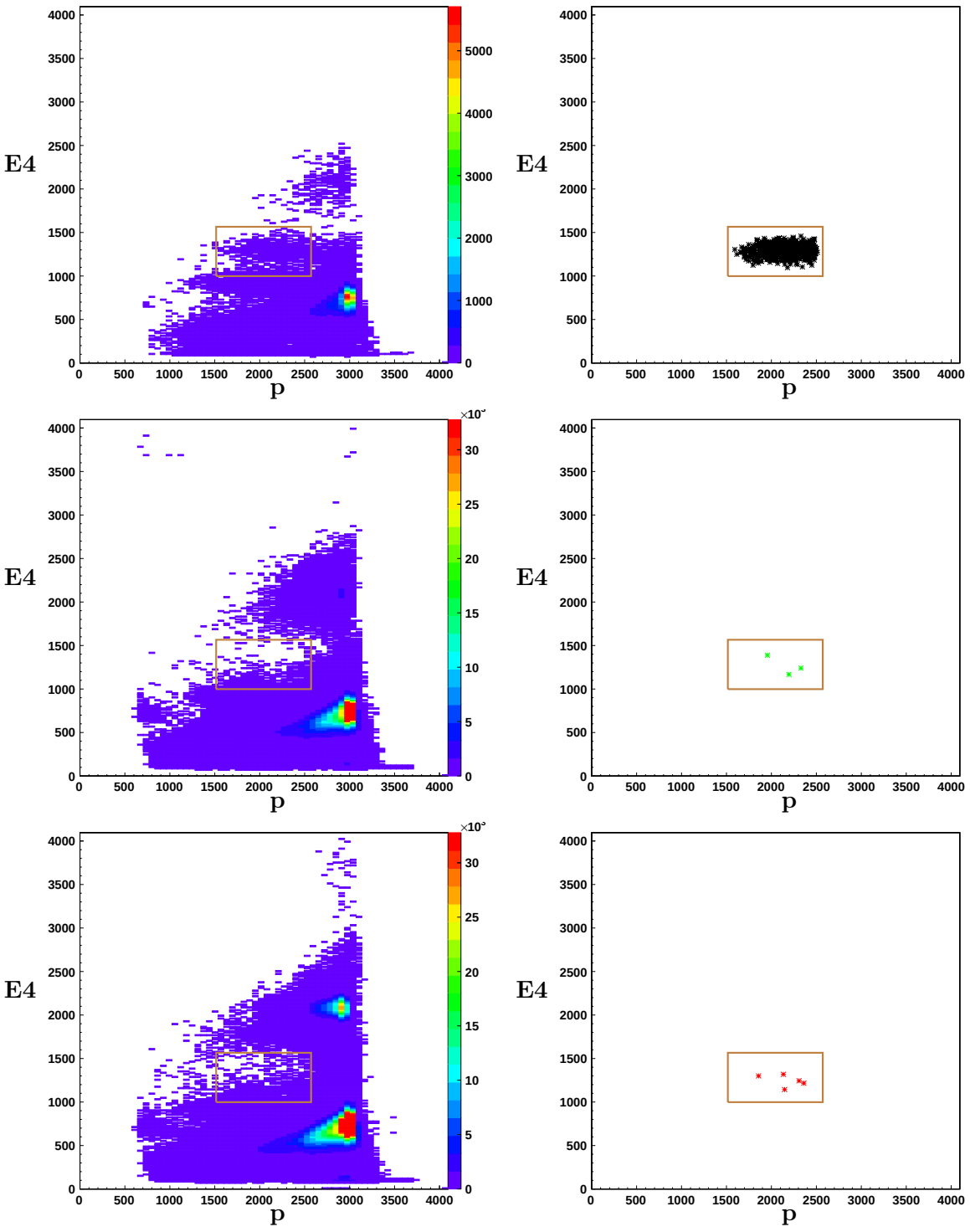

Figure 5.3: Spectra before (left) and after (right) software cuts for the measurement of the standard sample (top), the filter samples (middle) and the water sample (bottom). Three events are in the ROI of ^{60}Fe for the filter samples and five events are in the ROI for ^{60}Fe for the water sample. Additionally, two events from a previous beamtime have to be added to the filter sample.

5.3 Discussion of Results

^{60}Fe is present in the water as well as in the filter samples from Antarctica. The measured number of ^{60}Fe atoms in the samples could be compared to the estimated abundance and the amount of extraterrestrial material could be quantified. In a first approach, a purely cosmogenic signal is assumed in the water and the filter samples.

For the filter samples, a concentration of ^{60}Fe/Fe = $1.1 \cdot 10^{-15}$ is related to $4.9 \cdot 10^4$ atoms of ^{60}Fe in the filters. With the previously established production rate for ^{60}Fe from stable Ni [108], the amount of extraterrestrial Ni in the sample is m_{Ni}= 49 μg. Compared to the ICP-MS results for Ni (188 μg), the extraterrestrial Ni was diluted by terrestrial Ni. This could happen intrinsically in the reservoir by terrestrial input during the sampling of material, during transport or during chemistry. Furthermore, the amount of extraterrestrial Fe is also smaller than given by ICP-MS. 49 μg of extraterrestrial Ni would correspond to 0.8 mg of extraterrestrial Fe, in contrast to 4 mg from ICP-MS. An input of terrestrial Fe happens most likely during filtering the samples because of non-cleanroom conditions during this procedure.
49 μg of extraterrestrial Ni could be converted to 4.5 mg of extraterrestrial material of chondritic composition in the filters.
Note, larger particles were hand-picked from the filters prior to the chemistry for a later analysis by AMS after investigating their origin.

For the water sample, a more than three times higher concentration of ^{60}Fe/Fe = $3.5 \cdot 10^{-15}$ converts to slightly less atoms of ^{60}Fe due to stronger dilution by the addition of carrier material. $2.3 \cdot 10^4$ atoms of ^{60}Fe correspond to m_{Ni}= 22 μg of extraterrestrial Ni in the water. Again, after comparison with the amount of Ni deduced by ICP-MS and TXRF (200 μg - 250 μg), the sample is diluted by terrestrial Ni. In contrast to the filter samples, the amount of extraterrestrial Fe is less diluted by terrestrial Fe. Starting from 22 μg of extraterrestrial Ni, the amount of extraterrestrial Fe is 383 μg, less than suggested by the ICP-MS and TXRF results .
As before, the amount of chondritic material is calculated to be 2.1 mg in the water.

These results could be used to calculate the mass accretion rate of Earth per year, as it was already done in the past [20, 13]. Using e.g. 50 μg of extraterrestrial Ni that was deposited over one year of precipitation on 8 m^2 snow in Antarctica, the local flux of extraterrestrial Ni is around $6 \cdot 10^{-10}$ g/cm^2/yr. Furthermore by the two different sample sets, a distinction between smaller and possibly ablated particles and larger particles could be made. The total amount of extraterrestrial Ni found in Antarctica is around 70 μg, leading to an accretion rate of extraterrestrial Ni in Antarctica of around $1 \cdot 10^{-9}$ g/cm^2/yr. As mentioned before, this is only valid for the assumption that the measured signals are purely cosmogenic which has to be confirmed by a later measurement of ^{53}Mn or ^{41}Ca.

Another possible explanation of the measured concentrations would be that a significant contribution of interstellar, SN synthesized material is either in the water, in the filters or in both samples. This depends mostly on the ablation of dust in the atmosphere which could be different or comparable for ISD and IDP's. By this approach, a possibility to determine the accretion rate of Earth for interplanetary dust, as well as insight in interstellar dynamics and isotope enrichment, could be given.

The finding of ^{60}Fe in Antarctica supports cosmogenic production, whereas a LIC contribution based on previous SNe is not deducible by this measurement so far. For a direct SN signal or an enrichment of LIC material by ^{60}Fe, the maximum cosmogenic signal has to be exceeded significantly, or the cosmogenic signal has to be constrained further, for example by ^{53}Mn or ^{41}Ca measurements which have solely cosmogenic origin. By the follow up measurement of ^{53}Mn in the same sample set, the amount of cosmogenically produced ^{60}Fe could be quantified. Either these measurements show a significant excess of ^{60}Fe in one of the two samples or confirm these concentrations to be purely cosmogenic. For the case that ^{53}Mn or ^{41}Ca are solely in the filter or the water sample, the measurement of this ^{60}Fe concentration would directly become a double discovery of supernova and cosmogenically produced ^{60}Fe in Antarctica by AMS. Furthermore, this would constrain the ablation models for extraterrestrial dust in Earth's atmosphere and would give insight to differences in ISD and IDP's.

Nevertheless, this measurement yielded an extraterrestrially produced ^{60}Fe signal on Earth. This signal could be used to quantify the accretion of extraterrestrial material of Earth.

6 Summary and Outlook

In the framework of this Master's thesis, 500 kg of Antarctic surface snow were chemically processed and measured by AMS for any ^{60}Fe content.

Chemical treatment consisted of filtering the molten snow by filters with different pore sizes to obtain two sample sets, particles larger than 2 μm and smaller particles in the water. Both sample sets were chemically treated by ion-exchange chromatography to separate Fe from the other elements. ICP-MS and TXRF measurements were carried out to obtain the element content of the samples.

The chemical approach was modified for the water sample to yield less contamination with stable isotopes by the chemistry itself. By the usage of less concentrated acids, an additional purification step and cleaner materials, the suppression of interfering isotopes in the modified ion separation chemistry is comparable to the established procedure. Furthermore, the sample appeared to be cleaner in critical ^{59}Co and comparable in ^{60}Ni background in the AMS measurements.

AMS measurements to determine the ^{60}Fe content were carried out in Garching, Germany at the Maier-Leibnitz-Laboratory. Both sample sets yielded concentrations of ^{60}Fe above background which could be converted to the amount of initially present ^{60}Fe atoms in the sample. The measured concentrations suggest a cosmogenic origin of ^{60}Fe found in the samples, whereas an indication for a LIC origin can only be justified after follow-up measurements of different isotopes in the same sample set. In addition to this, the background of ^{60}Fe measurements was characterized and a new electronic background suppression, based on a Linear Gate and Stretcher, was installed.

Within this project, the first-ever detection of extraterrestrial ^{60}Fe by AMS with cosmogenic and/or SN origin in Antarctic snow was achieved. The measured number of ^{60}Fe atoms were $4.9 \cdot 10^4$ for the filter sample and $2.3 \cdot 10^4$ for the water sample with large uncertainties because of low counting statistics. These concentrations could be converted to an accretion rate for extraterrestrial Ni in Antarctica of around $10^{-9}\,\mathrm{g/cm^2/yr}$, considering this concentration to be purely cosmogenically produced ^{60}Fe.

The project could be improved by an even larger initial sample mass to yield more differentiated sample sets by adequate filtering. This would also yield a higher number of events in the measurement, which reduces the relative uncertainty by low counting statistics tremendously. Furthermore, different locations in Antarctica could be analyzed to confirm a uniform distribution of extraterrestrial material over Antarctica. The measurement itself could be improved to suppress the interfering ^{59}Co by adjusting the GAMS magnetic field and by dedicated suppression chemistry.

Followed by this project, the amount of ^{53}Mn and ^{41}Ca in the same sample set will be quantified by AMS to constrain the possible values for the extraterrestrial influx further. After establishing a precise value for the extraterrestrial influx in Antarctica by this three isotope approach, the global accretion rate could be calculated based on different models of matter dispersion on Earth. Triggered by this project, dated material e.g. from the Kohnen Station could be used to establish an accretion history of Earth, based on this three isotope approach.
By the measurement of ^{53}Mn and ^{41}Ca, the cosmogenically produced amount of ^{60}Fe will be constrained further and a possible LIC contribution might become apparent.

In addition to the actual sample sets, the handpicked and stored MM's in the filters will be evaluated. The amount has to be quantified as well as the composition and the elemental characteristics. By quantifying this fraction of the initial sample, the accretion of extraterrestrial matter will be specified further. An AMS measurement of these MM's will also reveal the irradiation history by radioisotope production. In total, the theory of accretion of extraterrestrial matter, including shifts in the size distribution by ablation will be refined in the future by the measurements of radioisotopes via AMS.

Appendix A: Isotope Data

Element	Abundance	Radionuclide Production
B	$6.9 \cdot 10^{-7}$	^{10}Be
C	$3.2 \cdot 10^{-2}$	^{10}Be
N	$3.2 \cdot 10^{-3}$	^{10}Be
O	$4.7 \cdot 10^{-1}$	^{3}He, ^{4}He, ^{10}Be
Na	$5.0 \cdot 10^{-3}$	^{21}Ne, ^{22}Ne
Mg	$9.6 \cdot 10^{-2}$	^{3}He, ^{4}He, ^{10}Be, ^{21}Ne, ^{22}Ne, ^{26}Al
Al	$8.5 \cdot 10^{-3}$	^{3}He, ^{4}He, ^{10}Be, ^{21}Ne, ^{22}Ne, ^{26}Al
Si	$1.1 \cdot 10^{-1}$	^{3}He, ^{4}He, ^{10}Be, ^{21}Ne, ^{22}Ne, ^{26}Al
S	$5.4 \cdot 10^{-2}$	^{21}Ne, ^{22}Ne, ^{26}Al
K	$5.4 \cdot 10^{-4}$	^{36}Cl
Ca	$9.3 \cdot 10^{-3}$	^{21}Ne, ^{22}Ne, ^{26}Al, ^{36}Cl, ^{36}Ar, ^{38}Ar
Ti	$4.6 \cdot 10^{-4}$	^{10}Be, ^{26}Al, ^{36}Cl
Fe	$1.8 \cdot 10^{-1}$	noble gases, ^{10}Be, ^{26}Al, ^{36}Cl, ^{41}Ca, ^{53}Mn
Ni	$1.1 \cdot 10^{-2}$	noble gases, ^{10}Be, ^{26}Al, ^{36}Cl, ^{41}Ca, ^{53}Mn, ^{60}Fe

Table l: Adopted abundances of elements in meteorites, used for the calculation of radionuclide production as well as for the later calculation of the accretion of extraterrestrial matter. Target elements, as well as produced radionuclides, are displayed. Values obtained by R. Trappitsch and I. Leya [108], adopted from [90].

Target Size [μm]	**50 MV** [dpm/kg]	**75 MV** [dpm/kg]	**100 MV** [dpm/kg]	**125 MV** [dpm/kg]	**150 MV** [dpm/kg]
2.5	0.07	0.18	0.29	0.40	0.50
4.0	0.08	0.20	0.32	0.44	0.55
6.0	0.08	0.21	0.34	0.46	0.57
8.0	0.09	0.21	0.34	0.47	0.59
10	0.09	0.21	0.35	0.48	0.60
15	0.09	0.22	0.36	0.49	0.61
20	0.09	0.22	0.36	0.49	0.62
25	0.09	0.22	0.36	0.50	0.62
50	0.09	0.23	0.37	0.50	0.63
100	0.09	0.23	0.37	0.50	0.63
150	0.09	0.23	0.37	0.51	0.63
200	0.09	0.23	0.37	0.51	0.63

Table m: Calculated cosmogenic production rates for ^{60}Fe by SCR spallation on Ni targets. Different target sizes are assumed for different SCR rigidities and a proton flux of 100 cm^{-2} s^{-1}. Data gratefully obtained by R. Trappitsch and I. Leya [108].

Appendix B: Analytical Techniques

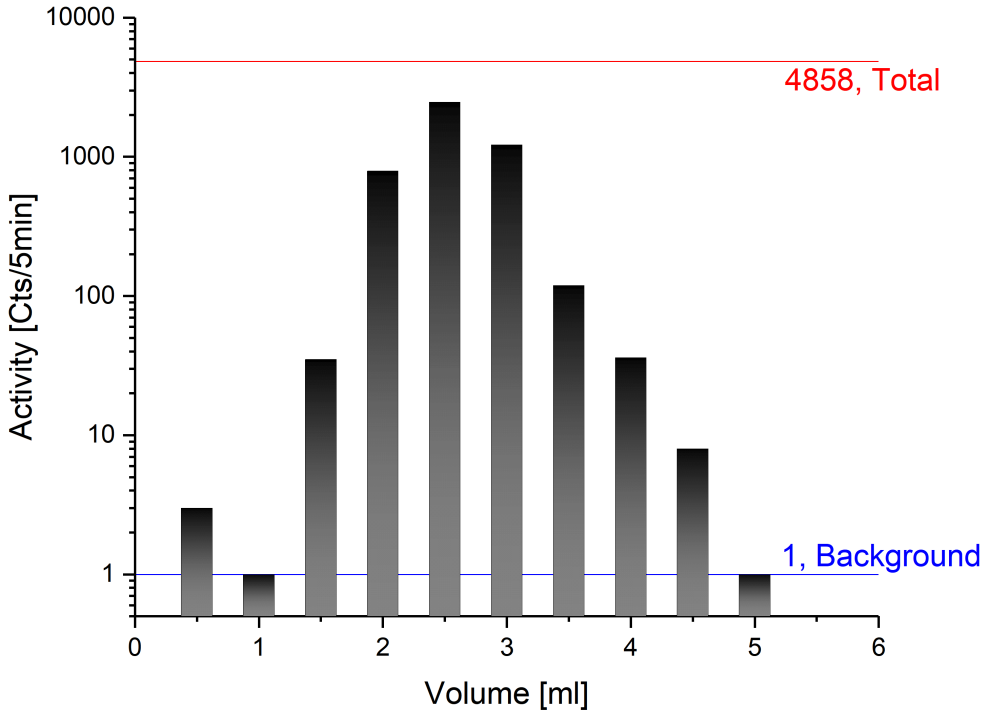

Figure 6.1: Elution of the ^{54}Mn tracer by ion-exchange chromatography, measured by γ-ray spectroscopy. 0.5 ml batches in chronological order with their ^{54}Mn content (logarithmic scale) are displayed. After 5 ml of HCl (6 M), all ^{54}Mn is eluted from the column. ^{54}Mn is a proxy for Mn, Cr and Ni in the water sample.

Label	Injector [Gauss]	Current [nA]	Mass	Composition
I	643	40	1	$^{1}H^{-}$
II	2206	11	12	$^{12}C^{-}$
II	2296	6.5	13	$^{12}CH^{-}$
II	2546	25000	16	$^{16}O^{-}$
II	2624	650	17	$^{16}OH^{-}$
II	2700	55	18	$^{18}O^{-}$
II	2771	7.0	19	$^{18}OH^{-}$
III	3599	200	32	$^{16}O_2^{-}$
III	3656	15	33	$^{16}O_2H^{-}$
III	3819	1.0	36	$^{18}O_2^{-}$
IV	4678	8.0	54	$^{54}Fe^{-}$
IV	4762	150	56	$^{56}Fe^{-}$
IV	4806	4.0	57	$^{57}Fe^{-}$
IV	5050	32	63	$^{63}Cu^{-}$
IV	5126	15	65	$^{65}Cu^{-}$
IV	5322	100	70	$^{54}Fe^{16}O^{-}$
IV	5396	1550	72	$^{56}Fe^{16}O^{-}$
IV	5433	45	73	$^{57}Fe^{16}O^{-}$
IV	5900	35	86	$^{54}Fe^{16}O_2^{-}$
IV	5965	400	88	$^{56}Fe^{16}O_2^{-}$
IV	6001	18	89	$^{57}Fe^{16}O_2^{-}$
V	6419	23	102	$^{54}Fe^{16}O_3^{-}$
V	6507	200	104	$^{56}Fe^{16}O_3^{-}$
V	6578	2750	107	$^{107}Ag^{-}$
V	6640	2500	109	$^{109}Ag^{-}$
V	6707	80	112	$^{56}Fe_2^{-}$
VI	7055	100	123	$^{107}Ag^{16}O^{-}$
VI	7111	95	125	$^{109}Ag^{16}O^{-}$
VII	8117	7.5	163	$^{107}Ag^{56}Fe^{-}$
VII	8166	7.0	165	$^{109}Ag^{56}Fe^{-}$
VII	8507	38	179	$^{107}Ag^{56}Fe^{16}O^{-}$
VII	8552	32	181	$^{109}Ag^{56}Fe^{16}O^{-}$
VIII	9301	68	214	$^{107}Ag_2^{-}$
VIII	9347	125	216	$^{107/109}Ag_2^{-}$
VIII	9385	60	218	$^{109}Ag_2^{-}$

Table n: Mass spectrometry at the injector magnet for Fe_2O_3 + Ag in Ag cathodes. Injector field is given in Gauss (10^{-4} T) and composition is the most probable composition of the detected ions. Typical molecules like FeO as well as atomic ions like C or O could be observed, where fractionation especially for low mass atomic ions has to be considered [80]. Deviations from the isotopic abundance could be attributed to neighboring species with different mass and/or energy. Labels I-VIII indicate groups of ions in the same mass range. See Figure 4.8 for the corresponding histogram.

Appendix C: Acquired Data from AMS

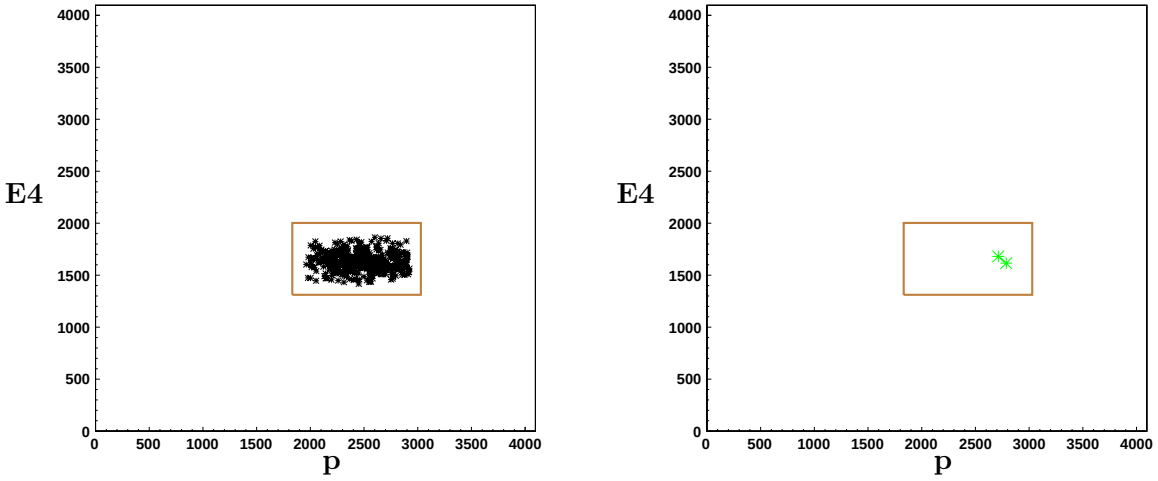

Figure 6.2: Spectrum after software cuts for the measurement of the filter samples (green, right) during the beamtime in February compared to the standard events (black, left). Two events are in the ROI for ^{60}Fe. For this measurement, background-free conditions apply after software cuts.

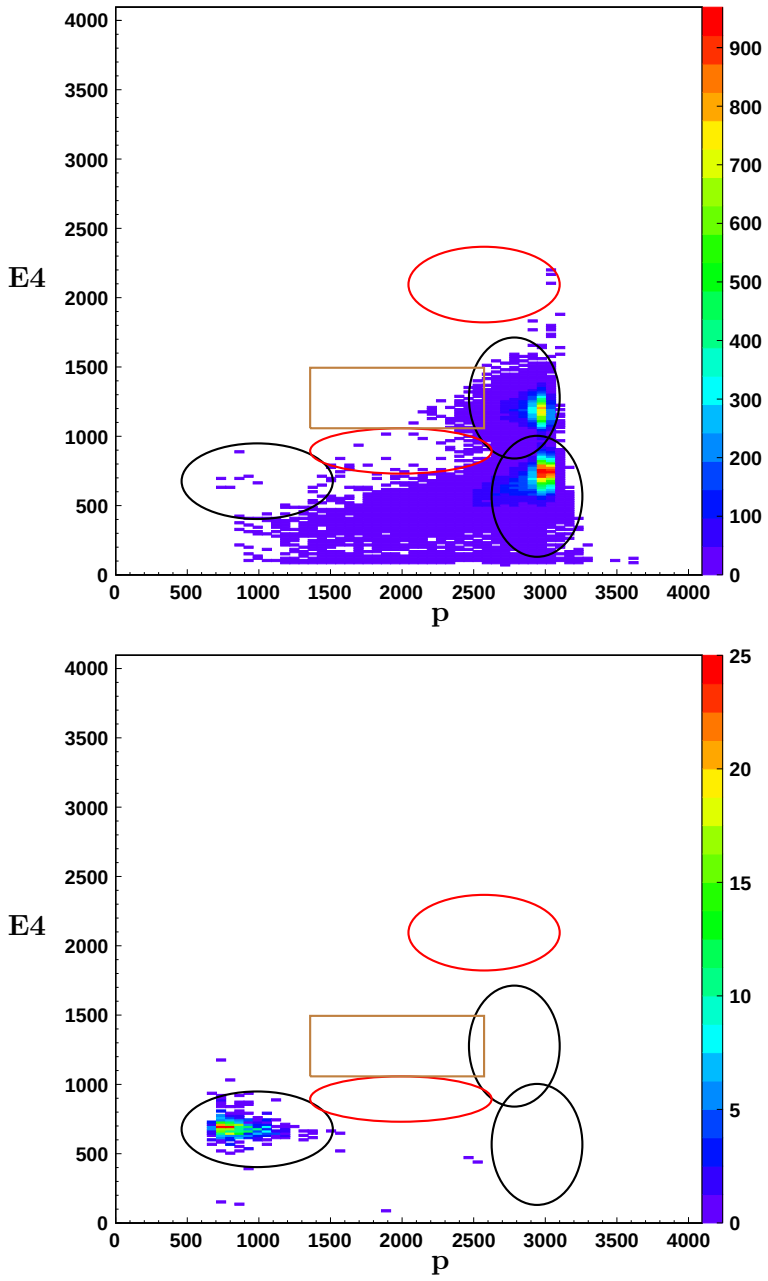

Figure 6.3: Background identification for ^{60}Fe runs. Top: Measurement of pure CoO. $^{59}Co^{10+}$ is detected besides $^{60}Ni^{10+}$. Bottom: Measurement of pure Se. $^{76}Se^{13+}$, $^{77}Se^{13+}$ and $^{78}Se^{13+}$ are possible candidates to be detected.

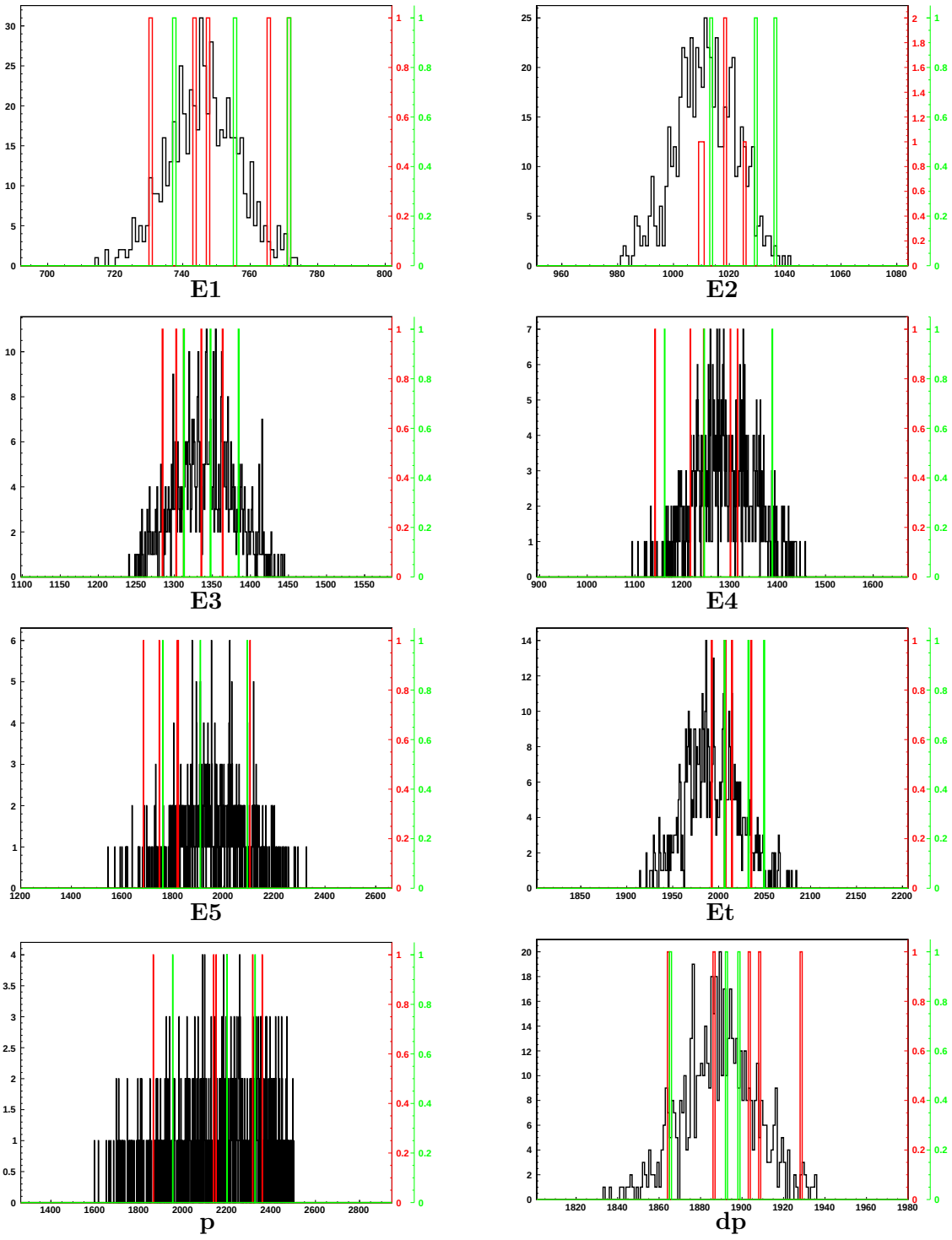

Figure 6.4: 1-D histograms for the standard (black), filter (green) and the water (red) measurements. Anodes from E1 to E5, Et, position and x-angle are displayed. For Et and E2, shifts in the signals to higher values occurred during the measurement of the water and the filter samples, which was verified by a late standard measurement.

Appendix D: Linear Gate and Stretcher

The IoI and its isobar enter at slightly different energies and positions the ionization chamber after the GAMS. In the gas of the ionization chamber, the IoI and its isobar lose energy according to Figure 4.9. For cases depicted as (Z,Z'), where the IoI has a lower nuclear charge than its isobar, the isobar could be stopped in the ionization chamber before the IoI. In these cases, the energy loss of the isobar induces a positive bipolar signal after signal processing at the fourth anode but no positive bipolar signal at the last anode. The positive signal on the fourth anode induces then a negative signal at the last anode by mirror charge effects. This negative, inverted signal leads to a positive signal in the spectra because of its bipolar structure and the long gate length of the master-gate for pile-up rejection (see [70] for a detailed description of the installed signal processing elements). After all, stopping of the isobar at the fourth anode does not lead to a significant improvement in isobaric suppression. One way to overcome this problem is to switch to unipolar signals which introduces timing problems for high count rates because of the long time needed for pole-zero adjustment. Another way to solve this problem is to stay with bipolar signals and to discard inverted signals.

For this issue, a Linear Gate and Stretcher (LGS) is installed. A new, short gate is used to check for positive signals from E5 within the gate length. If a positive signal is within the gate, a rectangular signal with the same amplitude as the bipolar signal is transmitted to data processing. The rectangular signal is delayed compared to the bipolar signal from the amplifier and shaper, but within the master gate length. Any inverted signal does not lead to a positive output, if the gate length of the LGS is short enough to cover only the negative part of the bipolar signal.

This concept was tested the first time with pure ^{60}Ni from a lab blank. The pressure was adjusted in such a way that some events produce inverted signals in E5 (43 mbar, 11.5 MV, q = 10+). All inverted signals are removed and the amount of background is reduced (see Figure 6.5). Furthermore, the suppression capability of the LGS for the case of Fe-Ni was investigated. A sample, containing macroscopic amounts of Ni and Fe was used to examine the suppression of ^{58}Ni compared to ^{58}Fe which are both stable isobars and which is the same situation as for ^{60}Ni and ^{60}Fe. Different gas pressures were used to obtain different scenarios with higher or lower amount of inverted signals. Increasing gas pressure leads to more and more inverted signals from Ni and from Fe, leading to full suppression of Ni at the expense of high losses of Fe (see Figure 6.6).

For the case of Fe-Ni, LGS is not needed because of good separation in all energy channels and in position. For ^{99}Tc, additional suppression of background can lead to higher sensitivities or new measurement techniques like measurements of ^{99}Tc relative to ^{97}Tc.

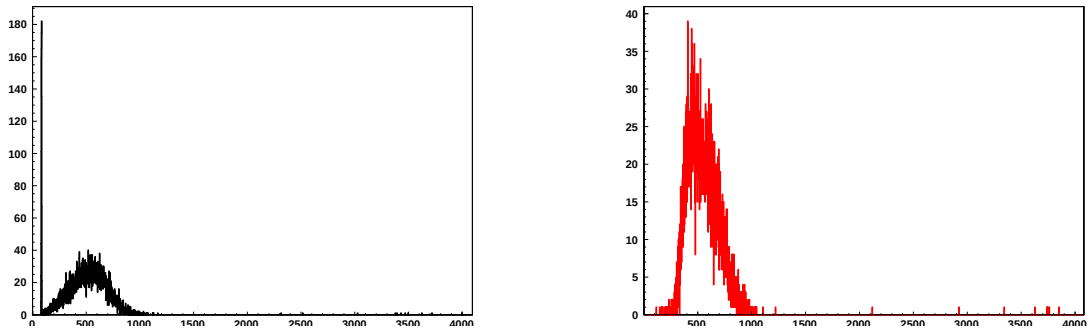

Figure 6.5: ^{60}Ni events in E5 with LGS (left, black) and without LGS (right, red). All inverted signals from the right histogram, which are not externally discernible inverted signals, are removed in the left histogram and acquired at minimum pulse height, considerably distant from the maximum of the peak.

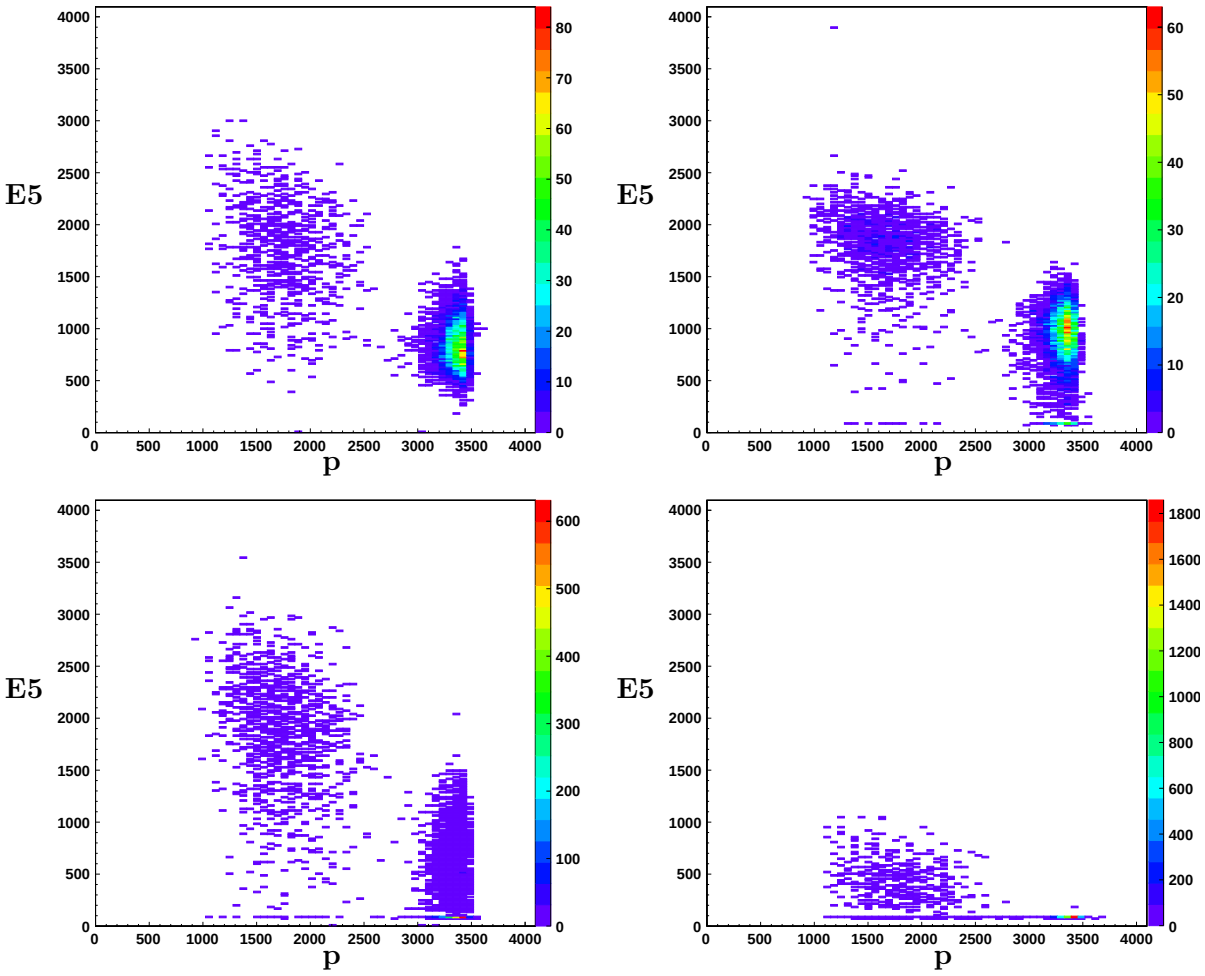

Figure 6.6: Coincident measurement of ^{58}Fe (left in each histogram) and ^{58}Ni (right in each histogram). Top left: 35 mbar without LGS. Top right: 32.5 mbar with LGS. Bottom left: 35.0 mbar with LGS. Bottom right: 37.5 mbar with LGS.

Appendix E: Extraterrestrial Matter

Element	Figure 3.2 [wt %]	Figure 6.8 [wt %]	Figure 6.9 [wt %]
O	40.9	28.2	45.3
Na	0.7	2.8	9.5
Mg	25.7	1.0	3.0
Al	1.3	1.4	3.2
Si	15.9	6.3	28.7
S	0.0	0.1	0.3
Ca	0.5	2.0	6.7
Ti	0.0	0.8	0.0
Fe	15.1	57.0	2.7

Table o: EDX analysis of the displayed dust grains for their element content. Large variations between different dust grains are apparent. Further examination of the dust grains and AMS measurements will reveal the origins of the grains.

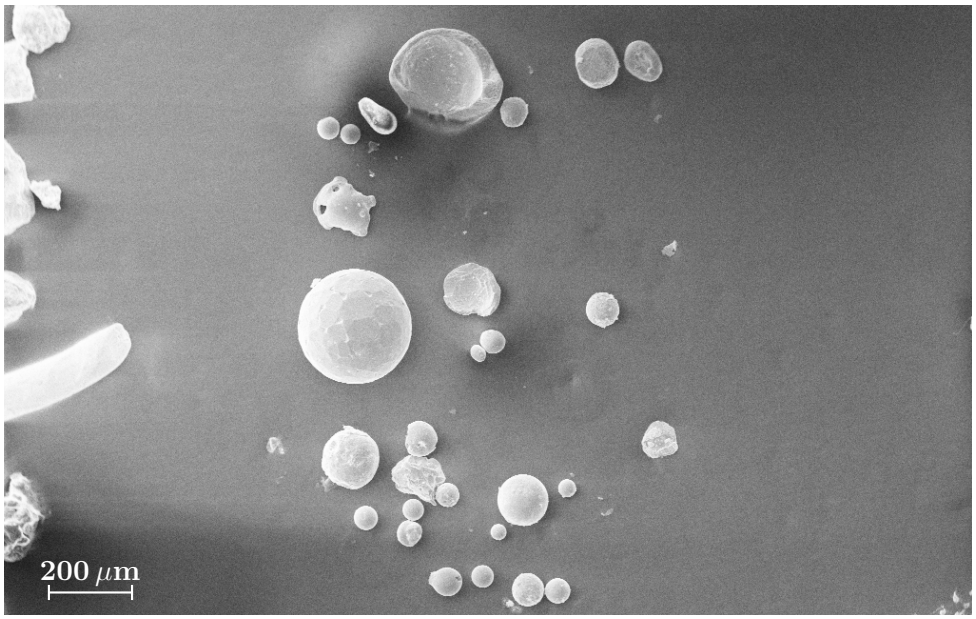

Figure 6.7: Collection of several dust grains that were collected from the filters. In total, more than 150 grains were handpicked and will be analyzed further.

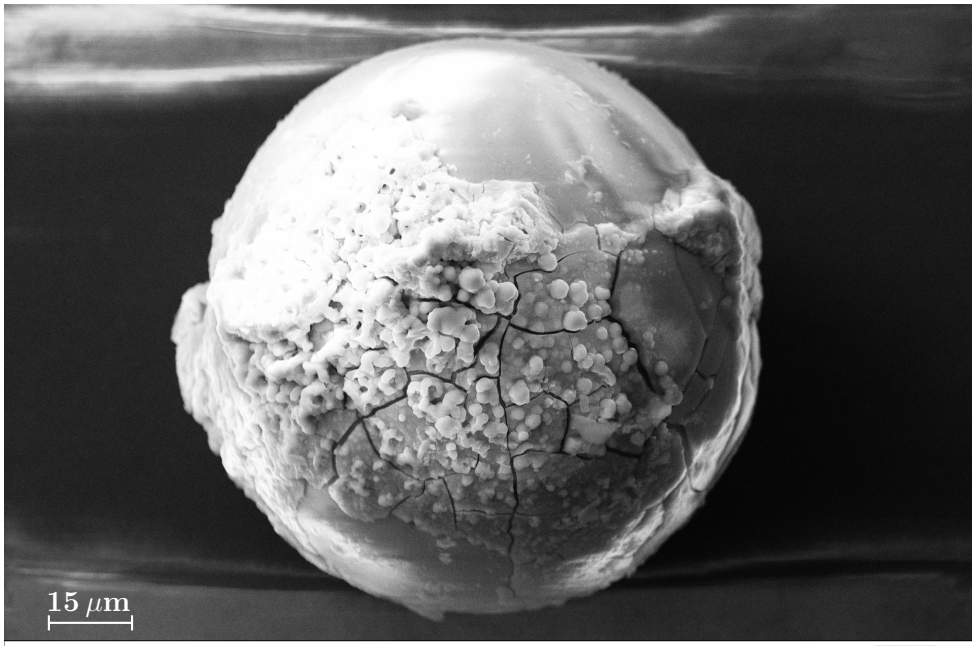

Figure 6.8: Picture of an exemplary dust grain collected from the filter. This grain consists mostly of Fe and O. The grain is 100 μm in diameter.

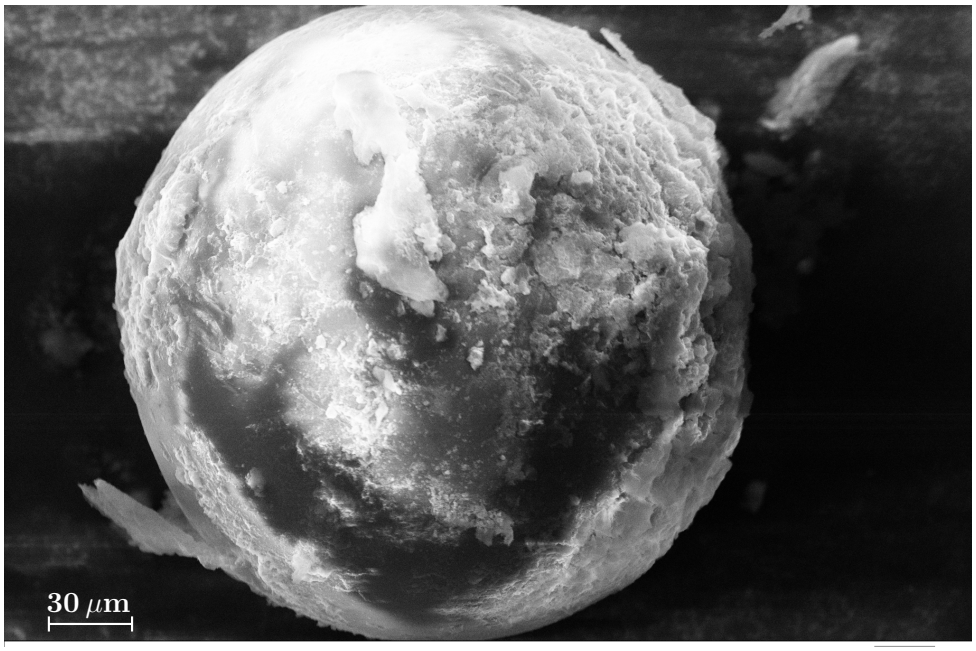

Figure 6.9: Picture of an exemplary dust grain collected from the filter. This grain consists mostly of O and Si. The grain is 100 μm in diameter.

List of Abbreviations

AGB Asymptotic Giant Branch

AMM Antarctic Micro Meteorites

AMS Accelerator Mass Spectrometry

BH Black Hole

CCSN Core Collapse Supernova

CKT Chemical Kinetic Theory

CNT Classical Nucleation Theory

ECSN Electron Capture Supernova

ED phase Ejecta Dominated phase

EDX Energy Dispersive X-ray spectroscopy

FWHM Full Width Half Maximum

GAMS Gas-filled Analyzing Magnet System

GCR Galactic Cosmic Rays

GVM Generating Voltmeter

HE High Energy

HRD Hertzsprung Russell Diagram

HZDR Helmholtz-Zentrum Dresden-Rossendorf

ICP-MS Inductively Coupled Plasma Mass Spectrometry

IDP Interplanetary Dust Particle

IoI Isotope of Interest

ISD Interstellar Dust

ISM Interstellar Medium

LB Local Bubble

LE Low Energy

LGS Linear Gate Stretcher

LIC Local Interstellar Cloud

LNHB Laboratoire National Henri Becquerel

MCP Micro Channel Plate

MLL Maier-Leibnitz-Laboratorium

MM Micrometeorites

NS Neutron Star

NS-NS merger Neutron Star mergers

NSE Nuclear Statistical Equilibrium

PIPS Passivated Implanted Planar Silicon

ppb parts per billion

ppm parts per million

r-process rapid neutron capture process

ROI Region of Interest

s-process slow neutron capture process

SCR Solar Cosmic Rays

SN Supernova

SNR Supernova Remnant

SP phase Snow-Plough phase

ST phase Sedov-Taylor phase

TNSN Thermonuclear Supernovae

ToF Time-of-Flight

TXRF Total Reflection X-Ray Fluorescence

WD White Dwarf

List of Figures

List of Tables

Bibliography

[1] B. Abbott et al. “GW170817: Observation of Gravitational Waves from a Binary Neutron Star Inspiral”. In: *Phys. Rev. Lett.* 119 (2017), p. 161101.

[2] O. Abollino et al. “Determination of copper, cadmium, iron, manganese, nickel and zinc in Antarctic sea water. Comparison of electrochemical and spectroscopic procedures”. In: *Analytica Chimica Acta* 305.1 (1995), pp. 200–206.

[3] S. Adams et al. “Observing the Next Galactic Supernova”. In: *The Astrophysical Journal* 778.2 (2013), p. 164.

[4] A. Andersen. “Dust from AGB Stars”. In: *Astronomical Society of the Pacific Conference Series* 378 (2008), p. 170.

[5] T. Athanassiadou and B. Fields. “Penetration of nearby supernova dust in the inner solar system”. In: *New Astronomy* 16.4 (2011), pp. 229–241.

[6] M. Beech. “The past, present and future supernova threat to Earths biosphere”. In: *Astrophysics and Space Science* 336 (2011), pp. 287–302.

[7] M. Belyaev and R. Rafikov. “The Dynamics of Dust Grains in the Outer Solar System”. In: *The Astrophysical Journal* 723.2 (2010), p. 1718.

[8] C. Bennet et al. “Radiocarbon Dating Using Electrostatic Accelerators: Negative Ions Provide the Key”. In: *Science* 198.4316 (1977), pp. 508–510.

[9] T. Berghoefer and D. Breitschwerdt. “The origin of the young stellar population in the solar neighborhood — A link to the formation of the Local Bubble?” In: *Astronomy and Astrophysics* 390.1 (2002), pp. 299–306.

[10] H. Bethe. “Supernova Mechanisms”. In: *Reviews of Modern Physics* 62.4 (1990), pp. 801–866.

[11] H. Betz. “Charge States and Charge-Changing Cross Sections of Fast Heavy Ions Penetrating Through Gaseous and Solid Media”. In: *Rev. Mod. Phys.* 44 (1972), pp. 465–539.

[12] S. Bianchi and R. Schneider. “Dust formation and survival in supernova ejecta”. In: *Monthly Notices of the Royal Astronomical Society* 378.3 (2007), pp. 973–982.

[13] R. Bibron et al. “Extra-terrestrial 53Mn in Antarctic ice”. In: *Earth and Planetary Science Letters* 21.2 (1974), pp. 109–116.

[14] W. Binns et al. “Observation of the 60Fe nucleosynthesis-clock isotope in galactic cosmic rays”. In: *Science* (2016).

[15] G. Birnbaum et al. “Synoptic situations causing high precipitation rates on the Antarctic plateau: observations from Kohnen Station, Dronning Maud Land”. In: *Antarctic Science* 18.2 (2006), pp. 279–288.

[16] P. Bland et al. “The flux of meteorites to the Earth over the last 50 000 years”. In: *Monthly Notices of the Royal Astronomical Society* 283.2 (1996), p. 551.

[17] M. Bocchio et al. “Dust grains from the heart of supernovae”. In: *Astronomy and Astrophysics* 587 (2016), A157.

[18] D. Breitschwerdt and M. de Avillez. “The history and future of the Local and Loop I bubbles”. In: *Astronomy and Astrophysics* 452.1 (2006), pp. L1–L5.

[19] D. Breitschwerdt et al. “The locations of recent supernovae near the Sun from modelling 60Fe transport”. In: *Nature* 532 (2016), pp. 73–76.

[20] J. Brocas and E. Picciotto. “Nickel content of antarctic snow: Implications of the influx rate of extraterrestrial dust”. In: *Journal of Geophysical Research* 72.8 (1967), pp. 2229–2236.

[21] D. Brownlee. “Cosmic Dust: Collection and Research”. In: *Annual Review of Earth and Planetary Sciences* 13.1 (1985), pp. 147–173.

[22] R. Brun and F. Rademakers. “ROOT - An Object Oriented Data Analysis Framework”. In: *Nuclear Instruments & Methods in Physics Research A* 389 (1997), pp. 81–86.

[23] E. Burbidge et al. “Synthesis of the Elements in Stars”. In: *Reviews of Modern Physics* 29.4 (1957), pp. 547–650.

[24] I. Cherchneff. “Dust production in Supernovae”. In: *The Life Cycle of Dust in the Universe: Observations, Theory, and Laboratory Experiments*. 2013.

[25] A. Chieffi and M. Limongi. “Pre-supernova Evolution of Rotating Solar Metallicity Stars in the Mass Range 13-120 $M_{\odot}$ and their Explosive Yields”. In: *The Astrophysical Journal* 764.1 (2013), p. 21.

[26] F. Dell’Agli. “Modelling dust production in AGB stars”. In: *Proceedings of the International Astronomical Union* 12.S323 (2016), pp. 165–168.

[27] F. Dell’Agli et al. “Asymptotic giant branch and super-asymptotic giant branch stars: modelling dust production at solar metallicity”. In: *Monthly Notices of the Royal Astronomical Society* 467.4 (2017), pp. 4431–4440.

[28] E. Dobrica et al. “Connection between micrometeorites and Wild 2 particles: From Antarctic snow to cometary ices”. In: *Meteoritics & Planetary Science* 44.10 (2009), pp. 1643–1661.

[29] R. Dodson et al. “The Extraction of Ferric Chloride from Hydrochloric Acid Solutions by Isopropyl Ether”. In: *Journal of the American Chemical Society* 58.12 (1936), pp. 2573–2577.

[30] E. Dwek. “Iron: A Key Element for Understanding the Origin and Evolution of Interstellar Dust”. In: *The Astrophysical Journal* 825.2 (2016), p. 136.

[31] B. Elmegreen. “Grain formation behind shocks and the origin of isotopically anomalous meteoritic inclusions”. In: *The Astrophysical Journal* 251 (1981), pp. 820–833.

[32] G. Feldman and R. Cousins. “Unified approach to the classical statistical analysis of small signals”. In: *Phys. Rev. D* 57 (1998), pp. 3873–3889.

[33] B. Fields et al. “Supernova Collisions with the Heliosphere”. In: *The Astrophysical Journal* 678.1 (2008), p. 549.

[34] L. Fimiani et al. “Interstellar 60Fe on the Surface of the Moon”. In: *Phys. Rev. Lett.* 116 (2016), p. 151104.

[35] D. Fink. “AMS-11 in Rome, 2008: Past achievements, current and future trends”. In: *Nuclear Instruments and Methods in Physics Research Section B: Beam Interactions with Materials and Atoms* 268.7 (2010). Proceedings of the Eleventh International Conference on Accelerator Mass Spectrometry, pp. 1334–1342.

[36] C. Fitoussi et al. “Search for supernova-produced 60Fe in a marine sediment”. In: *Physical Review Letters* 101.121101 (2008), pp. 1–15.

[37] P. Frisch. “The galactic environment of the Sun”. In: *Journal of Geophysical Research: Space Physics* 105.A5 (2000), pp. 10279–10289.

[38] B. Fry et al. “Astrophysical Shrapnel: Discriminating among Near-Earth Stellar Explosion Sources of Live Radioactive Isotopes”. In: *The Astrophysical Journal* 800.1 (2015), p. 71.

[39] B. Fry et al. “Radioactive Iron Rain: Transporting 60Fe in Supernova Dust to the Ocean Floor”. In: *The Astrophysical Journal* 827.1 (2016), p. 48.

[40] B. Fuchs et al. “The search for the origin of the Local Bubble redivivus”. In: *Monthly Notices of the Royal Astronomical Society* 373.3 (2006), pp. 993–1003.

[41] P. Gabrielli et al. “Meteoric smoke fallout over the Holocene epoch revealed by iridium and platinum in Greenland ice”. In: *Nature* 432 (2004), pp. 1011–1014.

[42] C. Gall et al. “Rapid formation of large dust grains in the luminous supernova 2010jl”. In: *Nature* 511 (2014), pp. 326–329.

[43] N. Gehrels et al. “Ozone Depletion from Nearby Supernovae”. In: *The Astrophysical Journal* 585.2 (2003), p. 1169.

[44] M. Genge et al. “The textures and compositions of fine-grained Antarctic micrometeorites: Implications for comparisons with meteorites”. In: *Geochimica et Cosmochimica Acta* 61.23 (1997), pp. 5149–5162.

[45] H. Gomez. “Dust in Supernova Remnants”. In: *The Life Cycle of Dust in the Universe: Observations, Theory, and Laboratory Experiments*. 2013.

[46] M. Goodson et al. “Chemical enrichment of the pre-solar cloud by supernova dust grains”. In: *Monthly Notices of the Royal Astronomical Society* 462.3 (2016), pp. 2777–2791.

[47] M. Gounelle et al. “Supernova Propagation and Cloud Enrichment: A New Model for the Origin of 60Fe in the Early Solar System”. In: *The Astrophysical Journal Letters* 694.1 (2009), p. L1.

[48] E. Gruen et al. “Discovery of Jovian dust streams and interstellar grains by the Ulysses spacecraft”. In: *Nature* 362 (1993), pp. 428–430.

[49] K. Hain et al. “AMS of 93Zr: Passive absorber versus gas-filled magnet”. In: *Nuclear Instruments and Methods in Physics Research Section B: Beam Interactions with Materials and Atoms* 423 (2018), pp. 42–48.

[50] M. Hashimoto. “Supernova Nucleosynthesis in Massive Stars”. In: *Progress of Theoretical Physics* 94.5 (1995), pp. 663–736.

[51] A. Heger et al. “How Massive Single Stars End Their Life”. In: *The Astrophysical Journal* 591.1 (2003), p. 288.

[52] C. Iliadis. *Nuclear Physics of Stars*. Wiley-VCH Verlag GmbH, 2008, p. 637.

[53] R. Indebetouw et al. "Dust Production and Particle Acceleration in Supernova 1987A Revealed with ALMA". In: *The Astrophysical Journal Letters* 782.1 (2014), p. L2.

[54] H.-Th. Janka. "Explosion Mechanisms of Core-Collapse Supernovae". In: *Annual Review of Nuclear and Particle Science* 62.1 (2012), pp. 407–451.

[55] S. Jones et al. "Advanced Burning Stages and Fate of 8-10 Solar Mass Stars". In: *The Astrophysical Journal* 772.2 (2013), p. 150.

[56] F. Kaeppeler et al. "The s-process: Nuclear physics, stellar models, and observations". In: *Rev. Mod. Phys.* 83 (2011), pp. 157–193.

[57] H. Kimura et al. "Composition, Structure, and Size Distribution of Dust in the Local Interstellar Cloud". In: *The Astrophysical Journal* 583.1 (2003), p. 314.

[58] H. Kimura et al. "Elemental Abundances and Mass Densities of Dust and Gas in the Local Interstellar Cloud". In: *The Astrophysical Journal* 582.2 (2003), p. 846.

[59] K. Knie et al. "60Fe Anomaly in a Deep-Sea Manganese Crust and Implications for a Nearby Supernova Source". In: *Phys. Rev. Lett.* 93 (2004), p. 171103.

[60] K. Knie et al. "Accelerator mass spectrometry measurements and model calculations of iron-60 production rates in meteorites". In: *Meteoritics & Planetary Science* 34.5 (1999), pp. 729–734.

[61] K. Knie et al. "Indication for Supernova Produced 60Fe Activity on Earth". In: *Physical Review Letters* 83.1 (1999), pp. 18–21.

[62] D. Koll et al. "Recent Developments for AMS at the Munich Tandem Accelerator". In: *Nuclear Instruments & Methods in Physics Research B* (accepted).

[63] G. Korschinek. "Mass Extinctions and Supernova Explosions". In: *Handbook of Supernovae*. Ed. by A. Alsabti and P. Murdin. Cham: Springer International Publishing, 2017, pp. 2419–2430.

[64] T. Kozasa et al. "Dust in Supernovae: Formation and Evolution". In: *ASP Conference Series* 414 (2009), p. 22.

[65] K. Kraus and G. Moore. "Anion Exchange Studies. VI.1,2 The Divalent Transition Elements Manganese to Zinc in Hydrochloric Acid". In: *Journal of the American Chemical Society* 75.6 (1953), pp. 1460–1462.

[66] W. Kutschera et al. "Half-life of 60Fe". In: *Nuclear Instruments and Methods in Physics Research Section B: Beam Interactions with Materials and Atoms* 5.2 (1984), pp. 430–435.

[67] D. Leahy. "Supernova Remnant Evolution: from explosion to dissipation". In: *Supernova remnants an odyssey in space after stellar death, 6-11 June 2016, Greece*. 2016.

[68] M. Limongi and A. Chieffi. "Evolution, Explosion and Nucleosynthesis of Core Collapse Supernovae". In: *The Astrophysical Journal* 592 (2003), pp. 404–433.

[69] M. Limongi and A. Chieffi. "Nucleosynthesis of 60Fe in massive stars". In: *New Astronomy Reviews* 50.7–8 (2006), pp. 474–476.

[70] P. Ludwig. "Search for 60Fe of Supernova Origin in Earth's Microfossil Record". PhD thesis. Technische Universitaet Muenchen, 2015.

[71] P. Ludwig et al. “Time-resolved 2-million-year-old supernova activity discovered in Earth’s microfossil record”. In: *Proceedings of the National Academy of Sciences* 113.33 (2016), pp. 9232–9237.

[72] M. Lugaro and A. Karakas. “26Al and 60Fe yields from AGB stars”. In: *New Astronomy Reviews* 52.7 (2008). Astronomy with Radioactivities. VI, pp. 416–418.

[73] R. Lutter et al. “MARaBOOU - a MBS and ROOT based online/offline utility”. In: *IEEE Transactions on Nuclear Science* 47.2 (Apr. 2000), pp. 280–283.

[74] K. Maeda et al. “Properties of Newly Formed Dust Grains in the Luminous Type IIn Supernova 2010jl”. In: *The Astrophysical Journal* 776.1 (2013), p. 5.

[75] J. Magill et al. “Karlsruher Nuklidkarte”. 9th Edition. 2015.

[76] P. Marcillac et al. “Experimental detection of alpha-particles from the radioactive decay of natural bismuth”. In: *Nature* 422 (2003), p. 876.

[77] S. Merchel and U. Herpers. “An Update on Radiochemical Separation Techniques for the Determination of Long-Lived Radionuclides via Accelerator Mass Spectrometry”. In: *Radiochimica Acta* 84 (1999), pp. 215–219.

[78] S. Merchel et al. “Thin- and thick-target cross sections for the production of 53Mn and 60Fe”. In: *Nuclear Instruments and Methods in Physics Research Section B: Beam Interactions with Materials and Atoms* 172.1 (2000). 8th International Conference on Accelerator Mass Spectrometry, pp. 806–811.

[79] R. Middleton. “A versatile high intensity negative ion source”. In: *Nuclear Instruments and Methods in Physics Research* 214.2 (1983), pp. 139–150.

[80] R. Middleton et al. “Isotopic fractionation of negative ions produced by Cs sputtering in a high-intensity source”. In: *Nuclear Instruments and Methods in Physics Research Section B: Beam Interactions with Materials and Atoms* 93.1 (1994), pp. 39–51.

[81] A. Moro-Martin and R. Malhotra. “Dynamical Models of Kuiper Belt Dust in the Inner and Outer Solar System”. In: *The Astronomical Journal* 125.4 (2003), p. 2255.

[82] R. Muller. “Radioisotope Dating with a Cyclotron”. In: *Science* 196.4289 (1977), pp. 489–494.

[83] D. Nelson et al. “Carbon-14: Direct Detection at Natural Concentrations”. In: *Science* 198.4316 (1977), pp. 507–508.

[84] T. Nozawa et al. “Dust in the Early Universe: Dust Formation in the Ejecta of Population III Supernovae”. In: *The Astrophysical Journal* 598.2 (2003), p. 785.

[85] T. Nozawa et al. “Evolution of Dust in Primordial Supernova Remnants: Can Dust Grains Formed in the Ejecta Survive and Be Injected into the Early Interstellar Medium?” In: *The Astrophysical Journal* 666.2 (2007), p. 955.

[86] H. Oerter et al. “Accumulation rates in Dronning Maud Land, Antarctica, as revealed by dielectric-profiling measurements of shallow firn cores”. In: *Annals of Glaciology* 30 (2000), pp. 27–34.

[87] K. Ostdiek et al. “Activity measurement of 60Fe through the decay of 60mCo and confirmation of its half-life”. In: *Phys. Rev. C* 95 (2017), p. 055809.

[88] *Our Solar Journey Through the Milky Way by NASA/Goddard/Adler/U. Chicago/Wesleyan.* 2017.

[89] B. Pagel. *Nucleosynthesis and chemical evolution of galaxies.* Cambridge University Press, 2009, p. 453.

[90] H. Palme and A. Jones. "Solar System Abundances of the Elements". In: *Meteorites, Comets and Planets* 1 (2003), pp. 41–61.

[91] E. Pian et al. "Spectroscopic identification of r-process nucleosynthesis in a double neutron-star merger". In: *Nature* 551 (2017), p. 67.

[92] J. Plane. "Cosmic dust in the earths atmosphere". In: *Chem. Soc. Rev.* 41 (2012), pp. 6507–6518.

[93] J. Rho et al. "Freshly Formed Dust in the Cassiopeia A Supernova Remnant as Revealed by the Spitzer Space Telescope". In: *The Astrophysical Journal* 673.1 (2008), p. 271.

[94] H. Robertson and H. Russell. "Dynamical Effects of Radiation in the Solar System". In: *Monthly Notices of the Royal Astronomical Society* 97.6 (1937), pp. 423–437.

[95] J. Roy and T. Kohman. "IRON 60". In: *Canadian Journal of Physics* 35.5 (1957), pp. 649–655.

[96] G. Rugel et al. "New Measurement of the 60Fe Half-Life". In: *Phys. Rev. Lett.* 103 (2009), p. 072502.

[97] A. Sarangi and I. Cherchneff. "Condensation of dust in the ejecta of Type II-P supernovae". In: *Astronomy and Astrophysics* 575 (2015), p. 95.

[98] A. Sarangi and I. Cherchneff. "The Chemically Controlled Synthesis of Dust in Type II-P Supernovae". In: *The Astrophysical Journal* 776.2 (2013), p. 107.

[99] R. Sayer. "Semi-empirical formulas for heavy-ion stripping data". In: *Rev. Phys. Appl. (Paris)* 12.10 (1977), pp. 1543–1546.

[100] I. Seitenzahl et al. "Three-dimensional delayed-detonation models with nucleosynthesis for Type Ia supernovae". In: *Monthly Notices of the Royal Astronomical Society* 429.2 (2013), pp. 1156–1172.

[101] D. Silvia et al. "Numerical Simulations of Supernova Dust Destruction. I. Cloud-crushing and Post-processed Grain Sputtering". In: *The Astrophysical Journal* 715.2 (2010), p. 1575.

[102] D. Silvia et al. "Numerical Simulations of Supernova Dust Destruction. II. Metal-enriched Ejecta Knots". In: *The Astrophysical Journal* 748.1 (2012), p. 12.

[103] R. Tagle and J. Berlin. "A database of chondrite analyses including platinum group elements, Ni, Co, Au, and Cr: Implications for the identification of chondritic projectiles". In: *Meteoritics & Planetary Science* 43.3 (2008), pp. 541–559.

[104] A. Taylor et al. "Discovery of interstellar dust entering the Earth's atmosphere". In: *Nature* 380 (1996), pp. 323–325.

[105] *The Hertzsprung-Russel Diagram by ESO (eso0728c).* 2007.

[106] P. Todini and A. Ferrara. "Dust formation in primordial Type II supernovae". In: *Monthly Notices of the Royal Astronomical Society* 325.2 (2001), pp. 726–736.

[107] R. Trappitsch and I. Leya. "A new model for deriving the solar cosmic ray spectrum from lunar rock measurements". In: *Lunar and Planetary Science XLVIII.* 2017.

[108] R. Trappitsch and I. Leya. “Cosmogenic production rates and recoil loss effects in micrometeorites and interplanetary dust particles”. In: *Meteoritics & Planetary Science* 48.2 (2013), pp. 195–210.

[109] J. Truelove and C. McKee. “Evolution of nonradiative supernova remnants”. In: *The Astrophysical Journal Supplement Series* 120 (1999), pp. 299–326.

[110] C. Tuniz et al. *Accelerator Mass Spectrometry: Ultrasensitive Analysis for Global Science*. CRC Press, 1998, pp. 1–400.

[111] A. Wallner et al. “Abundance of live 244Pu in deep-sea reservoirs on Earth points to rarity of actinide nucleosynthesis”. In: *Nature Communications* 6 (2015), p. 5956.

[112] A. Wallner et al. “Recent near-Earth supernovae probed by global deposition of interstellar radioactive 60Fe”. In: *Nature* 532 (2016), pp. 69–72.

[113] A. Wallner et al. “Settling the Half-Life of 60Fe: Fundamental for a Versatile Astrophysical Chronometer”. In: *Phys. Rev. Lett.* 114 (2015), p. 041101.

[114] S. Wanajo et al. “Electron-capture Supernovae as Sources of 60Fe”. In: *The Astrophysical Journal Letters* 774.1 (2013), p. L6.

[115] W. Wang et al. “SPI observations of the diffuse 60Fe emission in the Galaxy”. In: *Astronomy and Astrophysics* 469.3 (2007), pp. 1005–1012.

[116] J. Wasson and G. Kallemeyn. “Compositions of Chondrites”. In: *Philosophical Transactions of the Royal Society of London A: Mathematical, Physical and Engineering Sciences* 325.1587 (1988), pp. 535–544.

[117] S. Woosley and A. Heger. “Nucleosynthesis and remnants in massive stars of solar metallicity”. In: *Physics Reports* 442.1–6 (2007). The Hans Bethe Centennial Volume 1906-2006, pp. 269–283.

[118] S. Woosley et al. “The evolution and explosion of massive stars”. In: *Rev. Mod. Phys.* 74 (2002), pp. 1015–1071.

[119] H. Yang and M. Ishiguro. “Origin of Interplanetary Dust through Optical Properties of Zodiacal Light”. In: *The Astrophysical Journal* 813.2 (2015), p. 87.

[120] L. Yun-Gang et al. “Analysis of Trace Elements in the Bhq Ice Core, Law Dome, Antarctica”. In: *Journal of Glaciology* 34.118 (1988), pp. 297–300.

[121] S. Zhukovska et al. “Evolution of interstellar dust and stardust in the solar neighbourhood”. In: *Astronomy and Astrophysics* 479.2 (2008), pp. 453–480.

[122] J. Ziegler et al. “SRIM-The stopping and range of ions in matter”. In: *Nuclear Instruments and Methods in Physics Research Section B: Beam Interactions with Materials and Atoms* 268.11–12 (2010). 19th International Conference on Ion Beam Analysis, pp. 1818–1823.

Acknowledgments

At the very end, it's time to thank all the people that contributed to the successful outcome of this project. I want to express my deepest acknowledgments and to thank:

- Prof S. Schönert for supervising this project and for financial support.
- Dr. G. Korschinek for so many discussions about AMS and for being an invaluable adviser. Especially your commitment for my future career in AMS, I will neither forget nor underappreciate.
- Dr. T. Faestermann for teaching me inexhaustibly and vividly about experimental nuclear physics and electronics. I enjoyed all our discussions and our handicraft work at the GAMS detector and at the Q3D.
- Dr. P. Ludwig for introducing me to AMS the first time and for arousing my passion for AMS. ^{60}Fe will remain my favorite AMS isotope.
- Dr. K. Hain for fruitful discussions about chemistry, different AMS setups and for introducing me to the AMS community.
- Dr. S. Merchel and the team of the HZDR for the effort on the chemistry of the filter samples. I appreciate your readiness to help me, whenever I have any question about difficult chemistry.
- Dr. J. Welch and the team of the Atominstitut of TU Vienna for the evaporation of the water and helping me to modify the Fe separation chemistry. I really enjoyed working with you in Vienna.
- Dr. S. Kipfstuhl and the team of the AWI for providing the Antarctic snow which was essential for this project.
- Dr. J. M. Gómez-Guzmán and Dr. L. Fimiani for melting and filtering half a ton of snow.
- A. Gärtner for analyzing numerous tiny dust grains from the filters.
- The GAMS team: C. Busser, A. Kinast, D. Krieg, M. Lebert and Pablo for a productive and companionable working atmosphere. I will not forget our night shifts and the catastrophic beamtimes with all the problems and our AMS-Bingo.
- The MLL team: Michi I+II, Christian, Fritz, Schorsch, Horst, Luigi and Christine for your help in all possible situations. I will miss this wonderful lab.
- Last but not least my family for encouraging me and never ending support. Without you, the last five years and especially the next years wouldn't be possible. But beware, now you have a physicist among yourselves.